UNIVERSITAT POLITÈCNICA DE CATALUNYA BARCELONATECH

Control of grid connected power converters with grid support functionalities

Weiyi Zhang

ADVERTIMENT La consulta d'aquesta tesi queda condicionada a l'acceptació de les següents condicions d'ús: La difusió d'aquesta tesi per mitjà del repositori institucional UPCommons (http://upcommons.upc.edu/tesis) i el repositori cooperatiu TDX (http://www.tdx.cat/) ha estat autoritzada pels titulars dels drets de propietat intel·lectual **únicament per a usos privats** emmarcats en activitats d'investigació i docència. No s'autoritza la seva reproducció amb finalitats de lucre ni la seva difusió i posada a disposició des d'un lloc aliè al servei UPCommons o TDX. No s'autoritza la presentació del seu contingut en una finestra o marc aliè a UPCommons (*framing*). Aquesta reserva de drets afecta tant al resum de presentació de la tesi com als seus continguts. En la utilització o cita de parts de la tesi és obligat indicar el nom de la persona autora.

ADVERTENCIA La consulta de esta tesis queda condicionada a la aceptación de las siguientes condiciones de uso: La difusión de esta tesis por medio del repositorio institucional UPCommons (http://upcommons.upc.edu/tesis) y el repositorio cooperativo TDR (http://www.tdx.cat/?locale-attribute=es) ha sido autorizada por los titulares de los derechos de propiedad intelectual **únicamente para usos privados enmarcados** en actividades de investigación y docencia. No se autoriza su reproducción con finalidades de lucro ni su difusión y puesta a disposición desde un sitio ajeno al servicio UPCommons No se autoriza la presentación de su contenido en una ventana o marco ajeno a UPCommons (*framing)*. Esta reserva de derechos afecta tanto al resumen de presentación de la tesis como a sus contenidos. En la utilización o cita de partes de la tesis es obligado indicar el nombre de la persona autora.

WARNING On having consulted this thesis you're accepting the following use conditions: Spreading this thesis by the institutional repository UPCommons (http://upcommons.upc.edu/tesis) and the cooperative repository TDX (http://www.tdx.cat/?locale-attribute=en) has been authorized by the titular of the intellectual property rights **only for private uses** placed in investigation and teaching activities. Reproduction with lucrative aims is not authorized neither its spreading nor availability from a site foreign to the UPCommons service. Introducing its content in a window or frame foreign to the UPCommons service is not authorized (framing). These rights affect to the presentation summary of the thesis as well as to its contents. In the using or citation of parts of the thesis it's obliged to indicate the name of the author.

PhD Thesis

Control of Grid Connected Power Converters with Grid Support Functionalities

Weiyi Zhang

Barcelona, March 2017

Control of Grid Connected Power Converters with Grid Support Functionalities

Weiyi Zhang

Dissertation submitted to the Doctorate Office of the Universitat Politècnica de Catalunya in partial fulfillment of the requirements for the degree of Doctor of Philosophy by the

UNIVERSIDAD DE MALAGA

UNIVERSIDAD DE SEVILLA

UNIVERSIDAD DEL PAÍS VASCO/EUSKAL ERRIKO UNIBERTSITATEA

UNIVERSITAT POLITÈCNICA DE CATALUNYA

Joint Doctoral Programme in Electric Energy Systems

Barcelona, March 2017

Control of Grid Connected Power Converters with Grid Support Functionalities

Copyright © Weiyi Zhang, 2017
Printed by the UPC
Barcelona, March 2017

ISBN:–.
Research Project: ENE 2014-60228-R
ENE 2016-79493-R

UNIVERSITAT POLITÈCNICA DE CATALUNYA
Escola de Doctorat
Edifici Vertex. Pl. Eusebi Güell, 6
08034 Barcelona.
Web: http://www.upc.edu

UNIVERSIDAD DE MALAGA
Escuela de Doctorado
Pabellón de Gobierno - Plaza el Ejido s/n
(29013) Málaga.
Web: http://www.uma.es

UNIVERSIDAD DE SEVILLA
Escuela Internacional de Doctorado
Pabellón de México - Paseo de las Delicias, s/n
41013 Sevilla.
Web: http://www.us.es

UNIVERSIDAD DEL PAÍS VASCO/EUSKAL ERRIKO UNIBERTSITATEA
Escuela de Master y Doctorado
Edificio Aulario II - Barrio Sarriena, s/n
48940- Leioa (Bizkaia) Spain.
Web: http://www.ehu.eus/es

To those who persist…

ACKNOWLEDGEMENTS

First of all, I would thank my supervisor, Prof. Pedro Rodriguez for his guidance, as well as for creating an environment that fosters practice and team work, enabling me to carry out all the research activities during my PhD study. In addition to the critical support on the research subjects, his personality also gave me great positive influences to get me through the fancy and challenging journey.

I would thank Dr. Alvaro Luna, who has given me infinite support in all aspects. Thanks to his guidance and arrangement, I got rich opportunities to stay in labs to get practical experience in grid converter control, which I believe will benefit me not only in completing the PhD tasks, but also for being qualified for future jobs.

I would thank Dr. Ignacio Candela for always being open to me for solving any doubt in the study subjects. My PhD study will not be accomplished without always taking knowledge and tools from him.

I would thank Dr. Joan Rocabert for the vast amount of time and effort that he has spent, for helping me completing objectives in labs or improving technical reports for publications.

I would thank Dr. Raul Santiago, who has fought with me against the 100 kW grid converter, because of whom I also improve my DSP programming.

I would also thank Dr. Juan Ramon Hermoso, Khadija El Haddadi, Lidia Herrera and Elena Corbera for helping me handling the organizational and administrative issues, and thus make it possible for me to work without distractions.

I would thank Daniel Remon and Antoni M. Cantarellas for always inspiring me, for helping my ideas growing, and for teaching me to use the proper tools for several study subjects.

I would also thank Andres Tarrasso, Jesus Amo, Alvaro Rodriguez, Costantino Citro, Victor Fauquet, Sergio Gimenez, Miguel Altes for the countless help that I got in the labs, and thank Kumars Rouzbehi, Cristian Verdugo, Mohamed Elsaharty, Mostafa Bastaki, Nurul Roslan, Leonardo Marin, David Arancibia, Mahdi Shahparasti, Cosmin Ciobotaru, Mehdi Monadi, Elyas Rakhshani, Catalin Gavriluta, Ruben Capo, Josep Oltra for the impressive talks.

I feel honored and grateful to be supported by the China Scholarship Council with the CSC-UPC Joint PhD Scholarship project, by which I am able to conduct my PhD study. I would thank Prof. Zhang Xiaobin and Prof. Wu Xiaohua from Northwestern Polytechnical University, for helping me in applying for this scholarship.

Finally, I would give thanks to my beloved family and many friends of mine, who have supported or encouraged me at one time or at all times.

Weiyi Zhang
Terrassa, Barcelona, Spain
March, 2017

Abstract

The installation of power generation systems based on renewable energy sources has been increasing exponentially over the last decades. However, in spite of the well-known merits of such energy sources, the expansion of renewable-based generation (RG) plants, which interface the grid through power converters, can produce also negative impacts on the electrical grid, due to its power processing mechanism, which is different from traditional generation plants. In fact, the regulation capability of the grid can decrease as much as the share of the RG increases. To avoid this, power conversion systems belonging to RG plants are requested to be more grid-friendly, responsive to the electrical network conditions, as well as grid-supportive. In this way, they can contribute to the electrical network stability as other generation does, instead of behaving as simply grid-feeding systems focused on injecting as much power as possible.

This PhD dissertation is focused on the control of grid-connected power converters with grid support functionalities based on the Synchronous Power Controller (SPC) concept. The SPC is an established solution for controlling grid connected power converters and equipping them with emulated and improved synchronous machine characteristics. In addition to the general goal of improving the grid interaction of the RG plants, grid support functionality stands as a main property among the characteristics given by the SPC.

Considering the fact that the power conversion stage of RG plants normally act as current sources to feed the grid, it is necessary to count on a low-level current controller to regulate the current injected by the power converter. Even though other controllers can be used in upper levels, a fast and accurate current controller in the inner loop is still essential to control and limit the current and to realize a specific function combining other controllers. However, the tuning of these controllers is not always simple, as the output connection filters play a relevant role in the transient and steady-state performance of the power conversion stage. For this reason, this work proposes a unified current controller tuning approach for the typical linear controllers in stationary or synchronous reference frame. Conventional methods normally set the controller gains by trials of placing the open-loop poles considering the stability and dynamics limits, or by direct calculation using the stability and dynamics inputs. However, the inputs for controller gains calculation are commonly given out of different conventions. The proposed method, instead, gives numerous inputs in a wide range for controller gains calculation, and select the optimal solution by evaluating and comparing the numerous resulting systems.

Taking into account that the inner control block just permits the system to behave as a proper current source, this research is more focused on the external blocks, the one that give full sense to the SPC structure. In this dissertation the virtual admittance structure, contained in the electrical block of the SPC, which emulates the stator output impedance of the synchronous machines, is analyzed. Moreover, it is extended to a study case where the admittance value can be different for positive- and negative-sequence components. The designed virtual admittance block contains three branches, which are responsible for positive-sequence current injection, negative-sequence current injection and other harmonic components, respectively. The converter's performance under asymmetrical grid fault is especially considered in this case.

The analysis and arrangements in the design of the SPC's power loop controller is another contribution of this research. Other methods that consider synchronous machine emulation normally construct the controller by reproducing the synchronous generation swing equation. Based on the virtual implementation, which is free from mechanical constraints, one can set a proper damping factor achieving thus better dynamics compared to the traditional synchronous machines. However, the increase of the damping factor changes the inherent power-frequency (*P-f*) droop characteristics, which may lead to undesired deviations in the active power generation. In the framework of this PhD, a method that modifies the conventional swing equation emulation and lets the inherent *P-f* droop characteristics be configurable, independently of the inertia and damping characteristics, is proposed.

The work presented in this dissertation is supported by mathematical and simulation analysis. Moreover, in order to endorse the conclusions achieved, a complete experimental validation has been conducted. As it will be shown, the performance of the SPC has been validated in tests once the main parts, namely virtual admittance and power loop controller, and other parts are settled. The simulation and experimental test scenarios include events like changes in the power operation point, frequency sweeps, voltage magnitude changes, start-up and parallel converters operation, which are given under different control configurations like the different structures for the power loop controller and different control parameters. This PhD research also compares the transient performance of the SPC-based power converters with the ones achieved with conventional control methods.

Considering the outer blocks, more linked to voltage and frequency regulation, some analysis regarding the design of the droop control in voltage source converter (VSC) stations in multi terminal direct current (MTDC) systems is also analyzed as a particular study case. Considering that the MTDC system is a potential ac grid supporter in the future, the proposed VSC control method combines the ac frequency droop and the dc voltage droop to come up with the Unified Reference Controller (URC), which is validated in a simulated CIGRE test model.

Contents

FIGURES

TABLES

ACRONYMS

SGEC	synchronous generation emulation control
PLL	Phase-Locked Loop
PI	Proportional Integral
PR	Proportional Resonant
RES	renewable energy sources
VCO	Voltage-Oscillated Controller
PV	photovoltaic
HVDC	High Voltage Direct Current
VISMA	Virtual Synchronous Machine
VSYNC	Virtual Synchronous Generator
SPC	Synchronous Power Controller
MTDC	multi terminal direct current
VSC	Voltage Source Converter
PWM	Pulse-Width Modulation
PLC	power loop controller
RPC	reactive power controller
TSO	transmission system operator
FLL	Frequency-Locked Loop
SOGI	Second-Order Generalized Integrators
D-SOGI	dual Second-Order Generalized Integrators
REE	Spanish Electrical Grid
PCC	Point of Common Coupling
ZOH	Zero Order Hold
IARC	Instantaneous Active and Reactive Control
MPL	Mechanical Power Loop
CND	Configurable Natural Droop
VCC	vector current control
URC	Unified Reference Controller
GVD	Generalized Voltage Droop

CHAPTER 1.

Introduction

This chapter introduces the background of the thesis topic, the state of the art and the objectives of the PhD studies. The new requirements for control of grid connected power converters are firstly indicated, which have caused the need for developing controllers emulating a synchronous generator. The state of the art of the synchronous generation emulation control (SGEC) is then reviewed, followed by the main objectives of the thesis that are answered in the next chapters.

1.1 Background

Due to the increasing global energy demand and the need for alternative and sustainable forms of energy, power generation plants based on renewable energy sources (RES) have increasingly penetrated into electrical grid over the past years. High-level penetration of renewables has reshaped the modern electrical grids. Grid connected power converters commonly act as the interface between the RES-based generation plants and the grid for harvesting wind and solar energy and feeding the grid, as shown in Fig. 1.1.

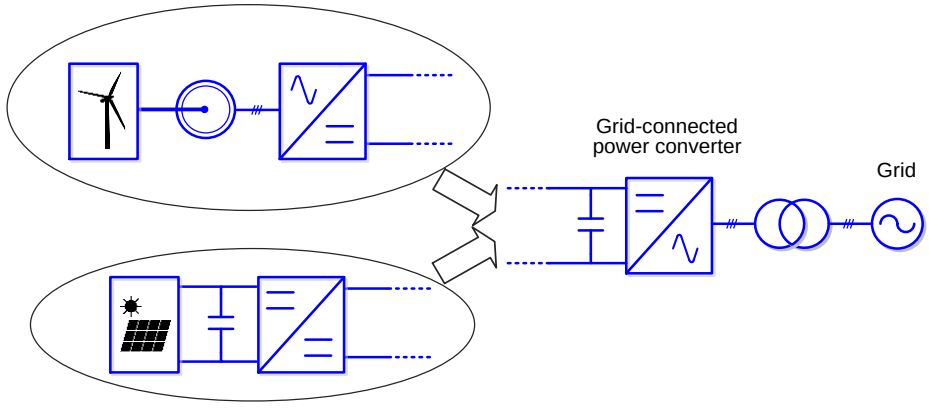

Fig. 1.1. Grid connected power converter for wind and photovoltaic generation.

The large penetration of renewables is facilitated by the fast development of grid connected power converters. The control of grid connected power converters have been drawing many interests, since the performance of these converters will considerably influence the grid power quality and determine whether the generation plant meets the grid connection requirements.

1.1.1 Conventional control for grid connected power converters

Conventional control of grid connected power converters have been well validated in many applications and shows its effectiveness [1]–[4]. Fig. 1.2 shows a typical conventional control scheme for grid connected power converters, where the control part is divided into the inner and the outer loops. The inner loop controls the grid injection current i_{abc} and sends driving pulses $d_{1\text{-}6}$ to the converter. The current loop controller normally has a Proportional Integral (PI) or Proportional Resonant (PR) structure, depending on the control reference frame (PR for stationary reference frame and PI for synchronous reference frame). The outer loop provides the current reference for the inner loop and controls the active power P and reactive power Q injected to the grid. The reference of the inner loop is i_d^* and i_q^* in case of synchronous frame control (while in case of stationary frame control, I and φ, namely, the amplitude and phase-angle of the reference current, are calculated to further generate i_α^* and i_β^*). The active and reactive power control can work in closed-loop, by using PI controllers, or in open-loop, by using instantaneous power calculations [5]. The grid synchronization is achieved through a dedicated grid synchronization unit known as Phase-Locked Loop (PLL) [6], which obtains the phase-angle θ and angular speed ω of the grid voltage v_{abc}. The converter response and its interaction with the grid are strongly affected by the PLL dynamics. The active power control effort i_d^* is adjusted by a dc voltage controller to keep the power balance on the dc bus.

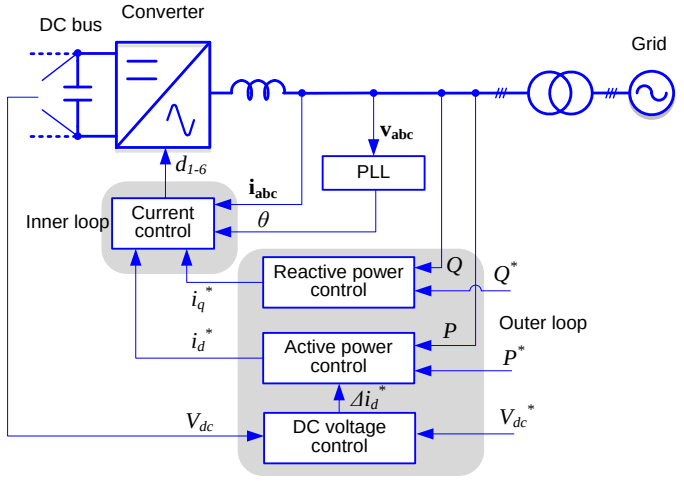

Fig. 1.2. Conventional control block diagram for grid connected power converters (inner current control in synchronous reference frame).

The detailed current control structure in synchronous reference frame is shown in Fig. 1.3. The current variables i_d and i_q are transformed from the three-phase grid current measurement $\mathbf{i_{abc}}$ using Park transformation T_θ, which is written as:

$$\begin{bmatrix} i_d \\ i_q \end{bmatrix} = \mathbf{T_\theta} \begin{bmatrix} i_a \\ i_b \\ i_c \end{bmatrix}, \quad \mathbf{T_\theta} = \frac{2}{3} \begin{bmatrix} \cos(\theta) & \cos(\theta - \frac{2\pi}{3}) & \cos(\theta + \frac{2\pi}{3}) \\ -\sin(\theta) & -\sin(\theta - \frac{2\pi}{3}) & -\sin(\theta + \frac{2\pi}{3}) \end{bmatrix}. \tag{1.1}$$

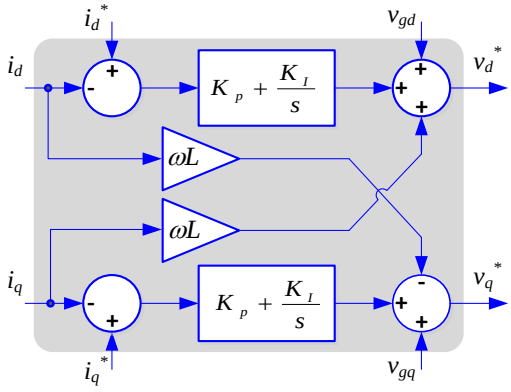

Fig. 1.3. Current control structure for three-phase power converters in synchronous reference frame.

In the structure shown in Fig. 1.3, the well-known PI controller is used thanks to the Park transformation, which creates a reference frame rotating with the angular speed corresponding to the grid frequency. With the cross coupling branches, the active and reactive powers can be controlled separately. As a measure to improve the grid disturbance rejection and dynamic response, grid voltage feed forward can be used, and v_{gd} and v_{gq} are obtained by transforming the three-phase grid voltage measurement $\mathbf{v_{abc}}$.

A PLL is used to obtain the grid voltage phase-angle θ for Park transformation. A basic structure of the PLL is shown in Fig. 1.4.

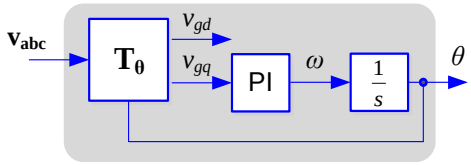

Fig. 1.4. Basic block diagram of the synchronous reference frame PLL.

A detailed outer loop control structure is shown in Fig. 1.5.

In summary, based on the conventional control paradigm, the grid connected power converter acts as a current feeder for the grid. The statics (steady-state power reference) of the converter is determined by the status of the primary source, and the dynamics (transient performance under grid disturbances) is determined by the PLL.

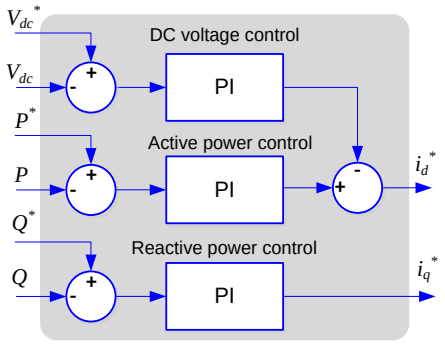

Fig. 1.5. Outer closed-loop control structure [6].

1.1.2 Frequency and voltage droop control

Along with the expansion of the RES generation plants, their negative impact on the power system has caused increasing attention [7]. The regulation capability of the grid can be reduced as much as the share of the renewable generation increases. Therefore, depending on the renewable penetration level (percent of renewable generation in the system), grid connected power converters should show differences in their roles, interconnection objectives and applicable standard [8], which is explained in detail in Table 1.1.

In the grid of the future, grid connected power converters are expected to be grid-friendly, or even grid-supportive, instead of simply grid-feeding elements.

The stability of a given electrical power system is dependent on balancing generation, demand and power losses. The estimation of generation and demand plays a decisive role when planning operation schedules for power plants and transmission systems. With continuous penetration of renewables and the expansion of distributed generation plants, central coordination becomes more challenging. Instead, generation and demand with automatic response to voltage and frequency changes becomes a promising solution in the long run, considering both stability and economy.

In practice, traditional power stations that are comprised of synchronous generators incorporate a droop mechanism for regulating their generated power as a function of the grid frequency variation. In order to provide frequency and voltage regulation from each interfaced terminal in modern electrical networks, renewable generation plants based on grid connected power converters are required to interact with the grid and provide frequency and voltage support. Therefore, the steady-state performance of a grid connected power converter needs to be set by its droop characteristics, instead of simply controlling its dc-bus voltage to inject all the available power provided by the renewable resource to such a bus.

Droop control has been well used in the control of grid connected power converters as seen in [9]–[13]. The droop loops can contribute to primary voltage and frequency control by adjusting the active and reactive power set point proportional to the deviation of frequency and ac voltage magnitude, respectively. Fig. 1.6 shows the frequency and voltage

droop control structure.

Table 1.1 Grid nature under different penetration level [8]

	≤ 2% of generation	≤ 10% of generation	≤ 25% of generation	100 % of generation
Grid penetration scenario	Low level penetration	Moderate level penetration	High level penetration with grid capacity less than load demand	Renewable plants operate part time as an island
Renewables impact and its role	Not significant to grid operation	Not critical, affect distributed voltage	Critical to power delivery and meeting demand	Main power source for stand alone operation
Interaction objectives	No interference, good citizen and compatible	Manage any local distribution impacts	Engage in system operation and control	Responsible for stability and regulation
Rule / standard	IEEE 1547-2003 current practice	Modified 1547, add penetration limits	New rules include operation and grid support	Stand-alone rules
Issues	Trip limits, fault response, synchronization	Interfere with regulation, islanding, coordination	Regulation, ramping response, interactions of machine control	Load following, voltage control, normal and reserve capacity

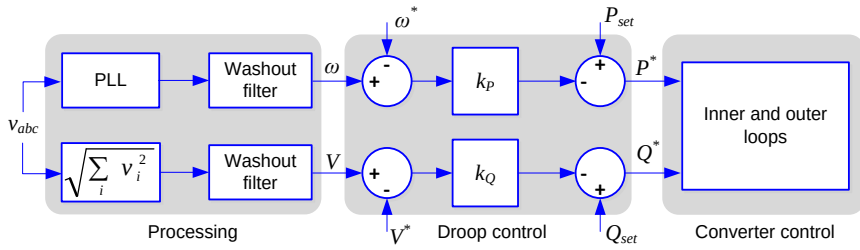

Fig. 1.6. Frequency and voltage droop control for grid connected power converters.

The droop control block interconnects the processing block and the converter control block. k_p and k_q are the droop gains for the frequency and voltage control, respectively. The processing block calculates the frequency and voltage magnitude and filter the output by a low pass filter.

With the droop control, the active power generation is automatically adjusted by a primary frequency error, and the reactive power generation automatically supports the ac voltage error. The converter can interact with the grid with the aid of energy storage or curtailed power. In this manner, the converter enhances the regulation capability of the

whole grid.

1.1.3 Synchronous generation emulation control

In order to further improve the performance of the grid connected power converters, different topics regarding converter control have been discussed, and various control strategies are proposed in order to comply with the updated grid codes and realize better functionality.

The generation in traditional power system is predominated by synchronous generators. Conventional grid connected power converters differ from synchronous generators mainly in the lack of the electromechanical characteristics. In consequence, the static and dynamics of the renewable power generation units are both different compared with the synchronous generators. Even if the statics can be changed by equipping the droop control and energy reserve, there are yet some disadvantages of the converter-interfaced generation plants.

The PLL is a grid voltage estimator used by conventional power converters to determine the amount of current to be injected either in-phase or in-quadrature to regulated the active and reactive powers delivered to the grid, respectively. Therefore, the dynamics of these conventional converters are characterized by the PLL, whose performance will degrade under weak or islanded grid conditions [14], [15]. As a PLL is not designed to emulate any inertial response in the presence of frequency deviations, the total inertia in the grid decreases as the integration of renewable generation plants grows. However, the updated grid codes have included “synthetic inertia” in the requirements [16].

Other shortcomings of conventional converters controllers based on the usage of PLL include the inferior performance under grid fault conditions [17], in weak grid connection [14] and low *X/R* ratio grid connection [18].

In contrast, the very well-known synchronous generators possess advantages like the contribution to inertia, the robust connection to weak grids, the natural load sharing and unbalanced voltage support. Therefore, the emulation of synchronous generators and the implementation of its electrical and mechanical characteristics on grid connected power converters have been intensively studied in recent years.

1.2 State of the Art of Synchronous Generation Emulation Control

The idea of approaching the grid connected power converters’ dynamics toward the electromechanical response of synchronous generators is well accepted by grid operators, since the successful operation of the traditional power system relies on the generation and regulation capability of the numerous synchronous generators.

Particularly, the output impedance of a synchronous machine determines its electrical characteristic, which define load sharing and voltage droop, and the rotor inertia determines its natural mechanical response, which guarantees the healthy dynamics of the power

system. Therefore, the synchronous generation emulation control (SGEC) (mainly the emulation of the electromechanical characteristics) has been widely discussed ever since its first publication [19].

1.2.1 Main methods for SGEC

Studies on SGEC have been conducted and reported in many publications. Even though different works vary in the objectives considering different aspects of synchronous machines, most of them share a common goal of improving the interaction between grid connected power converters and the electrical grid. Providing inertial characteristics to grid connected power converters appears as the main objective in many works. Table 1.2 categorizes the most representative works in the literature according to the method used for emulating inertia.

Table 1.2 Category of existing publications on SGEC according to the inertia emulation method

Method for inertia emulation		Publications
Type 1: Extra loop		[20]–[23]
Type 2: Modified PLL		[24]
Type 3: Power (or dc voltage) control	Type 3-A*	[25]–[36]
	Type 3-B*	[37], [38]
	Type 3-C*	[39]–[51]
Inertia emulation not specified		[14], [15], [52]

*Type 3-A: direct modulation as the inner loop
*Type 3-B: cascaded voltage-current control as the inner loop
*Type 3-C: virtual impedance/admittance as the inner loop

In a first group of works, inertia emulation is realized by adding an extra loop to the conventional control structure shown in Fig. 1.2. In this case, instead of using a dc voltage controller to modify the active power reference, the structure shown in Fig. 1.7(a) is used to modify such active power reference according to a function of the grid frequency value [20]–[22]. As an alternative, this extra loop method can also be used to specify the dc voltage reference using the structure shown in Fig. 1.7(b) [23].

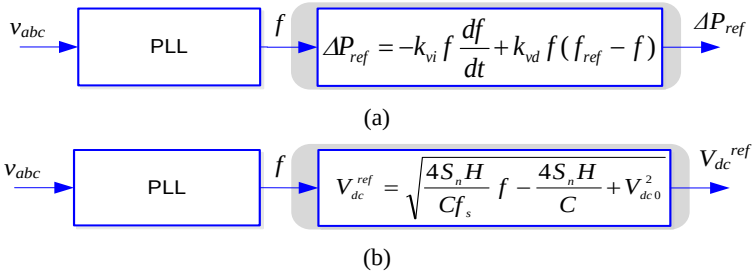

Fig. 1.7. Inertia emulation control structure using an extra loop (Type 1): (a) an extra loop to modify the active power reference, and (b) an extra loop to set the dc voltage reference.

In Fig. 1.7, v_{abc} is the measured voltage at the point of connection, ΔP_{ref} is the active power reference variation, V_{dc}^{ref} is the dc voltage reference, k_{vi} the virtual inertia constant,

k_{vd} the virtual damping constant, f_{ref} the reference frequency, S_n the rated power of the converter, H the virtual inertia constant, C the dc bus capacitance, and V_{dc0} the dc voltage operation point.

The main feature of this method is the minor changes to the conventional control structure. On the other hand, the derivative operation on the measured grid frequency and the dependence on a PLL can potentially lead to challenges in practical implementation.

In a second group of works, the inertia emulation is realized in a modified PLL, as shown in Fig. 1.8, which is proposed in [24]. Similar to the first method for emulating inertia, this implementation entails only minor changes in the conventional control structure shown in Fig. 1.2, where all the blocks are kept the same, except for the PLL. In Fig. 1.8, E is the specified nominal amplitude of the virtual electromotive force, X the virtual reactance, J the virtual moment of inertia, and ω_s the nominal grid frequency. It is worth noting that the lack of any damping term (K_p in the traditional PLL) can render the system oscillating.

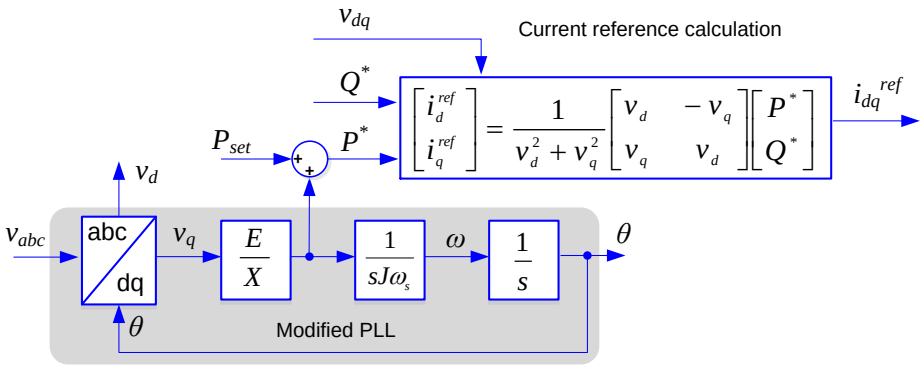

Fig. 1.8. Modified PLL for inertia emulation (Type 2).

The inertia emulation in the abovementioned two methods (Type 1 and 2 in Table 1.2) is both dependent on an external voltage source, and hence the power converter needs an extra control scheme to form the grid in case of island operation. Besides, even though the dynamic interaction between the converter and the grid is modified to emulate a synchronous machine response, the active power transfer dynamics is still different from the one of a synchronous machine.

Considering these two facts, a third type of method for inertia emulation emerged, which uses a power loop controller to emulate virtual inertia. In this manner, the active power transfer dynamics and power-frequency interaction dynamics are both changed, and grid forming capability is enabled.

This third type of method for emulating inertia can be represented by Fig. 1.9. In this figure, the inertia emulation function is realized by the active power controller as Fig. 1.9(a) shows. As an alternative, the inertia emulation function can also be realized by a dc voltage controller [42], [46]. In this method, the grid synchronization is achieved by a power balance synchronization mechanism, other than the PLL, which synchronizes according to the phase difference between the grid voltage and the signal generated by a voltage-controlled oscillator (VCO).

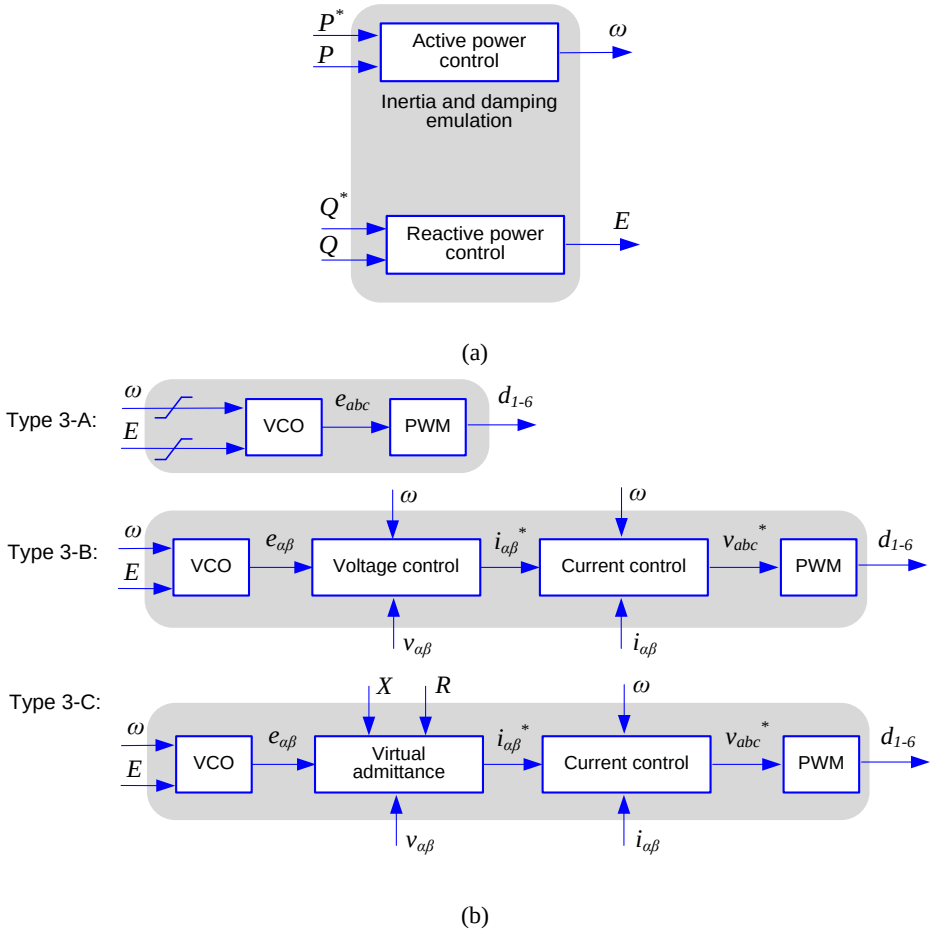

Fig. 1.9. Power loop controller for inertia emulation (Type 3): (a) active and reactive power controller, and (b) three different strategies in the electrical inner loop.

The VCO in Fig. 1.9(b) integrates the angular speed to calculate the voltage phase-angle, and uses this phase-angle, together the voltage amplitude E, to generate a virtual electromotive force e, which can be expressed in any reference frame, i.e., *abc*, *αβ*, or *dq*.

Publications dealing with the power loop control method use three different approaches to control the interaction between the virtual electromotive force and the electrical grid voltage, namely the open loop modulation, the cascaded voltage-current control and the virtual impedance/admittance structure.

When the open loop strategy is used, limiters for E and ω are needed, since there is no measure for limiting either the converter output voltage or its injected current. This control strategy, i.e., Type 3-A in Fig. 1.9(b), is used and validated in many publications as shown in Table 1.2.

In order to use a voltage control other than a simple direct modulation, a cascaded voltage-current control is implemented in the inner loop, i.e., Type 3-B in Fig. 1.9(b). In

this case, in addition to the voltage control loop, a current loop is also used to control and limit the grid current as a protection for the converter. Fig. 1.9(b) shows the implementation of this strategy in stationary $\alpha\beta$ reference frame, while it can also be implemented in synchronous *dq* reference frame as in [37] and [38].

In medium-voltage or low-voltage networks, the load sharing among multiple converters is largely affected by the line impedance, which is not predominantly inductive. In some publications, in addition to the emulation of the mechanical part of the synchronous machines (rotor inertia and damper winding), the emulation of the electrical part (stator output impedance) is also considered, i.e., Type 3-C in Fig. 1.9(b). In this manner, the load sharing can be better controlled with a virtual output impedance. In fact, virtual impedance is the focus of many papers based on the configuration of paralleled converters [53], [54]. An alternative technique to virtual impedance implementation is the virtual admittance implementation. The difference between both implementation techniques will be explained in detail in the Chapter 2. It is worth mentioning however that virtual impedance/admittance technique can also be used for objectives such as harmonics compensation [55], [56] and impedance shaping in cascaded converters [57].

Except for inertia emulation, many papers have put focus on other aspects of SGEC as follow. The associated energy storage is especially designed in [58]. The enhancement to the stability in weak grids connection is studied in [14], [15], [52]. Local stability analysis, based on linearized model and the stability oriented tuning approach, are presented in [37], [48]. A fault-condition (short circuit) performance indicator is proposed in [24]. In [29], the authors propose to use a virtual resistance for realizing low voltage ride through. A comparative study between the SGEC and the traditional synchronous machine is conducted in [43], where the performance in presence of load changes is shown. A photovoltaic (PV) plant model based on SGEC is given in [50]. Regarding the value to be set for the inertia constant of virtual synchronous generators, proposals dealing with adaptive inertia and damping control [21] and alternating inertia constant [34] can theoretically bring some advantages that traditional synchronous machines do not possess. Overviews on the SGEC concept can be found in [59], [60].

Perspectives for using the synchronous generation emulation concept in future scenarios are promising. Distributed renewable generation, high-voltage dc (HVDC) transmission and vehicle to grid are potential scenarios for its application.

1.2.2 Validations of the SGEC concept

Many papers have contributed to the implementation and validation of the SGEC concept. The test scenarios used in such validations vary from case to case and can be categorized as Table 1.3 shows.

Since inertia emulation totally reshaped power control dynamics in power converters, tests dealing with steps in active power reference are commonly found in the existing publications. Besides, since the interaction between grid connected power converters and the grid is improved, test scenarios considering load changes, voltage sags, frequency changes, grid phase-angle jump, unbalanced and distorted grid are also found in the literature. Taking into account that distributed generation might be the main application for

SGEC, test scenarios dealing with power converters islanding and reconnection are also found in publications.

Table 1.3 Typical test scenarios found in the existing publications on SGEC

Test scenario	Publications
Active power (or dc voltage) and reactive power steps	[14], [15], [19], [25], [26], [30], [31], [33], [34], [36], [37], [40], [44]–[47], [50], [61]
Load changes	[21]–[23], [25], [29], [35], [39], [42]–[44], [49], [51]
Voltage sag	[14], [15], [23]–[25], [29], [33], [34], [36], [40], [52]
Frequency changes	[20], [33], [36], [40], [45], [50], [62]
Grid phase-angle jump	[35], [36]
Start-up without PLL	[33], [36]
Islanding	[25], [29], [30], [40], [42]–[44], [51]
Island operation with unbalanced and nonlinear loads	[44]
Reconnection of island	[30], [42], [43], [51]
Unbalanced and distorted grid	[36]
Working when the grid frequency has a deviation	[27], [33]
Changes in solar radiation in a PV system	[49]

1.2.3 Important landmarks in the research activities on SGEC

Research activities on the SGEC concept began in the last 10 years, and this idea keeps catching increasing attention. Discussions on the concept, control design for power converters, and laboratory validation are the main activities reported in the literature. Fig. 1.10 shows several landmarks of the research activities on SGEC that might be worthy to mention.

The first publication found on SGEC is a conference paper authored by H. P. Beck et al. and published in 2007 [19], where the fundamental concept and preliminary experimental results (7 kW) were shown in scenarios where steps in the inner voltage phase-angle and magnitude were considered. A patent soon followed this paper, which is authored by the same research team whose work is known as Virtual Synchronous Machine (VISMA) [63].

The first journal paper found in the literature was authored by M. R. Iravani et al. and published in 2008 [25]. In this paper, a detailed control scheme is presented, indicating how the concept is implemented. In this paper, inertial characteristics are achieved by using an active power control loop, and the inner loop is based on direct modulation of the power converter. Many papers published later follow a similar design (Type 3-A diagram in Fig. 1.9).

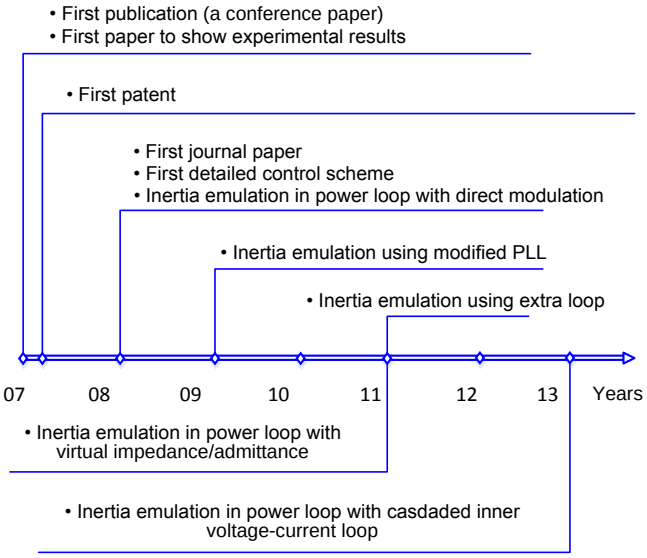

Fig. 1.10. Important landmarks in the research activities on SGEC.

The PLL with inertia emulation capabilities (Type 2 method in Table 1.2) was firstly proposed in a paper authored by M. V. Wesenbeeck et al. and published in 2009 [24]. The authors in this paper are known by a project entitled "Virtual Synchronous Generator" (VSYNC), of which the results were published in a series of papers after finishing the project.

Inertia emulation by using an extra loop (Type 1 method in Table 1.2) started appearing in publications in 2011, being firstly found in [20], a paper authored by T. K. Vrana et al. As previously mentioned, the main concern of this type of inertia emulation method is its practical implementation, since it is based on a time-derivative operator. On the other hand, the main advantage of this method is its simplicity in modeling and simulation, which helps the analytical validation of the SGEC in large systems.

The combination of inertia emulation and virtual impedance/admittance (Type 3-C diagram in Fig. 1.9) emerged with the name Synchronous Power Controller (SPC) in 2011 and was authored by P. Rodriguez et al. [41]. The inclusion of the virtual admittance in the power converter controller brings several advantages, such as accurate power sharing, grid current control, easy implementation, etc.

An alternative method (Type 3-B diagram in Fig. 1.9) was proposed to avoid direct modulation in the power converter's inner loop. The first paper presenting this control method was authored by S. D'Arco et al. and published in 2013 [37]. It is worth noting that Fig. 1.10 only shows the first publication for each type of method, while several research teams published their work at approximately the same time and have been active in reporting their results. Such teams include the "Synchronverters" team (G. Weiss et al.) [27] and Ise Lab (T. Ise et al.) [29].

1.3 Objectives of This PhD Dissertation

The research work in this PhD dissertation was conducted toward the general goal of improving grid interaction of grid connected power converters and providing advanced support services to the electrical grid. Several objectives were stated to guide the PhD project, which are summarized in the following:

1- Setting a methodology to tune the inner current control loop for virtual admittance implementation
2- Achieving a detailed design and validation of the SPC virtual admittance
3- Achieving a detailed design and validation of the SPC power control loop for inertia and damping emulation
4- Conducting an integrated frequency and dc voltage droop control design for voltage source converters in a multi terminal direct current (MTDC) system

Most of the results in this PhD dissertation aim to report the studies on the SPC, which is a representative SGEC solution, which was previously categorized as a Type 3-C control method. These objectives contribute to enrich particular details of the SPC regarding implementation, and considering specific needs in different scenarios.

A. Current control loop tuning

Grid connected power converters are controlled by multi-loop controllers like the SPC in many cases, in which a current controller is used in the inner control loop [22], [24], [42]–[44]. The inner current loop for grid connected power converters characterizes the system dynamics considerably, and the dynamics of the outer loops is normally analyzed assuming the current loop performing a fast response. Moreover, the current loop plays an important role since it intrinsically determines the stability of the system. Therefore, the design of inner current loop is critical for the overall performance of multi-loop controller. Besides, the control tuning for converters in high power applications becomes more challenging due to the reduced control bandwidth and increased complexity in the grid connection filter. Therefore, the first objective of this PhD dissertation is to develop a unified current loop tuning methodology for grid connected power converters, which should be generally applicable in different cases.

B. Virtual admittance

In distributed generation, even though the droop gain of each generation unit can define load sharing characteristics, the actual load sharing is also dependent on the lines impedance. Since estimating line impedance is difficult in a configuration with paralleled generation units, emulating the predominant output impedance of synchronous machines in the power converter controller can becomes a possible solution to minimize the effect of lines impedance in load sharing. Besides, the current loop contained in the virtual admittance structure can control and limit the current injected into the grid by the power converter, which is more feasible in realistic applications.

Grid connected power converters can face voltage sags caused by different types of grid faults. In spite of the fact that three-phase faults are considered for stating the LVRT requirements in most of the grid codes, asymmetrical faults are the most common faults in

electrical grids [64], [65]. Even though sophisticated ride-through abilities can be enabled in power converters to prevent tripping of renewable generation units under fault conditions [66], [67], the lack of contribution of negative-sequence current during asymmetrical faults motivates further improvement in the control design [68].

Therefore, another objective of this PhD dissertation is to design a virtual admittance controller for accurate load sharing, grid current control and voltage support under asymmetrical grid faults.

C. Power loop controller

Making a proper design of the power loop controller is one of the objectives of this PhD dissertation. The structure of the power loop controller should have a specific form, which should result in accurate inertia and damping emulation, like in a electromechanical synchronous generator. Based on this philosophy, the mainstream technique for the power loop controller is the emulation of the synchronous machine swing equation, which was studied in [25] and many other publications. This emulation strategy will be analyzed first, and then other solutions will be discussed and presented.

D. Integrated frequency and dc voltage droop control design for voltage source converters in an MTDC system

An MTDC system can be connected to different ac areas through VSCs. As a convention, these VSCs are normally given a dc voltage droop control mechanism to ensure a stable operation of the MTDC system. On the other hand, these VSCs do not interact with the ac areas that they are connected, except for delivering power to them.

The droop control design for VSCs in a MTDC grid is one of the objectives of this PhD dissertation. In addition to the typical dc voltage droop control, frequency droop control should be also considered in order to meet the needs from the ac systems and provide associated frequency support.

1.4 PhD Dissertation Organization

The following chapters in this PhD dissertation are organized as follow. Chapter 2 introduces the Synchronous Power Controller (SPC), which acts as the basis of the main results obtained in this PhD project. The main features of the SPC are given in this chapter. Virtual admittance design oriented to asymmetrical grid fault conditions is reported in Chapter 3, and a unified current loop tuning approach is also presented in this chapter. Chapter 4 presents a power loop controller that makes the inherent *P-f* droop gain configurable, other than a faithful replication of the synchronous machine swing equation. In Chapter 5, a unified droop control strategy is presented for the VSCs in an MTDC grid. Simulation and/or experimental results will be given in Chapter 3, 4 and 5 as justifications.

1.5 Publications during This PhD Project

Some of the results of this PhD project were published or accepted for publication in journals and conference proceedings. These publications are listed below.

1- **W. Zhang**, A. M. Cantarellas, J. Rocabert, A. Luna, and P. Rodriguez, "Synchronous Power Controller with Flexible Droop Characteristics for Renewable Power Generation Systems," *IEEE Trans. Sustain. Energy*, vol. 7, no. 4, pp. 1572–1582, 2016.

2- **W. Zhang**, K. Rouzbehi, A. Luna, G. B. Gharehpetian, and P. Rodriguez, "Multi-terminal HVDC grids with inertia mimicry capability," *IET Renew. Power Gener.*, vol. 10, no. 6, pp. 752–760, 2016.

3- **W. Zhang,** D. Remon, and P. Rodriguez, "Frequency support characteristics of grid-interactive power converters based on the synchronous power controller," *IET Renew. Power Gener.*, 2016. Accepted for publication.

4- **W. Zhang**, D. Remon, A. M. Cantarellas, and P. Rodriguez, "A Unified Current Loop Tuning Approach for Grid-Connected PV Inverters," *Energies (special issue Distrib. Renew. Gener.)*, vol. 9, no. 9, 2016.

5- **W. Zhang**, D. Remon, A. M. Cantarellas, A. Luna, and P. Rodriguez, "Dynamics Estimation and Generalized Tuning of Stationary Frame Current Controller for Grid-Tied Power Converters," *Eur. Power Electron. Drives (EPE Journal)*, vol. 26, no. 3, pp. 85–95, 2016.

6- **W. Zhang**, D. Remon, J. I. Candela, A. Luna, and P. Rodriguez, "Grid-connected Converters with Virtual Electromechanical Characteristics – Experimental Validation," *CSEE J. Power Energy Syst.*, 2016. Accepted for publication.

7- K. Rouzbehi, **W. Zhang**, J. I. Candela, A. Luna and P. Rodriguez, "Unified Reference Controller for Flexible Primary Control and Inertia Sharing in Multi-Terminal VSC-HVDC Grids," *IET Gener. Transm. Distrib.*, vol. 11, no. 3, pp. 750–758, 2017.

8- **W. Zhang**, D. Remon, J. Rocabert, A. Luna, J. I. Candela, and P. Rodriguez, "Frequency Support Properties of the Synchronous Power Control for Grid-Connected Converters," in *IEEE Energy Conversion Congress and Exposition (ECCE)*, 2016.

9- **W. Zhang**, K. Rouzbehi, J. I. Candela, A. Luna, G. B. Gharehpetian, and P. Rodriguez, "Autonomous Inertia-Sharing Control of Multi-Terminal VSC-HVDC Grids," in *IEEE PES General Meeting*, 2016.

10- **W. Zhang**, K. Rouzbehi, J. I. Candela, A. Luna, and P. Rodriguez, "Control of VSC-HVDC with Electromechanical Characteristics and Unified Primary Strategy," in *IEEE Energy Conversion Congress and Exposition (ECCE)*, 2016.

11- D. Remon, A. M. Cantarellas, **W. Zhang**, J. I. Candela, and P. Rodriguez, "Enhancement of the Stability of a Distribution System through Synchronous PV," in *IEEE PES General Meeting*, 2016.

12- **W. Zhang**, D. Remon, A. Mir, A. Luna, J. Rocabert, J. I. Candela, and P. Rodriguez, "Comparison of Different Power Loop Controllers for Synchronous Power Controlled Grid-Interactive Converters," in *IEEE Energy Conversion Congress and Exposition (ECCE)*, 2015, pp. 3780–3787.

13- **W. Zhang**, A. Luna, J. I. Candela, J. Rocabert, and P. Rodriguez, "An Active Power Synchronizing Controller for Grid- Connected Power Converters with Configurable Natural Droop Characteristics," in *IEEE 6th International Symposium on Power Electronics for Distributed Generation Systems (PEDG)*, 2015, pp. 1–7.

14- D. Remon, A. M. Cantarellas, J. D. Nieto, **W. Zhang**, and P. Rodriguez, "Aggregated Model of a Distributed PV Plant Using the Synchronous Power Controller," in *IEEE 24th International Symposium on Industrial Electronics (ISIE)*, 2015, pp. 654–659.

15- K. Rouzbehi, J. Zhu, **W. Zhang**, G. B. Gharehpetian, and P. Rodriguez, "Generalized voltage Droop Control with Inertia Mimicry Capability – Step Towards Automation of Multi-terminal HVDC Grid," in *International Conference on Renewable Energy Research and Application (ICRERA)*, 2015, pp. 1556–1561.

16- K. Rouzbehi, **W. Zhang**, J. I. Candela, A. Luna, and P. Rodriguez, "Generalized Voltage Droop Strategy for Power Synchronization Control in Multi-Terminal DC Grids -an Analytical Approach," in *International Conference on Renewable Energy Research and Application (ICRERA)*, 2015, pp. 1568–1574.

17- **W. Zhang**, C. Citro, A. M. Cantarellas, D. Remon, A. Luna, and P. Rodriguez, "Tuning of proportional resonant controllers for three phase PV power converters with LCL+trap filter," in *IEEE PES T&D Conference and Exposition*, 2014, pp. 1–5.

18- **W. Zhang**, A. M. Cantarellas, D. Remon, A. Luna, and P. Rodriguez, "A proportional resonant controller tuning method for grid connected power converters with LCL+trap filter," in *International Conference on Renewable Energy Research and Application (ICRERA)*, 2014, pp. 445–450.

CHAPTER 2.

The Synchronous Power Controller

The Synchronous Power Controller (SPC) is the basis of the studies presented in this PhD dissertation, and the design of the controllers in Chapter 3 to 5 considers different blocks of the SPC in detail. The overall control framework of the SPC is introduced and explained in this chapter, followed by its main features in comparison to other SGEC methods.

2.1 The Synchronous Power Controller for Grid Connected Power Converters

The SPC endows grid connected voltage source converters (VSC) with virtual electromechanical characteristics, as an emulation and enhancement of synchro-nous generators [41].

The electromechanical characteristics of synchronous generators can be split into two aspects, the stator output impedance (electrical) and the rotor inertia (mechanical). The former one defines the fundamentals of electrical interaction with the grid in terms of active and reactive power exchange, which also contributes to grid synchronization, power sharing and unbalance compensation, etc. The latter one defines the power-frequency dynamics in power systems and contributes to the frequency stabilization.

The exchange of active and reactive powers between two voltage sources e and v is written as:

$$P = \frac{EV}{Z}\cos(\phi - \delta) - \frac{V^2}{Z}\cos(\phi), \tag{2.1}$$

$$Q = \frac{EV}{Z}\sin(\phi - \delta) - \frac{V^2}{Z}\sin(\phi), \tag{2.2}$$

where E and V are the rms of e and v, $Z\angle\phi$ the impedance between the two sources, and δ the phase-angle difference between e and v, and it is known as load-angle.

For common synchronous machines, considering a mainly inductive output impedance and the synchronized condition (a small value of δ), (2.1) and (2.2) can be simplified as:

$$P = \frac{EV}{X}\delta = P_{\max}\delta\,, \tag{2.3}$$

$$Q = \frac{V(E-V)}{X}\,. \tag{2.4}$$

As shown in (2.3) and (2.4), synchronous machines regulate the active and reactive powers by adjusting the load-angle and magnitude of the electromotive force through the governor and exciter, respectively. Similarly, the SPC controls the active and reactive powers by adjusting its inner voltage phase-angle and magnitude, respectively, like a synchronous machine, rather than the conventional in-phase and in-quadrature current control performed in the decoupled rotating (dq) reference frame.

The overall control architecture for grid connected power converters based on the SPC and external droop controllers is shown in Fig. 2.1.

The control scheme contains the Pulse-Width Modulation (PWM) block, the SPC's electrical part, the Voltage-Controlled Oscillator (VCO), the SPC's mechanical part, the reactive power controller, the frequency droop controller and the voltage droop controller. The power loop controller (PLC) and the virtual admittance determine the main characteristics of the SPC, which correspond to the mechanical and electrical part of synchronous machines, respectively.

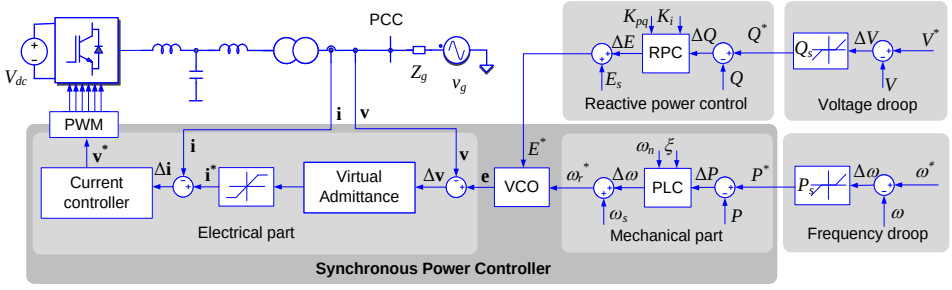

Fig. 2.1. Control of grid connected power converters based on the SPC.

2.1.1 The SPC's mechanical part

The power loop controller emulates the power-frequency regulation of a synchronous machine, and generates a virtual synchronous frequency ω_r^*. Inertial characteristics are given by the power loop controller, which can have multiple options in the control structure.

For traditional synchronous machines, the damping of the electromechanical loop is provided by a damper winding, which may be affected by several electrical or mechanical constraints. Besides, a ramp limiter for the input mechanical power can also be used to avoid oscillations.

For renewable power generation plants, the electromechanical characteristics of grid connected power converters can be virtually implemented by designing proper controllers. Therefore, the damping in power converters is possible to be further optimized based on a virtual implementation in its controllers. In addition, considering that the power input of renewable power generation plants is more irregular than in traditional plants, having an effective damping in the power converter becomes more important.

In summary, inertia and damping characteristics should be both considered in designing the power loop controller of the power converter. A good option is to use a first-order low-pass filter for the power loop controller, which results in a power-frequency relationship exactly like the swing equation of synchronous machines, which is:

$$P_m - P_e = \omega_s (Js + D)\omega, \tag{2.5}$$

where P_m and P_e are the mechanical and electrical power, respectively, J the moment of inertia, ω_s the rated rotor angular speed, D the damping factor and ω the rotor angular speed.

In case of the converter control, one can set P_m as the power reference P^* and P_e as the power measurement P, and ω as the angular frequency of the virtual electromotive force. In such a case, the inertia and damping characteristics can be emulated.

2.1.2 The voltage controlled oscillator (VCO)

The VCO block generates the virtual electromotive force **e** using ω_r^* and the magnitude reference E^* as rotation speed and amplitude references, respectively. In case that the control of the electrical part is realized in the stationary frame, the VCO can be written as:

$$\mathbf{e} = \begin{bmatrix} e_\alpha \\ e_\beta \end{bmatrix} = \begin{bmatrix} E^* \cos(\omega_r^* t) \\ E^* \sin(\omega_r^* t) \end{bmatrix}, \tag{2.6}$$

where the phase-angle of **e** is obtained by integrating ω_r^*.

2.1.3 The SPC's electrical part

In many low-voltage grids, where several converters are connected in parallel, the grid impedance is not necessarily inductive and difficult to be estimated. The SPC uses a virtual admittance structure to define the output impedance to ensure a high X-R ratio. In a single-phase system, the effect of the virtual admittance can be described by:

$$i_{grid} = \frac{1}{R + sL}(e - v), \tag{2.7}$$

where i_{grid} is the current injected to the grid by the converter, and L and R the inductive and resistive components of the virtual admittance, respectively.

By presenting an output reactance and resistance, which are both adjustable, the power converter will play a key role in performing load sharing and will present a natural droop characteristic for grid voltage support.

To realize (2.7), a current controller is needed. Then (2.7) becomes (2.8).

$$i_{ref} = \frac{1}{R + sL}(e - v), \tag{2.8}$$

where i_{ref} is the reference for the current controller.

2.1.4 Reactive power and droop control

As shown in Fig. 2.1, the reactive power controller (RPC) and the outer *P-f* and *Q-V* droop loops are also needed in power converters as complementary blocks in addition to the SPC. A proportional integral (PI) controller is usually used as the RPC, which can be described as:

$$E^* = E_s + (Q^* - Q)(K_{pq} + \frac{K_i}{s}), \tag{2.9}$$

and the outer droop controllers are expressed as:

$$P^* = P_s + (\omega^* - \omega)k_{DP}, \tag{2.10}$$

$$Q^* = Q_s + (V^* - V)k_{DQ}. \tag{2.11}$$

Droop control defines the steady-state *P-f* and *Q-V* relationship for a generation unit to meet the transmission system operator (TSO) requirements, and it is also necessary for forming an isolated grid.

The virtual admittance determines the inherent *Q-V* droop characteristics, and the power loop controller of the SPC determines the inherent *P-f* droop characteristic. Nevertheless, outer *P-f* and *Q-V* droop controllers are still needed to modify the inherent droop characteristics and define the overall droop gains. The schemes for the outer droop controllers of a grid connected power converter are shown in Fig. 2.2. Based on the synchronization mechanism of the SPC, the grid frequency estimation will be provided by the output of the power loop controller. K_{DP} and K_{DQ} define the droop gain for each controller. In practice, dead-bands can be used in the droop loops to disable the droop controllers around the nominal voltage and frequency values.

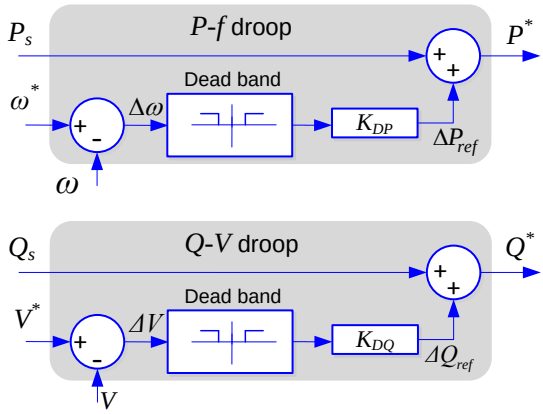

Fig. 2.2. Voltage and frequency primary control.

2.2 Differentiating SPC from Other SGEC Methods

Compared to other SGEC methods, the main features of SPC can be generalized as follow:

1- PLL-less power-based grid synchronization
2- Power loop controller for inertia emulation with multiple options
3- Virtual admittance
4- Multiple and selective virtual admittances
5- Multiple and selective power loop controllers

The first four points (marked in bold) are addressed in this dissertation. In detail, the first two points are shown in Chapter 4 and 5, while the latter two points are shown in Chapter 3.

2.2.1 PLL-less power-based grid synchronization

A SPC-based power converter synchronizes with the grid through a synchronization system based on power balancing instead of estimating the grid voltage phase-angle. The presented system stems from the principle that a power converter can interact with the grid like a synchronous generator, where the balance between the power generation and consumption is naturally kept through the speed variation of the rotor.

The mathematical model of the active power control loop of the SPC is shown in Fig. 2.3. It is a generalized modeling of the active power control mechanisms based on the control structure of Fig. 2.1.

The synchronous angular speed ω is adjusted according to the error in the power converter's power balance regulation, which will further modify the load-angle δ to regulate

generated active power. In this way, even though the grid voltage phase-angle θ_{grid} is unknown and can be variable in a realistic operation, ω can always be adjusted to eliminate the power control error, and meanwhile maintains the synchronization with the grid frequency ω_g. $G_{PLC}(s)$ represents the transfer function between the active power control error, ΔP, and ω, and P_{max} is the gain between δ and the generated active power P, which is defined in (2.3).

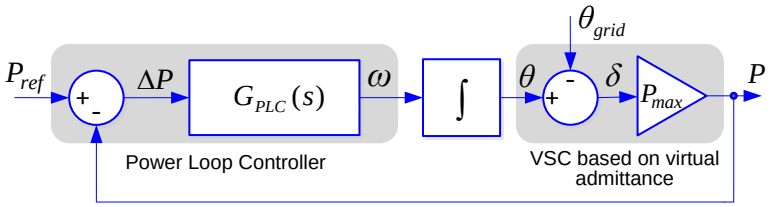

Fig. 2.3. Mathematical model of the SPC's active power control.

Therefore, the power converter's synchronization is not realized by a direct voltage characteristics estimation loop, like a phase-locked loop (PLL) or a frequency-locked loop (FLL), instead, the power loop controller, virtual admittance and current controller work altogether to achieve the power converter synchronization based on a power balance principle in the virtual rotating system.

Unlike the conventional power converter controllers, which require a dedicated synchronization block (PLL or FLL) and a dedicated power controller, the power control loop of the SPC performs synchronization as well as active power control, as naturally occurs in a synchronous machine. In this way, it is possible to provide inertial characteristics to the power converter by properly configuring its power loop controller, while a PLL is not used. This is a clear advantage, since the power converter will be able to operate without being affected by any malfunction of the PLL [14], [15]. In cases of grid faults, a power system can experience sudden phase-angle jumps, which produces a transient in the PLL, and further undesired peculiar transients in the current controller. By using the SPC, the control dynamics are not affected by the genuine dynamics of the PLL or the FLL.

2.2.2 Power loop controller for inertia emulation

Unlike those proposals that implement inertia by using an extra control loop [20]–[23], the SPC defines inertia in the power loop controller. Hence, the inertial effect is not dependent on the estimation of the frequency in the connection to an external grid. When a SPC-based power converter is disconnected from the main, it is able to maintain an islanded operation mode, without switching to any additional control scheme, and keep showing inertial characteristics.

It is worth noting that the structure of the power loop controller, $G_{PLC}(s)$, can have multiple options as long as it leads to a closed-loop transfer function that is similar to:

$$\frac{\partial P}{\partial P_{ref}}(s) = \frac{P_{\max} \big/ J\omega_s}{s^2 + \frac{D}{J}s + P_{\max} \big/ J\omega_s}, \tag{2.12}$$

which is the second-order transfer function based on the swing equation (2.5). In detail, the denominator of the resulting transfer function should maintain the second-order canonical form shown in (2.12) in order to calculate proper values for the natural frequency and damping factor of the transfer function, and thereby emulating given values for the inertia and the damping characteristics. This topic will be further discussed in Chapter 4.

2.2.3 Virtual admittance

Regarding design of the power converter's inner control loops, direct modulation, as in [25]–[36], or voltage-current double-loop controller, as in [37], [38], could be used. However, direct modulation is unable to limit the converter output voltage or injected current, and the double-loop solution also poses several issues, such as the voltage source fighting in parallel connected power converters. Besides, these strategies do not emulate the output impedance of synchronous machines, and thus do not naturally contribute to load sharing, and need impedance estimation when the converter is connected to low *X*-*R* ratio networks. Since the impedance estimation becomes challenging when several generation units are connected in parallel, it is useful to emulate the output impedance of synchronous machines in the control design.

The SPC uses a virtual admittance structure in its inner loops. The overall power transfer impedance can be dominated by the virtual admittance as long as the short circuit ratio (SCR) is not too small. Therefore, impedance estimation in low *X*-*R* ratio networks is not needed, since the virtual admittance presents a dominantly inductive characteristic with an *X*-*R* ratio much greater than 1. Moreover, the use of a back-up PLL as in [14] for start-up or severe fault conditions is not necessary thanks to the adjustable virtual admittance, which avoids complexity in the control design.

There are mainly two ways to emulate the stator impedance of synchronous machines, i.e., by implementing either a virtual impedance or a virtual admittance, as shown in Fig. 2.4.

In many works published in the literature [10], the stator output impedance of synchronous machines is emulated by means of using a virtual impedance structure, as shown in Fig. 2.4(b), and it can be written as:

$$v_{ref} = e - i(R + sL) \cdot \tag{2.13}$$

The time derivative operator in (2.13) causes difficulties in practice. It has various forms for practical implementation. In order to deal with the derivative term contained in the structure, a low-pass filter can be added to process the current measurement, or a fundamental frequency inductor ($j\omega_s L$) can be used as a compromise. With a low-pass filter, the accurate emulation of the impedance cannot be achieved due to phase shifts and delays.

Besides, the fundamental frequency inductor is not effective in the whole frequency range [45].

In contrast, the SPC contains the virtual admittance shown in (2.8) and in Fig. 2.4(a), which is a low-pass structure by itself. It uses a voltage measurement to generate a current reference, and does not contain any derivative operator for processing voltage measurement, which does not entail difficulties regarding practical implementation.

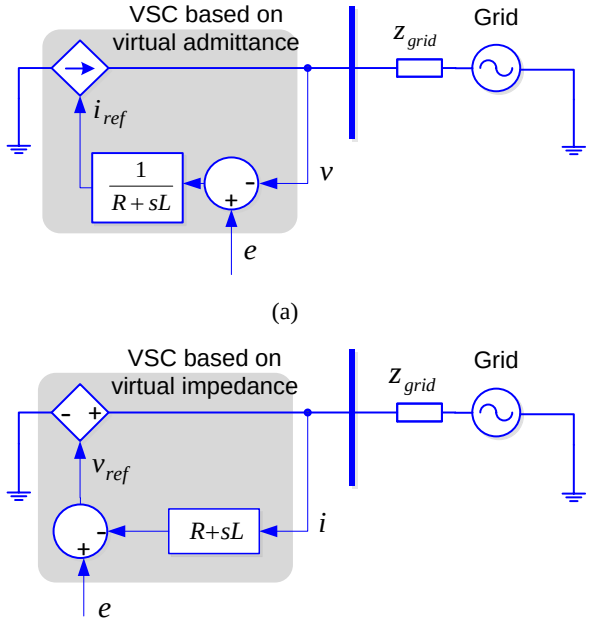

Fig. 2.4. Two strategies for emulating the electrical part of synchronous machines: (a) VSC based on virtual admittance (a main feature of the SPC), and (b) VSC based on virtual impedance.

Moreover, another advantage of the admittance structure lies in the implementation of the inner loops. Only a current control loop is needed in the virtual admittance structure, while for virtual impedance implementation, a voltage-current cascaded double control loop is necessary. It can be expected that the tuning of the controllers becomes more difficult when voltage and current controllers are both needed to avoid dynamics coupling between the voltage and current loops. The bandwidth of the impedance loop has a relatively small high bound, since it is limited by the inner control loops. Then the fast voltage support is hence difficult to be achieved. Therefore, a greater delay occurs in the inner loops if the virtual impedance (2.13) is used.

The virtual admittance also contributes to the start-up of the SPC-based power converters. By a proper conditioning of the admittance parameters, namely R and L, a smooth start-up and grid connection can be achieved.

Fig. 2.5 shows a simulated start-up process as an example. In order to limit the current transient at the moment of connecting the power converter to the grid, the initial values for

R and *L* are set significantly greater than the nominal ones, as Fig. 2.5(c) and (d) show.

In Fig. 2.5, the power converter is connected to the grid and its current control is enabled to make the injected current equal to zero at 0.11 s. As Fig. 2.5(a) shows, the injected current experiences a short transient in the power converter connection, however the current magnitude is within an acceptable range thanks to the high value set to the *R* and *L* before the connection. The grid synchronization of the power converter is completed at 0.35 s. From such a time, the values of *R* and *L* start to be reduced gradually to their nominal values during 1 s. Once the nominal values of *R* and *L* are reached, at 1.6 s, the converter can operate normally and increases the active power injection to its nominal value, as Fig. 2.5(b) shows.

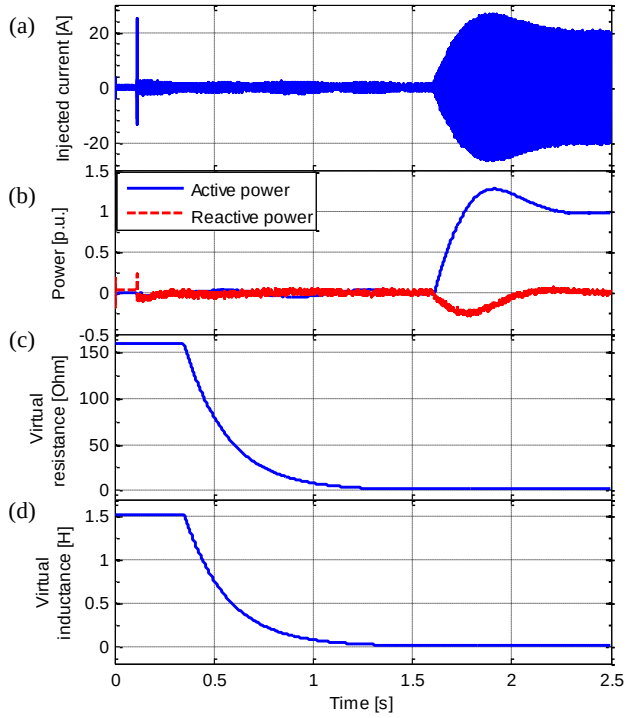

Fig. 2.5. Grid connection start-up process of a SPC-based power converter using virtual admittance conditioning: (a) current injected by the power converter, (b) active and reactive powers injected by the power converter, (c) the value of the virtual resistance, (d) the value of the virtual inductance.

A zoom-in of the start-up process at 0.05 s < t < 0.35 s is shown in Fig. 2.6, in which the details of synchronization process are shown. As shown in Fig. 2.6(c) and (d), both α and β components of the virtual electromotive force *e* are gradually shifted to be synchronized with the grid voltage *v* in several grid cycles.

It is worth mentioning that the transition time parameters can be predefined in the embedded power converter controller or given by other high-level controllers.

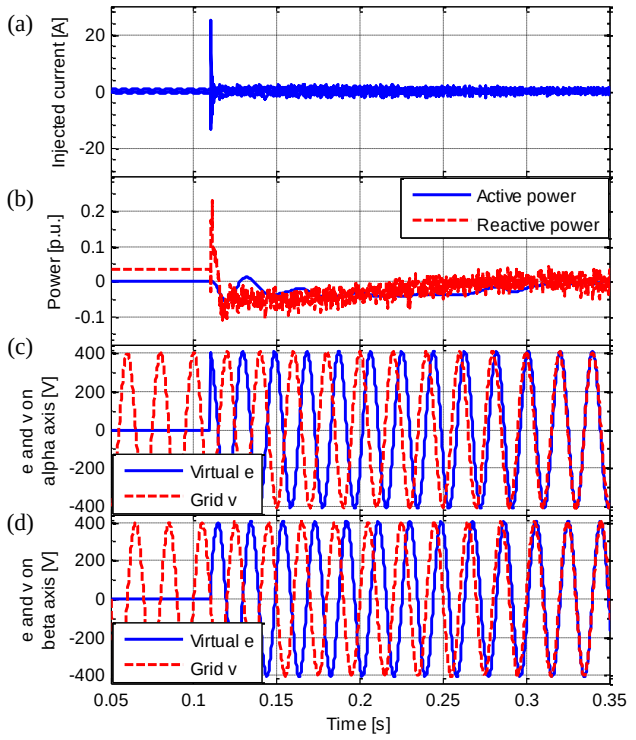

Fig. 2.6. Grid synchronization process of a SPC-based power converter: (a) current injected by the power converter, (b) active and reactive powers injected by the power converter, (c) inner virtual synchronous frequency and grid voltage on α-axis, (d) inner virtual synchronous frequency and grid voltage on β-axis.

2.2.4 Multiple and selective virtual admittance

Based on the SPC, the stator output admittance can be virtually implemented as (2.8), and then several admittances can be used for processing different voltage components. For example, an asymmetrical faults can occur in the electrical grid, which results in unbalanced voltage sags. In order to support the unbalanced grid voltage, both positive- and negative-sequence reactive currents should be injected during the asymmetrical fault. Therefore, different impedance values (L and R) for the positive- and negative-sequence voltages can be used in order to achieve different levels of positive- and negative-sequence reactive current injection during the unbalanced voltage sags. This topic will be further discussed in Chapter 3.

2.3 Summary of the Chapter

The SPC emulates and enhances the electrical and mechanical parts of actual synchronous machines, and presents characteristics such as virtual inertia, damping and

output impedance. It includes multiple control loops, which are, from the inner to outer, the PWM, the current control, the virtual admittance, the VCO and the power loop control.

Compared to other methods that emulate synchronous machines, the SPC shows practical advantages in the synchronization mechanism, inertia emulation method, and inner loops controllers. Moreover, the SPC offers an original capability of performing selective control for different current components. These features will be elaborated and demonstrated in the Chapters 3 to 5.

CHAPTER

3.

The Virtual Admittance

This chapter develops a virtual admittance control structure, which is an essential part of the Synchronous Power Controller (SPC). Except for the emulation of the output impedance of the synchronous generators, extra function of voltage support under asymmetrical grid faults is also added. Since the implementation of virtual admittance entails an inner current loop controller, a unified current loop tuning approach is also developed in this chapter.

3.1 The SPC's Virtual Admittance

According to grid code requirements, grid connected power converters have to be capable of getting through grid fault scenarios in order to let generation units keep connected to the grid under such adverse conditions, and further provide ancillary services to support the grid voltage and frequency. This chapter presents a virtual admittance controller aimed to provide voltage support under asymmetrical grid faults. By using independent and selective admittances for positive- and negative-sequence current injection, the unbalanced voltage can be significantly conditioned during asymmetrical faults. This controller is based on the general control framework of the SPC, which is able to emulate and enhance the electrical and mechanical characteristics of synchronous generators.

3.1.1 Tri-path selective admittances

The SPC's virtual admittance block, as Fig. 2.1 in Chapter 2 shows, defines an output admittance for the power converter equivalent to the output impedance of a synchronous generator. The admittance structure used in the admittance block can be written as:

$$i^* = \frac{e - v}{R + sL}. \tag{3.1}$$

As an enhancement to the output impedance of a synchronous generator, multiple and selective admittances are proposed to be built up in this block, as shown in Fig. 3.1.

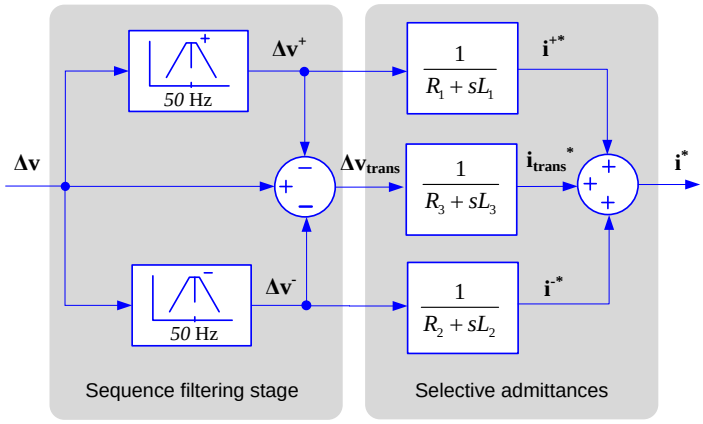

Fig. 3.1. Virtual admittance block for positive- and negative-sequence current injection.

In many cases, the asymmetrical faults that occur in the electrical grid result in unbalanced voltage sags. In order to support the unbalanced voltage, both positive- and negative-sequence current should be injected during the faults. Therefore, different impedance values for the positive- and negative-sequence signals can be used in order to achieve different levels of positive- and negative-sequence current injection during the voltage sags.

In Fig. 3.1, L_1 and R_1 are the inductance and the damping resistance of the impedance for the positive-sequence voltage components at the fundamental frequency, while L_2 and R_2 are the ones for the negative-sequence signals at the fundamental frequency. The rest of the voltage components goes through a third admittance branch (L_3 and R_3), which is named as transient admittance. Considering the possible delay of the filtering stages, this third branch will present a controlled impedance feature during transients. Therefore, the positive- and negative-sequence voltage support possess the same gain during the transient, which is determined by L_3. In addition, the injection of harmonic currents is also determined by this transient admittance, although additional selective band-pass filters and corresponding harmonic impedances might be also implemented. Above all, the current reference generated by the virtual admittance block of Fig. 3.1 results from the sum of three components, that is:

$$\mathbf{i}^{*} = \mathbf{i}^{+*} + \mathbf{i}^{-*} + \mathbf{i}^{*}_{\mathbf{trans}} . \tag{3.2}$$

The proposed virtual admittance has several advantages compared with the physical stator impedance of synchronous generators. Firstly, the positive- and negative-sequence voltages are decomposed and processed through difference admittances. Further, the delay effect of the positive- and negative-sequence components calculation is considered and hence a third general admittance branch is included as a compensation. Moreover, the admittance values of each branch can be online adjusted to meet the requirements in the full operation stage. In detail, the admittance values can be specified much smaller than the nominal ones during grid connection operations to avoid large transient currents caused by the transient lack of synchronization between the grid voltage and the converter inner-built

electromotive force. Then the admittance values can be conditioned to the nominal ones within a specified time of transition.

For separating the positive- and negative-sequence signals, sequence band-pass filters are needed in a former stage. The design of this sequence band-pass filters for this objective has been addressed in many works, such as [69]. In this PhD dissertation the method used is based on the Dual Second-Order Generalized Integrator (D-SOGI), which can be expressed as:

$$\mathbf{v}_{\alpha\beta}^{+} = \frac{1}{2}\begin{bmatrix} f_d & -f_q \\ f_q & f_d \end{bmatrix}\mathbf{v}_{\alpha\beta}, \tag{3.3a}$$

$$\mathbf{v}_{\alpha\beta}^{-} = \frac{1}{2}\begin{bmatrix} f_d & f_q \\ -f_q & f_d \end{bmatrix}\mathbf{v}_{\alpha\beta}, \tag{3.3b}$$

where the resonant and quadrature output of the SOGI are used to generate the positive- and negative-sequence signals. f_d(s) and f_q(s) in (3.3) have the transfer functions as:

$$f_d(s) = \frac{k_{bw}\omega s}{s^2 + k_{bw}\omega s + \omega^2}, \tag{3.4a}$$

$$f_q(s) = \frac{k_{bw}\omega^2}{s^2 + k_{bw}\omega s + \omega^2}, \tag{3.4b}$$

where k_{bw} is the bandwidth parameter and ω is the center frequency.

3.1.2 Design considerations

The virtual admittance block has to be carefully designed in order to achieve the desired performance in both normal operation and voltage sag conditions. Moreover, in addition to meet requirements regarding magnitude of the current injection to be injected during the voltage sags, the time response should also be considered.

A. Requirements of grid codes

Different requirements of reactive current injection during voltage dips can be found in grid codes. Normally, the proportional gain between the reactive current to be injected, I_q, and the voltage drop magnitude, ΔV, is defined to set the minimum requirement for the voltage support, which can be written as:

$$I_q^{pu} \geq -k_q \Delta V_{pu}. \tag{3.5}$$

In this PhD dissertation, a convention of the sign of the reactive current is defined to let the reactive power have a positive value under leading operation, and hence a negative value under lagging operation. In this way, as shown in (3.5), the injected reactive current has a positive value when the grid voltage drops.

In the E.ON grid codes, a proportional gain for reactive current injection, k_q, is required to be equal to or greater than 2, and the operational region for voltage regulation has a higher bound of $1.2V_N$, being V_N the rated grid voltage, which provides voltage limitation as well as voltage support, and a dead band of ±5% around V_N [70].

In the REE (the Spanish electrical grid operator) grid codes, it is required that the voltage support by reactive current injection should be activated once the voltage is lower than 85% of its rated value, and the reactive current should reach 90% when the voltage is lower than 50% of its rated value [71]. Based on these critical points, the proportional gain for reactive current injection, k_q, is calculated to be equal to or greater than 2.57.

Regarding the cases of asymmetrical faults (according to the ENTSO-E grid codes), the fault-ride-through capabilities should be defined by each TSO, while respecting the provisions of the national regulatory authorities [16].

One example of the requirement of the negative-sequence current injection can be found in the German grid codes VDE-AR-N 4120 [72], where it is required a proportional gain k_2 between the magnitude of the negative-sequence current and the negative-sequence voltage given by:

$$I^- = k_2(\Delta V^- - 0.05), \tag{3.6}$$

where k_2 represent the regulation gain, required to be within the range of 0 to 10, and ΔV^- is the incremental change of the magnitude of the negative-sequence voltage. As a complement of this relationship, there is a saturation for the magnitude of the negative-sequence current I^- at 1 p.u..

Moreover, the following specifications can be found in the grid codes regarding requirements of the time response of the voltage support.

In the E.ON grid codes, it is stated that the voltage support service of the generation unit needs to be activated when a voltage dip of over 5% of the rms value of the generator voltage occurs, and the voltage support should occur within 20 ms after fault detection.

In the REE grid codes, it is required that the reactive current injection should be provided within 150 ms after the beginning or clearance of the fault. During this time window, the consumption of reactive power is forbidden as long as the rms voltage drops below 0.85 p.u..

B. Design of the virtual admittance

The virtual admittance of the SPC naturally brings a proportional relationship between the magnitude of the grid voltage drop and the amount of injected reactive current. The interchanged reactive power between two voltage sources *e* and *v* through an impedance can be modeled by (2.4) in Chapter 2. Therefore, the reactive current injected by the generator will be:

$$I_q = \frac{Q}{V} = \frac{E - V}{X}. \tag{3.7}$$

Therefore, the incremental amount of the injected reactive current will be proportional to the change in the voltage magnitude, namely:

$$\Delta I_q = \frac{-\Delta V}{X}. \tag{3.8}$$

In case of SPC-based grid connected power converters, the value of X can be specified simply by setting the value of the inductance in the virtual admittance block. In order to specify a proper value for such a reactance, the per-unit value of X is considered and defined as:

$$X_{pu} = \frac{X}{V^2/S_n} = \frac{2\pi f L}{V^2/S_n}. \tag{3.9}$$

Then (3.8) can be expressed in per unit as:

$$\Delta I_q^{pu} = \frac{-\sqrt{3}\Delta V_{pu}}{X_{pu}}. \tag{3.10}$$

Based on the knowledge on traditional power systems, a typical value for the output impedance of a synchronous generator, X_{pu} can be chosen around 0.3. Then, according to (3.10), the resulting proportional gain, k_q, is calculated to be 5.77. Fig. 3.2 shows the voltage support characteristics when X_{pu} = 0.3 compared with the E.ON and REE grid codes. It can be observed in this figure that the resulting voltage support characteristic is above the requirements of both grid codes.

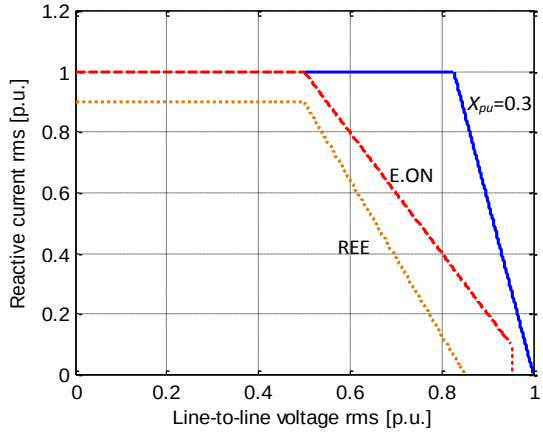

Fig. 3.2. The voltage support characteristics when X_{pu} = 0.3 compared with the grid codes' requirements.

Therefore, Fig. 3.2 gives a clue for specifying the values of the positive-sequence admittance, i.e., the first branch in Fig. 3.1. For the purpose of meeting the grid code requirements, the value of L_1 can be calculated based on (3.9) once X_{pu} is set. The value for R_1 can be chosen through a dynamic study of the admittance transfer function (1st order low-

pass filter) to yield a desired bandwidth with sufficient damping. Since the proportional gain for negative-sequence current injection can be chosen in a range as indicated by (3.6), L_2 might be set different from L_1.

The time response of the virtual admittance block has to be fast enough to achieve an effective voltage regulation. The virtual admittance block contains three selective admittances as shown in Fig. 3.1, for positive-sequence, negative-sequence and transient current regulation, respectively. The transfer function for each branch has the same form and can be generalized as:

$$\frac{\Delta i_{ref}}{\Delta v}(s) = \frac{1}{R_n + sL_n}, \quad n = 1,2,3 \cdot \tag{3.11}$$

Since in this application the input signals for the admittances Δv can be assumed sinusoidal, the time response can be estimated by the response of the magnitude of the two output signals that are generated by giving two sinusoidal input signals in quadrature. The expression is written as:

$$h_V(t) = \sqrt{h_{v\alpha}^2(t) + h_{v\beta}^2(t)}, \tag{3.12}$$

where $h_{v\alpha}(t)$ and $h_{v\beta}(t)$ are the responses to the sinusoidal input signals on α- and β-axis, respectively, and they can be calculated by the convolution:

$$h_{v\alpha}(t) = v_\alpha * h_\delta(t), \tag{3.13a}$$

$$h_{v\beta}(t) = v_\beta * h_\delta(t), \tag{3.13b}$$

where $h_\delta(t)$ is the system impulse response, and v_α and v_β are:

$$v_\alpha = V\cos(\omega t), \tag{3.14a}$$

$$v_\beta = V\sin(\omega t) \cdot \tag{3.14b}$$

In practice, the settling time of $h_V(t)$ has to be calculated with discretized signals (discretized input signal with finite length and discretized transfer function). Providing the calculated response is written as:

$$h_V(k) = \sqrt{h_{v\alpha}^2(k) + h_{v\beta}^2(k)}, \tag{3.15}$$

then the settling time can be calculated by:

$$t_s = T_s \cdot \max\{\forall k \quad s.t. \quad \left|\frac{h_V(k)}{h_V(n)} - 1\right| > \varepsilon_s\}, \tag{3.16}$$

where T_s is the discretizing sampling time, n the total number of the points of the discretized signal, and ε_s the defined steady-state band.

Specifying the values for R_{pu} and X_{pu} to be 0.1 p.u. and 0.3 p.u., respectively, the settling time for the admittance expression, $\frac{1}{R+jX}$, is 21.6 ms, which is calculated according to the aforementioned method, with ε_s = 0.1. This settling time can indicate the response of the transient admittance branch, namely, the second branch of the virtual admittance block in Fig. 3.1. For the other two branches that deal with positive- and negative-sequence voltages, the time response is also dependent on the filtering stage of the virtual admittance block (as shown in Fig. 3.1). The time response of the sequence filtering stages can be determined from (3.3) and (3.4).

Fig. 3.3(a) shows the response of the sequence filter for the negative-sequence rms component for different values of the bandwidth parameter k_{bw}.

According to (3.4), the response for the positive-sequence component will have the same characteristics in time. Therefore, by tuning the k_{bw} in (3.4), the speed for separating the positive- and negative-sequence components of the grid voltage can be easily adjusted.

Fig. 3.3(b) shows how the dynamics of the positive- and negative-sequence current injection during asymmetrical faults is mainly determined by the sequence filtering stage, since the admittance time response is very fast and does not add almost any delay.

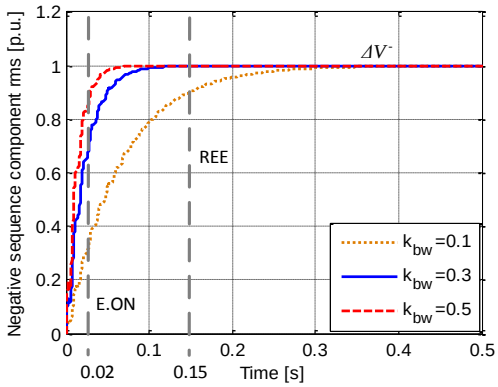

(a)

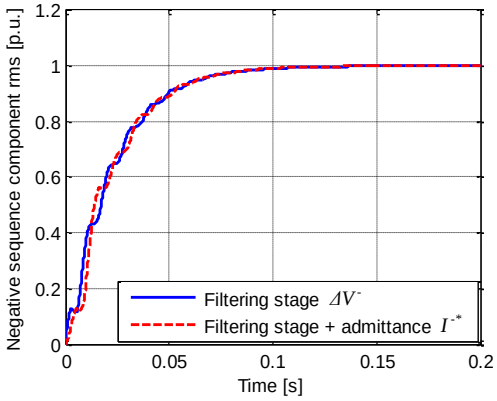

(b)

Fig. 3.3. The time response of (a) the sequence filtering stage of the virtual admittance block under different values of k_{bw}, and (b) the virtual admittance block when k_{bw} = 0.3.

3.1.3 Test results of the SPC's virtual admittance

A. Simulation Results

Simulation tests based on a digital implementation of the proposed controller are presented firstly in this section. A 100 kW two-level three-phase converter connected to a 400 V / 50 Hz grid through a grid link filter is modeled for simulation, as shown in Fig. 3.4. The key parameters for the test setup and controller are listed in Table 3.1. This simulation test system is presented in detail in the Appendix A.1.

The event considered in this simulation test is a 0.43 p.u. of voltage sag in one of the phases of the ac source, and it lasts for 200 ms. According to the aforementioned grid codes, the power converter should remain connected to the grid under such unbalanced voltage drop and the voltage support should be also triggered.

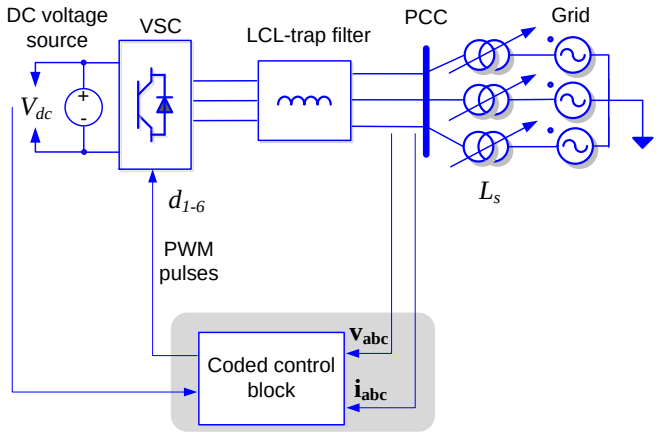

Fig. 3.4. 100 kW grid connected power converter simulation test system.

Table 3.1 Key parameters of the 100 kW SPC-based power converter

Description	Symbol	Value
dc voltage	V_{dc}	750 [V]
sag generator equivalent inductance	L_s	800 [μH]
switching frequency	f_{sw}	3150 [Hz]
virtual resistance	R_{pu}	0.1 [p.u.]
virtual reactance	X_{pu}	0.3 [p.u.]
sequence filtering stage bandwidth	k_{bw}	0.3
SPC's virtual inertia constant	H	5 [s]
SPC's virtual damping factor	ξ	0.7

A generalized expression for the current reference generated by the virtual admittance block can be written as:

$$\mathbf{i}^* = \frac{1}{R+Ls}\left(A_{pos}\Delta\mathbf{v}^+ + A_{neg}\Delta\mathbf{v}^- + A_{trans}\Delta\mathbf{v}_{\mathbf{trans}}\right), \tag{3.17}$$

where L and R are the unified inductance and resistance that can be calculated based on the specified X_{pu} and R_{pu}.

In order to set different values for each sequence admittance in the virtual admittance block, the unified value of resistance and inductance can be modified by different coefficients, as shown in (3.17). In this way the admittance value for each branch can be simply defined by specifying value for the coefficients A_{pos}, A_{neg} and A_{trans}. Therefore, the inductance and resistance in each branch have the values shown in Table 3.2.

Table 3.2 The inductance and resistance in each branch

Description	Symbol	Value
positive sequence resistance	R_1	R/A_{pos}
positive sequence inductance	L_1	L/A_{pos}
negative sequence resistance	R_2	R/A_{neg}
negative sequence inductance	L_2	L/A_{neg}
transient resistance	R_3	R/A_{trans}
transient inductance	L_3	L/A_{trans}

Once X_{pu} and R_{pu} are set to meet requirements in reactive current injection during the faults, A_{pos} can be set to 1 by convenience.

In the experiments, two different sets of values for the virtual admittances are specified. In the first case, the value for A_{neg} was set to 10, which is a significantly greater value than the ones for A_{pos} and A_{trans} (which were both set to 1 by convenience), to clearly boost the negative-sequence current injection in case of unbalanced faults. In contrast, the value for A_{neg} was set to 0.1 in a second case to limit the injection of negative-sequence current injection during unbalanced faults. These very different values for A_{neg}, namely 10 and 0.1, were chosen in this study case to clearly evidence the effect of the negative-sequence admittance value during unbalanced faults However, in real applications, A_{neg} should be determined according to the TSO requirements on the ratio between V^- and I^-.

Working with the first set of values, i.e. with $A_{neg} = 10\ A_{pos}$, it can be clearly appreciated in Fig. 3.5 how the power converter provides a significant support to recover the voltage at the point of common coupling (PCC) (regarding both magnitude and symmetry recovery). By using such a large value for the negative-sequence admittance, the unbalanced voltage at the PCC is almost compensated as Fig. 3.5(b) shows. The highly unbalanced current injected to the grid, shown in Fig. 3.5(c), denotes its large negative-sequence component.

Considering the second set of values, a small value for the negative-sequence admittance is used, $A_{neg} = 0.1\ A_{pos}$, and hence the converter injects a very limited amount of negative-sequence current during the unbalanced fault, which is denoted by the relatively balanced current waveforms shown in Fig. 3.6(c). As a result, the PCC voltage unbalance is almost not compensated during the unbalanced grid fault as Fig. 3.6(b) shows. Setting a low value for A_{neg} can be needed in practice considering current limitations of the power converter. Hence, small size power converters will be mainly responsible for positive-sequence current injection.

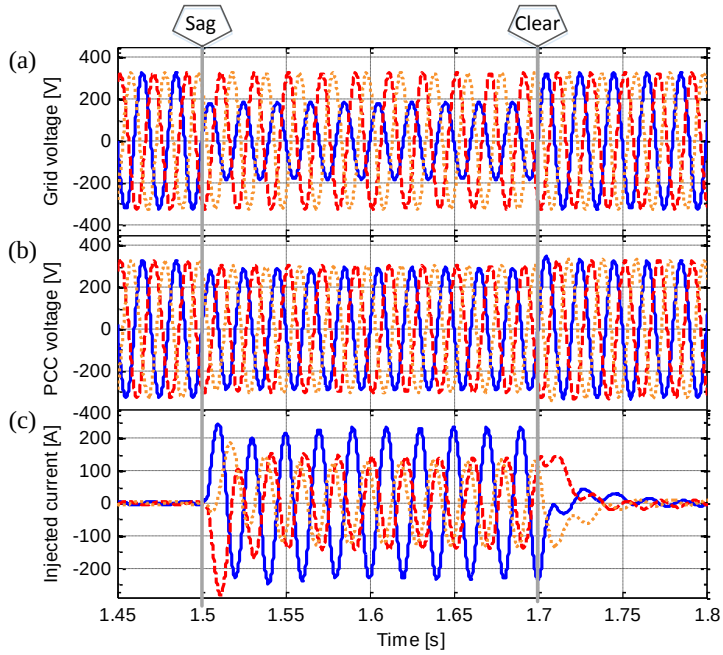

Fig. 3.5. Response of the SPC-based power converter under an asymmetrical grid fault when A_{pos} = 1, $A_{neg} = 10A_{pos}$: (a) grid voltage, and (b) PCC voltage, (c) current injected by the converter.

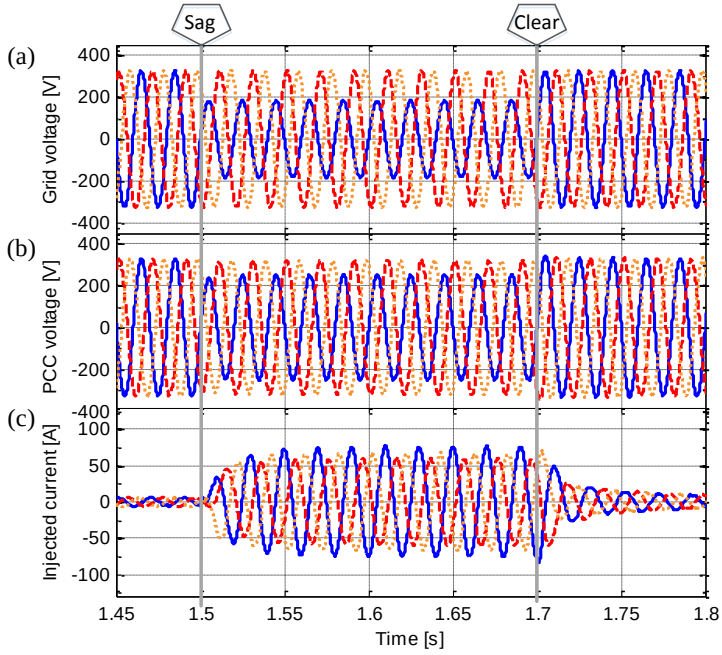

Fig. 3.6. Response of the SPC-based power converter under an asymmetrical grid fault when A_{pos} = 1, $A_{neg} = 0.1A_{pos}$: (a) grid voltage, and (b) PCC voltage, (c) current injected by the converter.

The rms value for the positive- and negative-sequence components of the voltage at the PCC and the injected current are shown in Fig. 3.7.

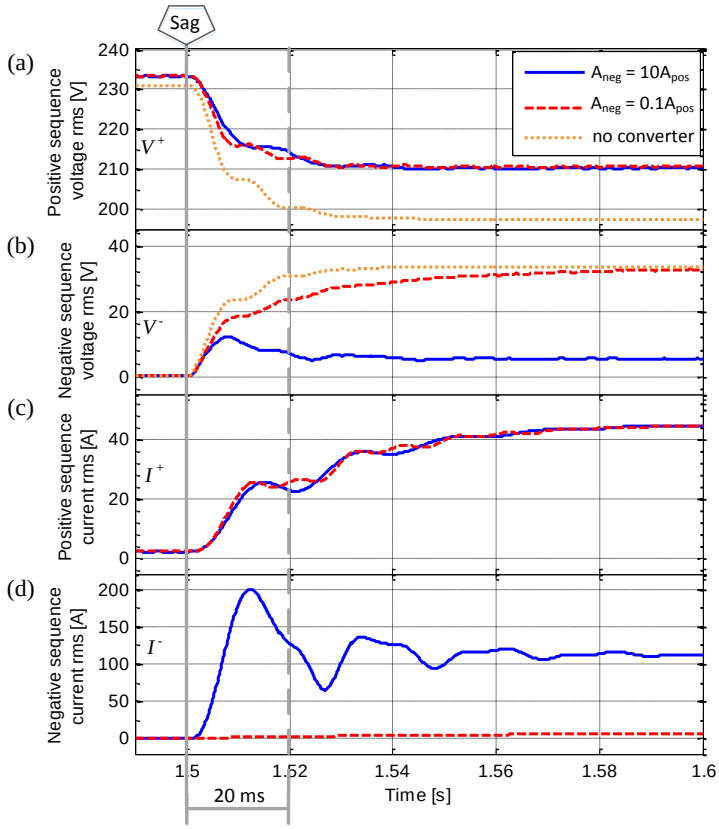

Fig. 3.7. Comparison of the unbalanced voltage support effect of the SPC-based power converter under different negative-sequence virtual admittances: (a) positive sequence PCC voltage rms, (b) negative sequence PCC voltage rms, (c) positive sequence current rms, (d) negative sequence current rms.

Fig. 3.7(a) shows that the positive-sequence voltage is properly supported by the SPC-based power converter with virtual admittance. The drop of the positive-sequence voltage component at the PCC is 8.5% when the power converter is activated, in comparison with 14.1% when the power converter is blocked. Fig. 3.7(b) demonstrates a significant compensation of the unbalanced effect. When A_{neg} = 10, the per-unit rms voltage of the negative-sequence at the PCC during the fault is only 2.35%, a value much smaller than 14.6%, which is the per-unit rms voltage of the negative-sequence component of the voltage at the main grid. Fig. 3.7(d) shows that the rms value of the negative-sequence current injected during the unbalanced fault can be simply adjusted by changing the values for the negative-sequence admittance, i.e. A_{neg}. Fig. 3.7 also shows that the reaction of the converter in presence of the unbalanced fault is less than 20 ms and gets settled within 100 ms, which meets the the grid codes requirements.

Fig. 3.8 shows the effect of the transient admittance branch in the proposed virtual

admittance block. A_{trans} is set to 0 and 1 in two different study cases, while A_{pos} is set to 1 and A_{neg} is set to 10 in both cases. As seen from the Fig. 3.8, the transient admittance contributes to a faster response when the unbalanced fault takes place. The injected current responds faster when the transient admittance is enabled, and both positive- and negative-sequence components of the PCC voltage present a smoother change than in case of disabling the transient impedance. The coherence of the steady-state profiles in each scope of Fig. 3.8 shows that the static performance is not affected by the transient admittance.

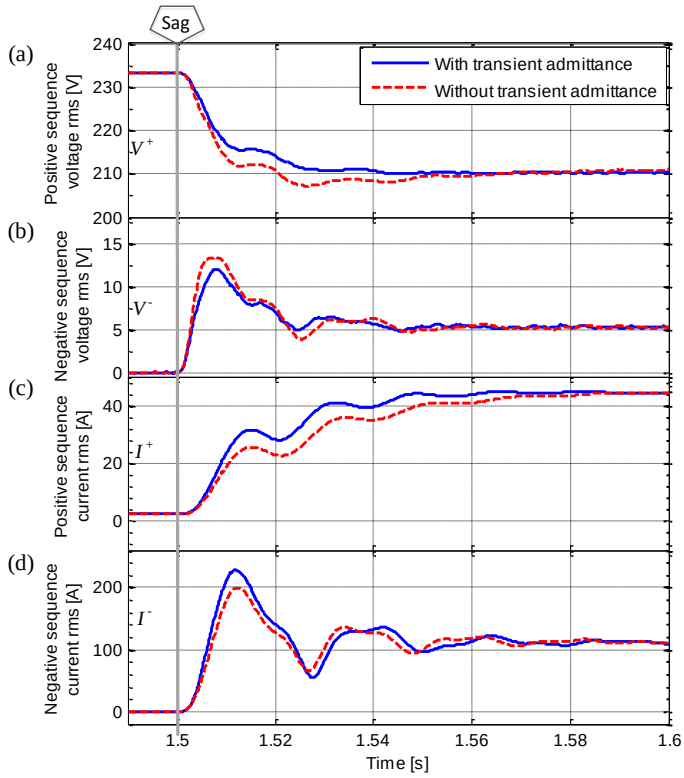

Fig. 3.8. Effect of the transient admittance branch under an asymmetrical grid fault: (a) positive sequence PCC voltage rms, (b) negative sequence PCC voltage rms, (c) positive sequence current rms, (d) negative sequence current rms.

B. Experimental Results

Fig. 3.9 shows the block diagram experimental setup for asymmetrical grid fault tests, where two 100 kW two-level three-phase power converters with the same specifications are connected in parallel and to the utility grid through a sag generator. A dc power source supplies both converters. The parameters for the experimental setup and controllers are the same as the ones used in simulation, shown in Table 3.1. The event considered in the experiments is the same with the simulation tests, namely, a voltage sag of 0.43 p.u. in one of the phases of the ac grid. This experimental setup is presented in detail in the Appendix B.2.

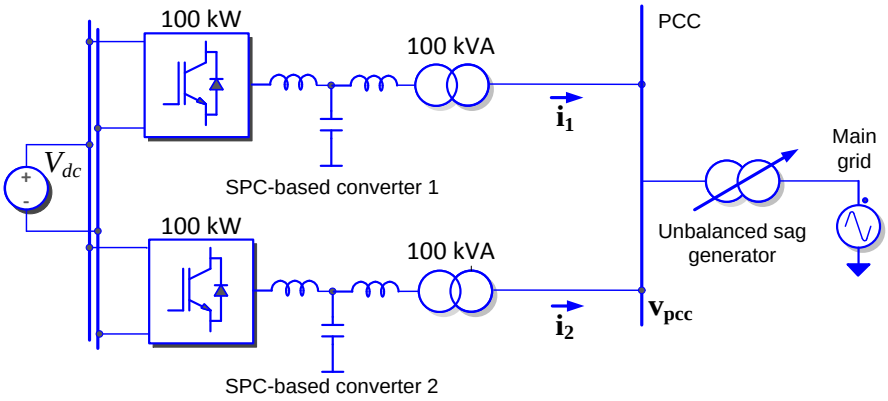

Fig. 3.9. Experimental setup for unbalanced voltage sag tests.

In a first experiment, only one of the two converters is connected, and A_{pos}, A_{neg}, and A_{trans} are set to 1, 10 and 1, respectively. The voltage and current waveforms at the PCC during normal working and under fault conditions are shown in Fig. 3.10. In this experimental test, the voltage sag is started and ended manually and the sag lasts from 6.4 s to 14.4 s.

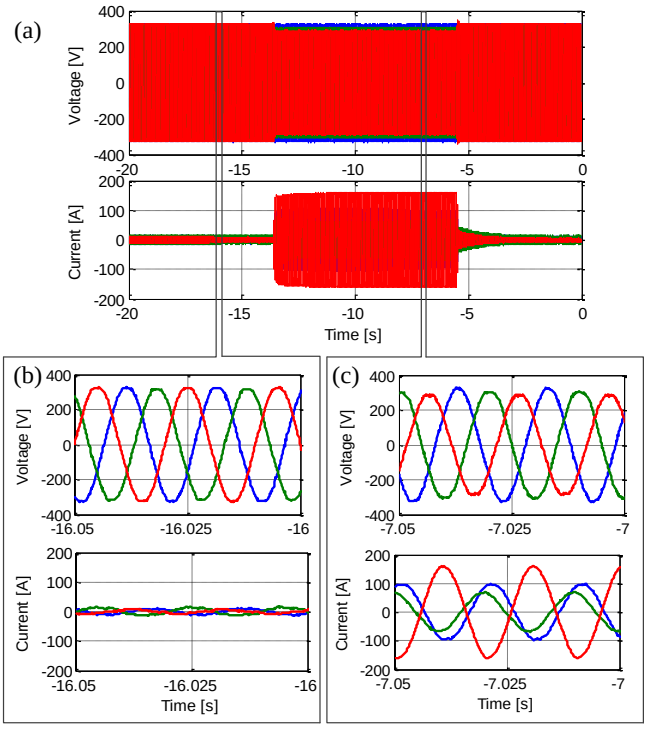

Fig. 3.10. Single SPC-based converter working. The PCC voltage and current injection when A_{pos} = 1 and A_{neg} = 10A_{pos}: (a) the whole experimental process, (b) prior to the fault, (c) during the fault.

Fig. 3.10(a) shows the envelope of the PCC voltage and converter injected current before, during and after the fault. A zoom-in of the pre-fault voltage and current waveforms are

shown in Fig. 3.10(b), while the zoom-in voltage and current waveforms during the fault are shown in Fig. 3.10(c). These plots evidence how the PCC voltage is well supported during the unbalanced fault. There are only minor visible differences in the voltage waveforms magnitude before and during the fault. Therefore, it is demonstrated how the injected negative-sequence current results in relatively balanced voltage waveforms at the PCC.

The recorded data from the oscilloscope were plotted in Fig. 3.11 in order to check the power converter dynamics and a quantitative evaluation of the injected positive- and negative-sequence currents. The positive- and negative-sequence components of the PCC voltage are also calculated.

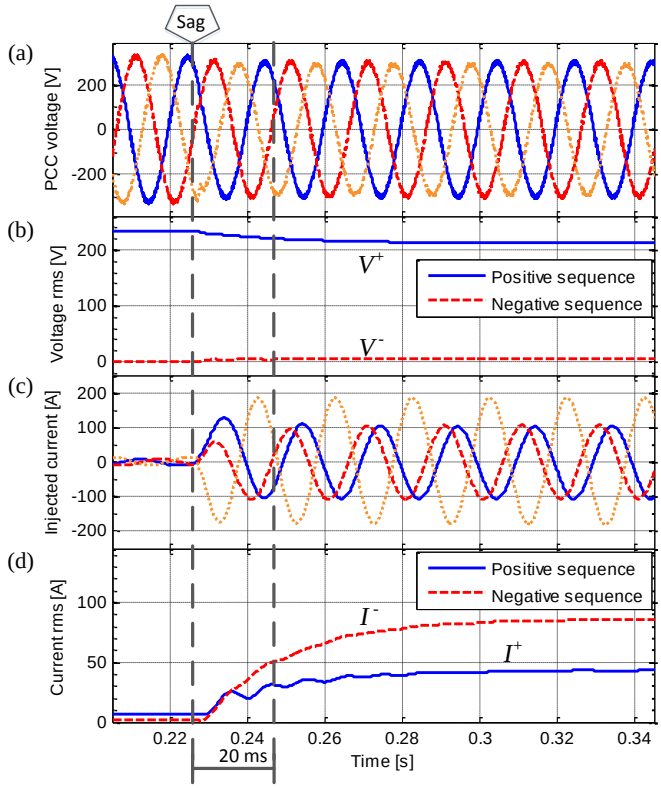

Fig. 3.11. Single SPC-based power converter working. Transient response after the start of an unbalanced sag: (a) voltage at the PCC, (b) positive- and negative-sequence voltage rms, (c) current injected by the converter, (d) positive- and negative-sequence current rms.

From the profiles of the rms current of the positive- and negative-sequence components, as Fig. 3.11(d) shows, the fast reaction of the power converter to support the unbalanced grid voltage can be appreciated. The positive- and negative-sequence current raised to 68% and 62% of the steady-state value, respectively, just 20 ms after of the fault start.

In a second experimental test, both converters are connected to the grid in order to test current sharing performance in front of common disturbances. The positive- and transient-admittance values were set the same for both converters, while different values for A_{neg} were

set for the two power converters, i.e., A_{neg} = 10 A_{pos} and A_{neg} = 0.1 A_{pos}, respectively.

Fig. 3.12 shows the difference in the current injection of the two power converters when different values for A_{neg} are set in both converters. For the converter 1, with A_{neg} = 10, the injected current during the fault has unbalanced waveforms as Fig. 3.12(c) shows, since it contains a large amount of negative-sequence component. While for the converter 2, with A_{neg} = 0.1, the injected current during the fault is relatively balanced, due to the small rate of negative-sequence current injection. Thanks to the combined support provided by both converters, the voltage at the PCC does not experience a significant change in magnitude during the grid fault, which can be seen by comparing Fig. 3.12(b) and (c).

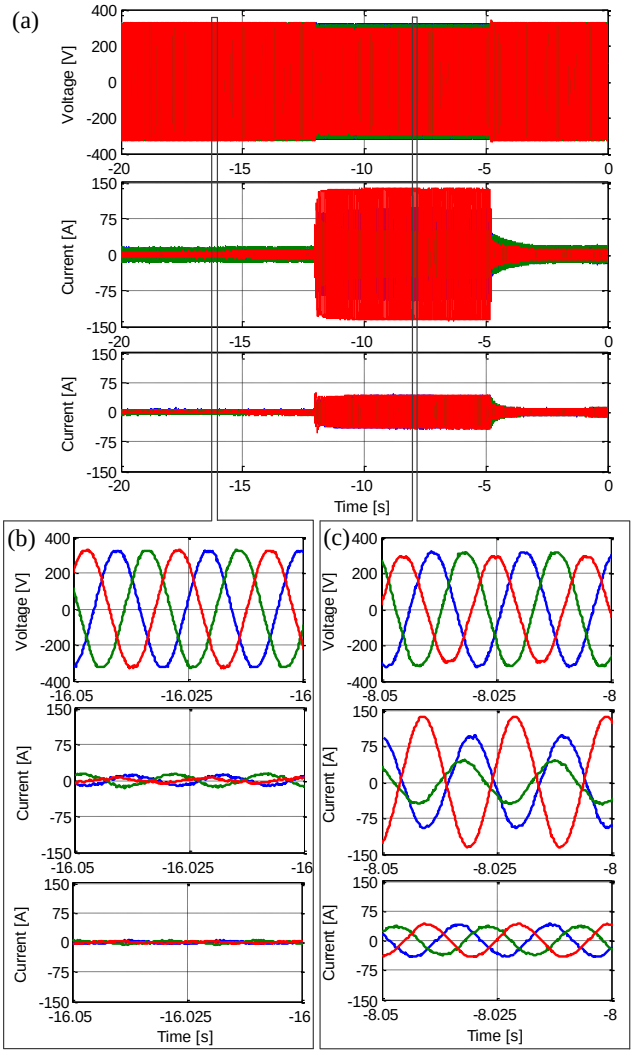

Fig. 3.12. Two SPC-based converters working with different negative-sequence virtual admittances. The PCC voltage and current injection: (a) the whole experimental process, (b) prior to the fault, (c) during the fault.

Fig. 3.13 compares the rms value of the current injected by both converters. Since both of them have the same value for A_{pos}, the rms value of the positive-sequence current component is at the same level in both converters. However, the negative-sequence rms current profiles for both converters exhibit a clear difference in magnitude. It practically demonstrates that negative-sequence current sharing among paralleled converter can be easily adjusted by just setting proper values for A_{neg} in each of them.

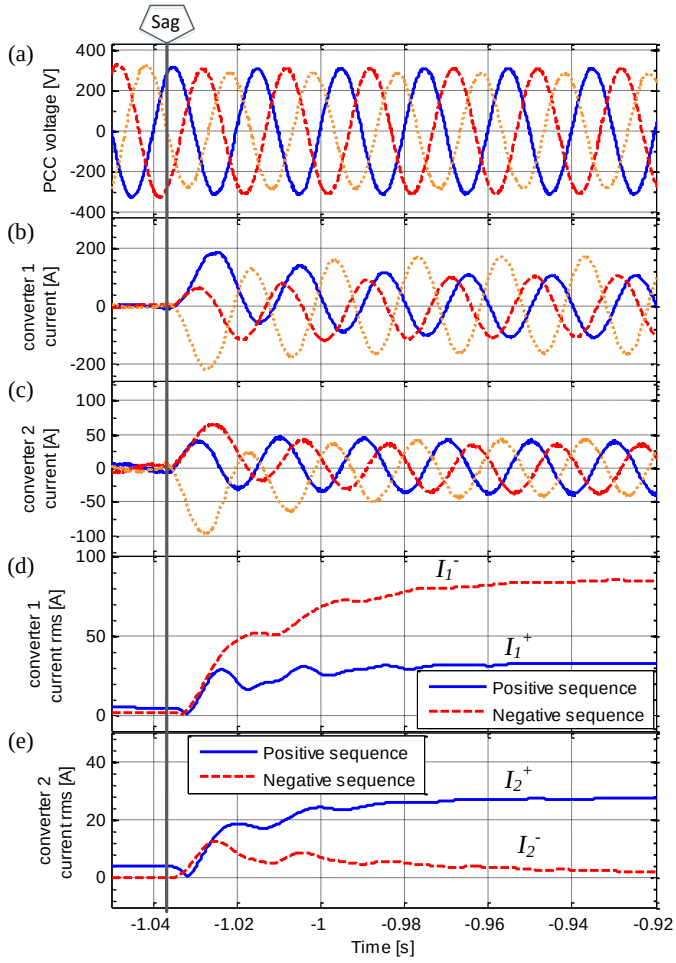

Fig. 3.13. Two SPC-based power converters working with different negative-sequence virtual admittances. The transient responses after the start of an unbalanced sag: (a) voltage at the PCC, (b) current injected by the converter 1, (c) current injected by the converter 2, (d) rms of the positive- and negative-sequence current injected by the converter 1, (e) rms of the positive- and negative-sequence current injected by the converter 1.

Fig. 3.14 shows the rms profile of the positive- and negative-sequence components of the voltage at the PCC and the currents injected by two power converters with different negative-sequence virtual admittances. The positive-sequence voltage drop at the PCC, as

Fig. 3.14(a) shows, is equal to 8.3% of its rated value, which is much smaller than the positive-sequence grid voltage drop, which is equal to 13.8%. Since the two converters have the same value for A_{pos}, the steady-state value of I_1^+ and I_2^+ are close each other as Fig. 3.14(c) shows. However, converter 1 injects much more amount of negative-sequence current than converter 2 as Fig. 3.14(d) shows, due to the high value set for A_{neg} in the former. The negative-sequence voltage component at the PCC increases by 5.2% during the fault. It is worth noting that even though the negative-sequence voltage component at the PCC, as Fig. 3.14(b) shows, is 5.2%, which is smaller than the one in grid voltage (14.6%) during the unbalanced fault, it is greater than the one in the former experiment, when converter 2 was not connected (1.9%). Therefore, the relative influence of converter 1 on the PCC voltage is reduced due to the participation of converter 2.

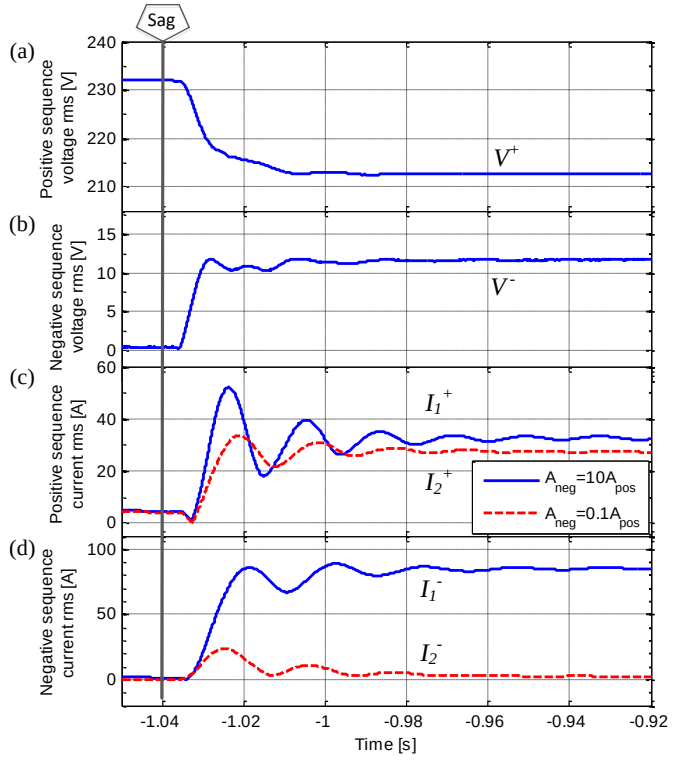

Fig. 3.14. Two SPC-based converters working with different negative-sequence virtual admittances. Comparison of the negative-sequence current injection of the two converters during an unbalanced sag: (a) positive sequence PCC voltage rms, (b) negative sequence PCC voltage rms, (c) positive sequence current rms, (d) negative sequence current rms.

Based on the steady-state rms value for the positive- and negative-sequence voltage and current components, the actual gain of the negative-sequence current injection ($\Delta I^-/\Delta V^-$) obtained from experimental results can be calculated. The actual gains for the two converters are visualized in Fig. 3.15 and compared with requirements in the VDE grid codes (considering a 5% dead-band for each one). As it can be observed in Fig. 3.15, the characteristics of the two converters are within the range of the grid codes requirements (the shadow area).

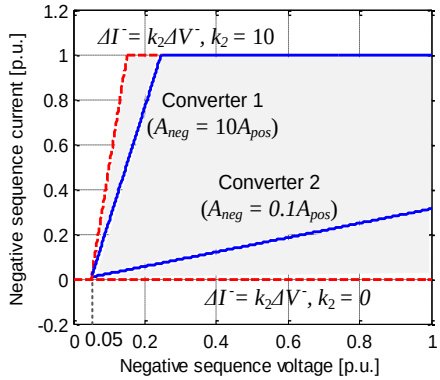

Fig. 3.15. Two SPC-based power converters working with different negative sequence virtual admittances. The V^- - I^- slope of the two converters compared with the VDE grid codes.

3.2 Inner Current Loop Controller

The performance of the current controller is critical for the implementation of the virtual admittance. Besides, considering that a current regulating loop is largely employed in various kinds of control strategies for grid-tied converters [73]–[75], a generalized and optimized approach for tuning the current controller of power converters is needed.

Regarding current regulators, the Proportional Resonant (PR) controller on the stationary frame has been used in different applications showing its effectiveness [76]–[81]. Compared with the proportional integral (PI) controllers on the synchronous frame [82], [83], the advantages of PR controller include the reference frame transformation with reduced computational burden in digital implementation [84], the simplicity in positive/negative sequence and harmonics control [85], and zero steady-state error in single-phase systems. Moreover, the grid synchronization algorithm applied in the stationary reference frame control paradigm is dependent on grid frequency, which is more stiff than the grid voltage phase-angle [86].

The influence of the PR controller gains on the characteristics of the power converter response has been well analyzed in [85], [87], [88]. The tuning of the controller gains is critical for the stability and dynamics of the system. The root-locus-based method is an option to determine the controller gains by fixing the closed-loop poles [88]–[90]. However, the criteria to determine the location or boundaries of the poles are not thoroughly reported.

Determining the controller gains based on crossover frequency and phase margin is another common approach [2], [91]. Nevertheless, how to determine phase margin and crossover frequency is not discussed in detail. It is suggested to keep the crossover frequency a decade below the switching frequency in [92]. In [2], the crossover frequency is fixed at the mathematical higher bound under a fixed phase margin, and a phase margin of 40 degree is suggested. While in [93], a phase margin between 30 and 60 degree with a gain margin above 6 dB is seen to be proper. In general, different criteria have been applied

for specifying the phase margin and crossover frequency of the inner current loop controller of power converters.

In high power applications, the control bandwidth of the power converter can be significantly reduced due to the reduced switching frequency [94]. As a result, an optimized tuning becomes more favored. Moreover, the effect of the grid connection filter is not negligible in the design of controllers. However, it can lead to a considerable complex system [95], [96]. Even if simplified modeling of the filter is found in existing control tuning techniques [78], [97], [98], the boundaries of the approximation needs to be justified, hence it cannot serve as a generalized method.

This section proposes a unified current loop tuning approach for grid connected power converters. The calculating algorithm based on crossover frequency and phase margin is used. Different from the existing studies, the determination of crossover frequency and phase margin is analyzed in detail to optimize the tuning. Instead of applying the phase margin and crossover frequency by classical experience, the controller gains can be tuned with more consideration of the actual system in each application. The relationship among controller gains, phase margin and crossover frequency are given in discrete-time domain for easy digital implementation and simple calculation. Besides, for an accurate estimation of the characteristics of the system, the open-loop transfer function is fully considered without the approximation of the transfer function of the controller or grid filter.

3.2.1 Modeling of the current loop

In this PhD dissertation the stationary reference frame control paradigm is employed, and the current flowing through the grid side inductor is adopted as the feedback variable.

The power converter current control loop is modeled as Fig. 3.16 shows.

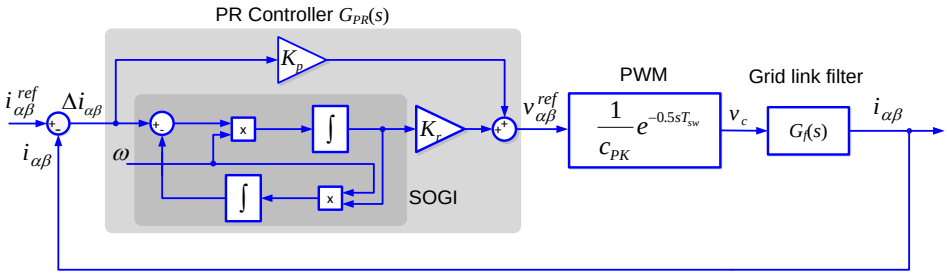

Fig. 3.16. Modeling of the current control loop.

The PR controller consists of a SOGI with a resonant gain K_r, and a proportional gain K_p. T_{sw} denotes the switching period, and due to the actual digital implementation, the computational delay is modeled to be half switching period. The gain of the PWM block is $1/c_{PK}$, where c_{PK} is the peak-to-peak value of the PWM triangular waveforms [91]. $G_f(s)$ is the transfer function between the converter output voltage and the controlled current, expressed by:

$$G_f(s) = \frac{i}{v_c}(s), \tag{3.18}$$

It has to be mentioned that the tuning procedure introduced as follow is also applicable to power converters when the synchronous reference frame current control is adopted, where it only needs to replace the PR controller block with the PI controller in the modeling.

3.2.2 A unified tuning approach

A unified current loop tuning procedure is proposed based on the previous modeling, and the stability and dynamic performance are analyzed based on numerical models.

A. Direct discrete-time domain design

Continuous-time tuning tends to work properly in digital implementations once the sampling rate is well above the controller bandwidth [94]. To overcome the limitations in digital implementation imposed by continuous-time tuning methods, in this chapter the control loop is modeled and tuned in discrete-time domain.

The transfer function of the PR controller in continuous-time domain $G_{PR}(s)$ is shown as:

$$G_{PR}(s) = K_P + K_R \cdot \mathrm{SOGI}(s), \tag{3.19}$$

where the transfer function of the SOGI is:

$$\mathrm{SOGI}(s) = \frac{\omega_0 s}{s^2 + \omega_0^2} \cdot \tag{3.20}$$

The methods for discretizing the SOGI structure have been discussed in [99]–[101]. As proposed in [101], the two integrators of the SOGI can be discretized separately. Employing the backward Euler method to discretize the integrator in the direct channel and the forward Euler method for the integrator in the feedback channel, the transfer function of the SOGI is discretized in the sampling period T_s and shown as:

$$\mathrm{SOGI}(z) = \frac{\omega_0 T_s z(z-1)}{(z-1)^2 + \omega_0^2 T_s^2 z} \cdot \tag{3.21}$$

The transfer function of the plant $G_2(s)$ is discretized by the Zero Order Hold (ZOH) method. Since all the values of the filter components are known, the discretization can be simply done employing a computing language application.

The open-loop transfer function in discrete-time domain $G_{OL}(z)$ is then expressed as:

$$G_{OL}(z) = \frac{1}{c_{PK}} G_{PR}(z) \cdot G_f(z), \tag{3.22}$$

where $G_f(z)$ is the transfer function of the filter in discrete-time domain. Since the ZOH-transformation intrinsically introduces a delay corresponding to the PWM computational delay [2], the PWM delay is hence included in the open-loop transfer function.

B. Calculation of the controller gains

The calculating algorithm based on phase margin and crossover frequency is used. According to the definitions, at crossover frequency ω_c, the module of the open-loop transfer function is equal to 1, and the phase-angle is $-(180^o - phm)$, where *phm* is the phase margin. In continuous-time domain, this relationship is shown as:

$$\left|G_{OL}(j\omega_c)\right| = 1, \tag{3.23a}$$

$$\angle G_{OL}(j\omega_c) = -(180^o - phm). \tag{3.23b}$$

Examples on calculating the controller gains in continuous-time domain with crossover frequency and phase margin can be found in [2], [91]. In this PhD dissertation, this calculation is done in discrete-time domain.

In discrete-time domain, the definitions of phase margin and crossover frequency are shown as:

$$G_{OL}(e^{j\omega_c T_s}) = 1\angle -(180^o - phm). \tag{3.24}$$

Combining (3.22) and (3.24) and assuming $c_{PK} = 1$, the below relationship is obtained and shown as:

$$G_{PR}(e^{j\omega_c T_s}) \cdot G_f(e^{j\omega_c T_s}) = 1\angle -(180^o - phm). \tag{3.25}$$

Therefore, the controller gains can be calculated once ω_c and *phm* are fixed. In practice, the complex number equation (3.25) needs to be transformed into two real number equations by extracting the real part and imaginary part respectively, that is:

$$\mathrm{Re}[G_{PR}(e^{j\omega_c T_s}) \cdot G_f(e^{j\omega_c T_s})] = \mathrm{Re}[1\angle -(180^o - phm)], \tag{3.26a}$$

$$\mathrm{Im}[G_{PR}(e^{j\omega_c T_s}) \cdot G_f(e^{j\omega_c T_s})] = \mathrm{Im}[1\angle -(180^o - phm)]. \tag{3.26b}$$

If z_c is defined to be the value of z when ω is fixed to ω_c, then (3.26) is transformed into:

$$[K_P \; K_R] \cdot \begin{bmatrix} 1 & 0 \\ \mathrm{Re(SOGI(z_c))} & \mathrm{Im(SOGI(z_c))} \end{bmatrix} = [\mathrm{Re(a)} \; \mathrm{Im(a)}], \tag{3.27}$$

where the constant *a* is written as:

$$a = \frac{1\angle -(180° - phm)}{G_f(e^{j\omega_c T_s})}. \tag{3.28}$$

C. Tuning of the controller

The controller gains K_p and K_r can be calculated by solving (3.27), which acts as a calculator, however, giving appropriate inputs for ω_c and *phm* requires further analysis.

For a second-order closed-loop system, the gains can be determined by specifying the damping coefficient and the step response settling time as shown in [101]. However, for a high order system, the relationship between the dynamics and the controller gains is more complex. A usual approach is to make reasonable specification or approximation for the open-loop transfer function [2], [91], or particularly, for the model of the grid-connection filter [78], [97], [98] to simplify the issue. In the meantime, justifications of the specification or approximation have to be given as well as the boundaries of application. In order to provide a generic tuning procedure, the closed-loop systems defined by different sets of controller gains can be evaluated and compared with each other analytically in terms of stability and dynamics.

In this section the tuning procedure for obtaining a set of optimized controller gains is introduced through a practical tuning case. The procedures of the tuning are summarized in Fig. 3.17.

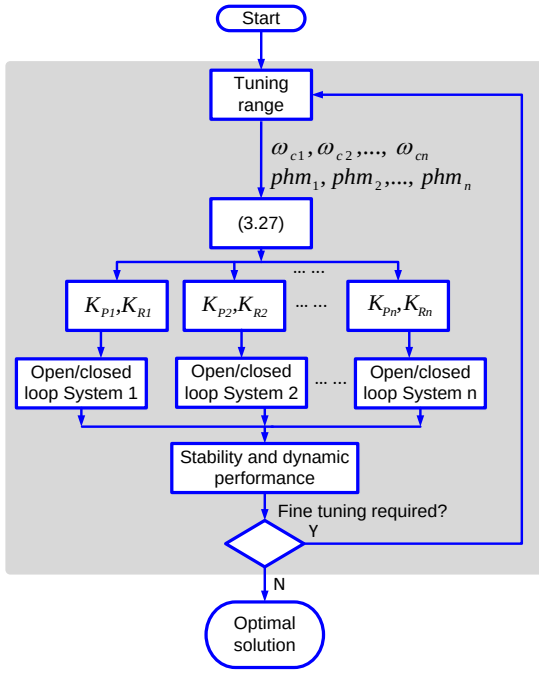

Fig. 3.17. Executing flow chart of the proposed tuning procedure.

In the first step, ω_c and *phm* are respectively specified with different values within the initial tuning range, and for each set of ω_c and *phm*, a set of K_p and K_r will be obtained

through (3.27). Commonly, the phase margin reflects the stability, and the crossover frequency reflects the bandwidth. So it is easy to designate an initial tuning range in advance. Then different sets of controller gains will be obtained, and each set will lead to an open-loop and a closed-loop system. By the assessment on open-loop stability margin, closed-loop system transient response and closed-loop band width, each solution is evaluated and a refined tuning range is found.

Even though the phase margin has already been specified in advance for calculating the controller gains, it has to be checked again after the system is specified. As mentioned in [98], in some scenarios when the PR controller is assigned to track harmonics, additional open-loop resonant poles will occur, resulting in the practical phase margin to be lower than the specification.

When the refined tuning range is found, another tuning is executed in a reduced range found in the first step, but with a smaller interval of the inputs. In this manner, progressive tuning is executed until an optimized solution is found.

A 100 kW two-level three-phase grid connected power converter, with practical parameters as shown in Table A.2 in Appendix A.1, is used to illustrate the tuning method. The grid link filter for this system is an LCL-trap filter [95], [96], which is described in the Appendix A.2.

The control requirements in this case are shown in Table 3.3, where settling time and overshoot are the ones calculated from the closed-loop system transient response, which is written as (3.15). The settling time is calculated by (3.16), and the overshoot is calculated by:

$$P_{os} = \max\left[\frac{P(t)}{P_{ss}} - 1\right]. \tag{3.29}$$

Table 3.3 Tuning limits for the current controller

Parameter	Limit
Settling time	<25 [ms]
Overshoot	<15 [%]
Gain margin	>5 [dB]
Phase margin	>35 [º]

Fig. 3.18 is plotted by specifying different values to ω_c and *phm* in a large range, and for each obtained solution of K_p and K_r, the open-loop stability margin, settling time t_{ss} and overshoot of the closed-loop unitary step response, and closed-loop band width are calculated. Fig. 3.18(a) and Fig. 3.18(b) show the influence of ω_c and *phm* on the performance of the system, respectively.

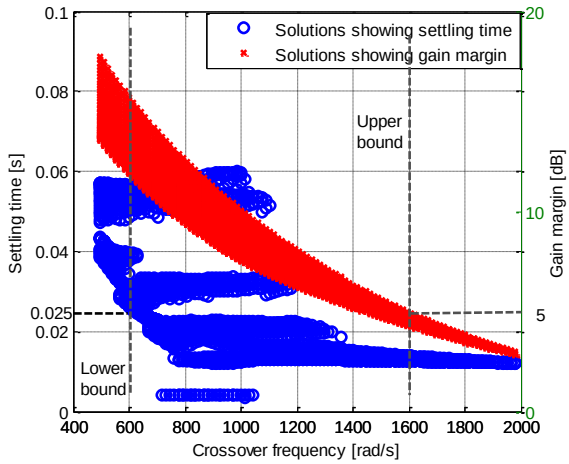

(a)

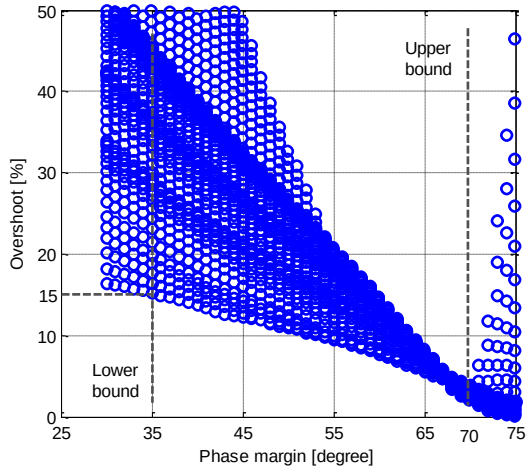

(b)

Fig. 3.18. Influence of ω_c and *phm* on the performance of the system: (a) influence of ω_c on t_{ss} and gain margin, and (b) influence of *phm* on overshoot.

In Fig. 3.18(a), the influence of the crossover frequency on the settling time t_{ss} and the gain margin are both shown. When ω_c increases from 500 to 800 rad/s, t_{ss} has a general trend of reducing, while gain margin has a general trend of reducing in the full range of ω_c. Fig. 3.18(a) also visualizes the trade-off between system stability and dynamics, and shows that a ω_c too great or small should both be avoided. When ω_c is above 1600 rad/s, the gain margin is smaller than 5 dB. In order to ensure the stability of the system, solutions with gain margin smaller than 5 dB are not accepted in the tuning. Therefore, the upper bound of ω_c is chosen to be 1600 rad/s. And when ω_c is below 600 rad/s, t_{ss} is greater than 25 ms. In order to ensure the speed of response, solutions with t_{ss} greater than 25 ms are not accepted in the tuning. So the lower bound ω_c is chosen to be 600 rad/s. Therefore, the refined input range of ω_c is obtained and shown as:

$$\omega_c = \{600, 600 + d\omega, 600 + 2d\omega, \cdots, 1600\} \quad (rad/s), \tag{3.30}$$

where $d\omega$ is the input interval that is chosen to be 10 rad/s.

Fig. 3.18(b) shows the relationship between overshoot and *phm*. When *phm* increases, the overshoot generally reduces. When *phm* is smaller than 35°, no solution has an overshoot below 15%. Since responses with large overshoot could render the converters to be oversized, the lower bound of *phm* is chosen to be 35°. Besides, the upper bound is chosen to be 70°. The refined tuning range of *phm* is obtained and shown as:

$$phm = \{35^\circ, 36^\circ, 37^\circ, \cdots, 70^\circ\}. \tag{3.31}$$

Even though some solutions that do not meet the tuning requirements have been rejected once the refined tuning range is obtained, the tuning limits are still necessary in the further tuning process to eliminate all the undesired solutions. With the inputs shown in (3.30) and (3.31), different sets of K_p and K_r are obtained. All the solutions that leads to a performance within the limits shown in Table 3.3 will be identified as eligible and stored, and one optimal solution can further be selected.

To select the optimal solution, different criteria can be used to rank the solutions and to select the desired one. It is indicated in [2] that the bandwidth should be selected as high as possible to achieve the best dynamics. Fig. 3.19 shows the bandwidth of the closed-loop systems related to ω_c and *phm* based on the eligible solutions. In this tuning case, the solution with the largest bandwidth is selected as the optimal one, which is shown in Table 3.4. It is seen in the figure that the eligible solutions mostly gather in the range of ω_c = [900 rad/s, 1100 rad/s] and *phm* = [55°, 70°]. Optionally, the number of the eligible solutions can be increased simply by reducing the input interval $d\omega$.

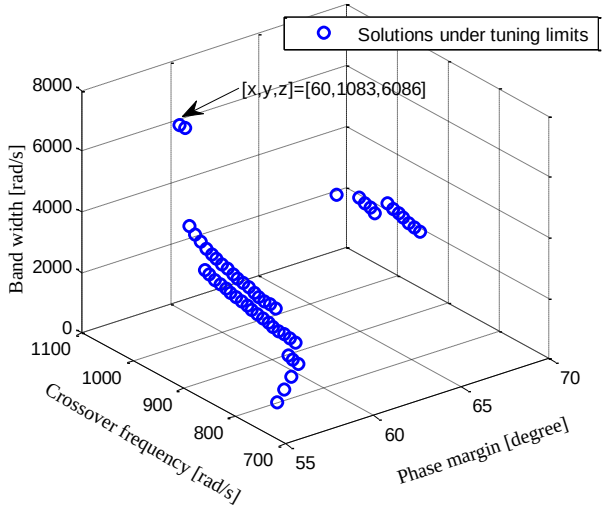

Fig. 3.19. Solutions that comply with the tuning limits.

Table 3.4 Selected solution of the controller gains

Parameter	Value
K_p	1.2192
K_r	0.5593
Settling time	22.5 [ms]
Overshoot	14.66 [%]
Gain margin	7.1276 [dB]
Phase margin	60 [º]
Band width	6086 [rad/s]
Cross-over frequency	1083 [rad/s]

Based on the selected optimal solution, the Bode plot of the open-loop system is shown in Fig. 3.20, where the stability is validated. By applying the above tuning procedure, the input of phase margin and crossover frequency can be determined reasonably according to the desired stability and dynamics limits. Therefore, instead of always using the phase margin and crossover frequency by classical experience, the controller gains can be tuned with more consideration of the actual system in each application.

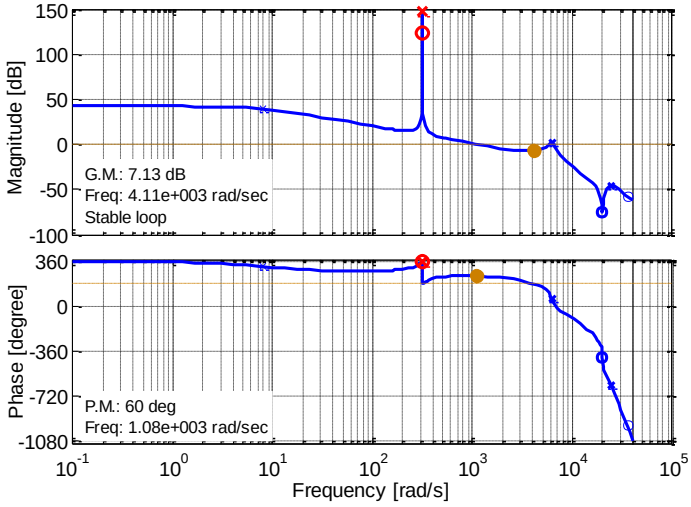

Fig. 3.20. Bode diagram of the open-loop system under the chosen gains.

3.2.3 Test results of current controller

A. Simulation Results

In this section, the current loop tuning method is primarily validated in two simulated grid connected power converters with 10 kW and 100 kW power rating, respectively. The test setup and control strategy are shown in Fig. 3.21, where a simple control scheme is used to check the dynamics of the current loop.

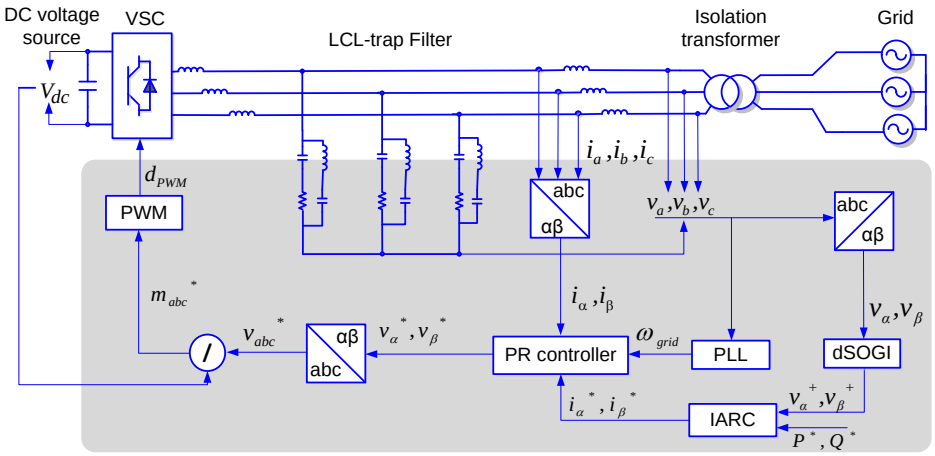

Fig. 3.21. PLL-based current control scheme.

With a synchronization algorithm, namely stationary frame PLL [102], the frequency of the grid ω_{grid} is estimated based on the measurement of three-phase grid voltage. The reference of the current controller i_α^* and i_β^* are provided according to the instantaneous active reactive controller (IARC) [103] shown as:

$$i_\alpha^* = \frac{P^* v_\alpha^+ + Q^* v_\beta^+}{v_\alpha^{+2} + v_\beta^{+2}}, \tag{3.32a}$$

$$i_\beta^* = \frac{P^* v_\beta^+ - Q^* v_\alpha^+}{v_\alpha^{+2} + v_\beta^{+2}}, \tag{3.32b}$$

where P^* and Q^* are respectively the reference of active power and reactive power, and v_α^+ and v_β^+ the positive sequence components of grid voltage in stationary frame extracted by D-SOGI [69].

The key parameters of the 10 kW and 100 kW simulation test systems are shown in Table 3.5 and Table 3.6, respectively. This simulation test system is presented in detail in the Appendix A.1.

Table 3.5 Key parameters of the 10 kW power converter and controller gains

Description	Symbol	Value
grid phase-phase voltage	V_{line}	400 [V]
grid frequency	f_g	50 [Hz]
dc bus voltage	V_{dc}	640 [V]
converter nominal power	P_N	10 [kW]
switching frequency	f_{sw}	10050 [Hz]
samping frequency	f_s	10050 [Hz]
current controller proportional gain	K_p	8.7818
current controller resonant gain	K_r	7.7968

Table 3.6 Key parameters of the 100 kW power converter and controller gains

Description	Symbol	Value
grid phase-phase voltage	V_{line}	400 [V]
grid frequency	f_g	50 [Hz]
dc bus voltage	V_{dc}	750 [V]
converter nominal power	P_N	100 [kW]
switching frequency	f_{sw}	3150 [Hz]
samping frequency	f_s	6300 [Hz]
current controller proportional gain	K_p	1.2192
current controller resonant gain	K_r	0.5593

The simulation results of the 10 kW system are shown in Fig. 3.22, where the steady state and dynamic performance are shown. A power reference of 5 kW and 0 kvar is given initially, and it changes to 10 kW and 0 kvar at t=0.01s. Fig. 3.22(a) shows the three-phase current waveforms, and how it is regulated properly in both steady state and transient without oscillations. Fig. 3.22(b) shows the instantaneous power injection to the grid by the converter. If 5% of the nominal power is defined as the steady state band, then the active power regulation settling time is calculated to be 1.8 ms. Fig. 3.22(c) shows the current control errors on the α and β axes. If 10% of the magnitude of the nominal current is defined as the steady state band, then the settling time of the current controller on the α and β axes are 0.9 ms and 0.6 ms, respectively. Therefore, a fast response of the current loop is demonstrated.

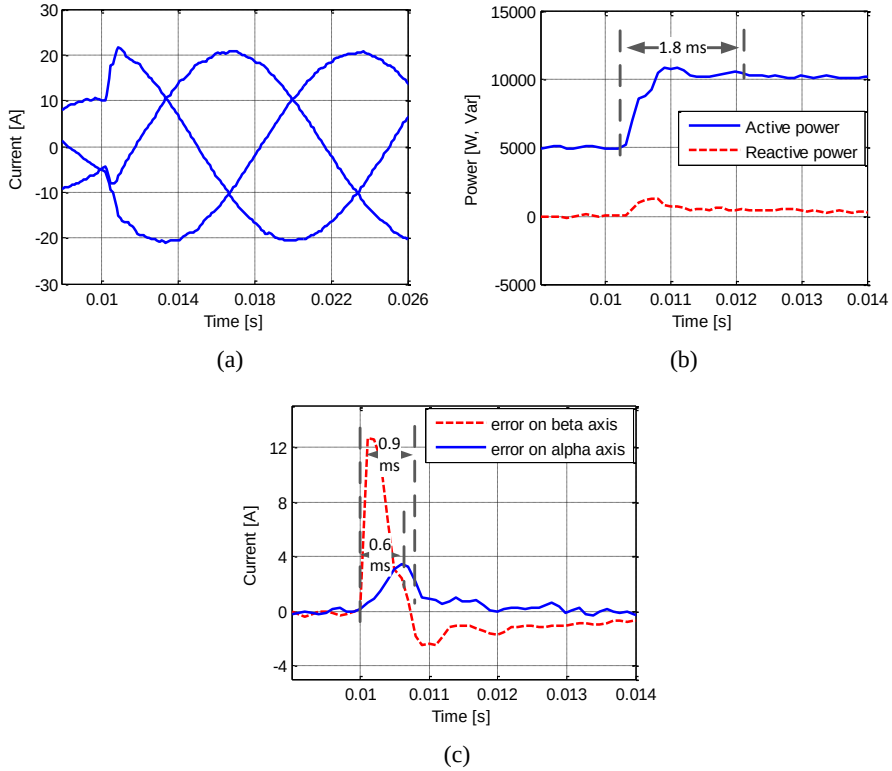

Fig. 3.22. Simulated performance of the 10 kW system when active power reference jumps from 5 kW to 10 kW: (a) grid injected current, (b) instantaneous active and reactive power injection, (c) current control error on α and β axes.

The simulation results of the 100 kW system are shown in Fig. 3.23, where a step in the active power reference from 50 kW to 100 kW is given at t=0.01s.

Fig. 3.23(a) shows the three-phase current waveforms. As well as the case of the 10 kW system, the grid injected current is regulated properly in steady state and presents a fast transient response. Fig. 3.23(b) shows the instantaneous power injection. If 5% of the nominal power is defined as the steady state band, then the active power regulation settling time is calculated to be 3.0 ms. Fig. 3.23(c) shows the current control errors on the α and β axes. If 10% of the magnitude of the nominal current is defined as the steady state band, then the settling time of the current controller on the α and β axes are respectively 3.2 ms and 1.7 ms.

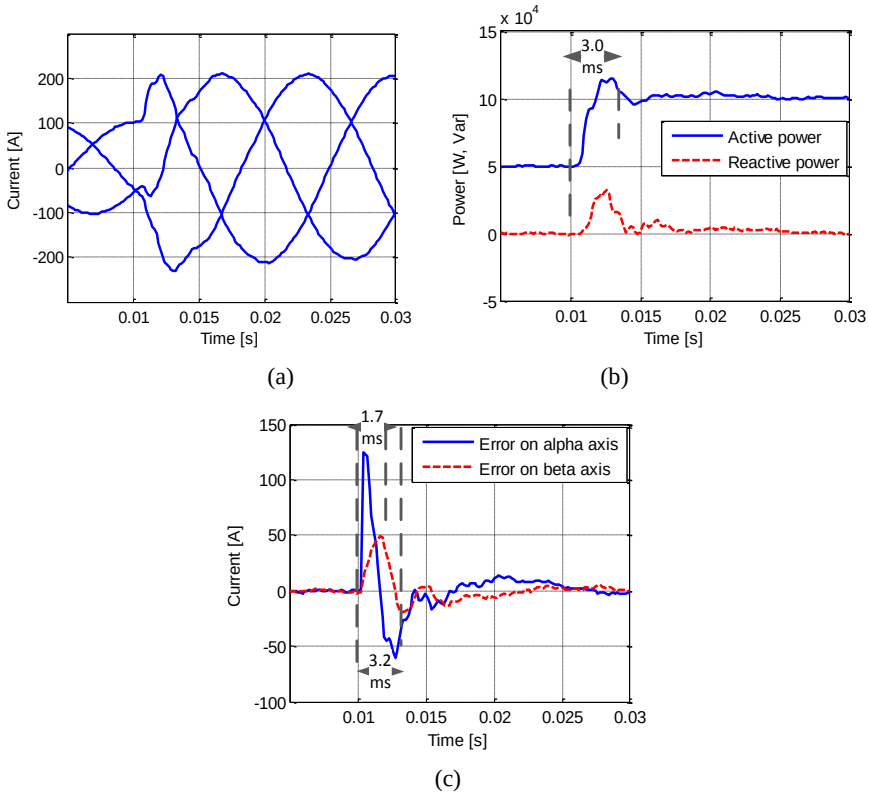

Fig. 3.23. Simulated performance of the 100 kW system when active power reference jumps from 50 kW to 100 kW: (a) grid injected current, (b) instantaneous active and reactive power injection, (c) current control error on α and β axes.

B. Experimental Results

Experimental tests are conducted in order to further validate the proposed tuning method. The 10 kW experimental setup and parameters are the same as the ones in simulation shown in Fig. 3.21 and Table 3.5. The dc bus of the converter is supplied by a dc power source, and the ac grid is formed by a regenerative power source of which the voltage magnitude and frequency can be programmed. This 10 kW grid connected power converter experimental setup is presented in Appendix B.1 in detail.

Firstly the control scheme of Fig. 3.21 is implemented to check the performance of the current loop independently. The current loop static and transient performance based on the 10 kW system are shown in Fig. 3.24.

Fig. 3.24(a) shows the grid voltage and injected current, where the current is well regulated as in simulation. Fig. 3.24(b) shows the instantaneous active and reactive powers injected into the grid. With the same definition of the steady state band as the simulation, the settling time of the active power is calculated to be 2.0 ms. The current control error on the α and β axes are shown in Fig. 3.24(c). With the same definition of the steady state band as in the simulation, the settling time of the error on α and β axes are 0.7 ms, 2.8 ms. Table 3.7 shows

that the experimental results are close to the simulation results with respect to the active power settling time.

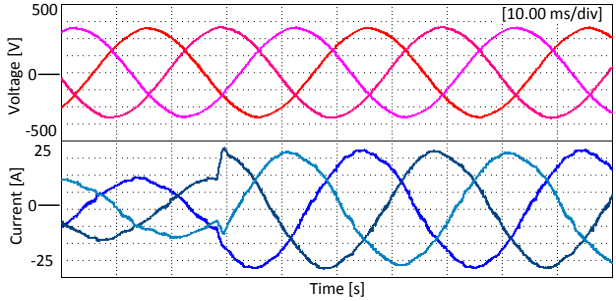

(a)

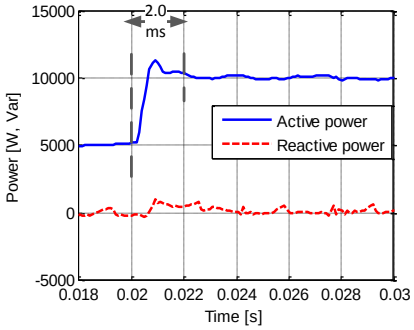

(b)

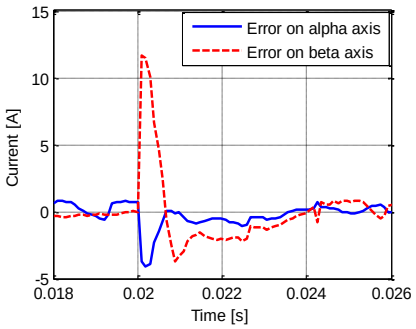

(c)

Fig. 3.24. Experimental performance of the 10 kW system when active power reference jumps from 5 kW to 10 kW: (a) grid voltage and injected current, (b) instantaneous active and reactive power injection, (c) current control error on α and β axes.

Table 3.7 Comparison of the settling time in simulations and experiments

Settling Time	Simulation	Experiment
active power	1.8	2.0
α-axis current	0.9	0.7
β-axis current	0.6	2.8

There is not any theoretical difference between the dynamics of the α-current controller and β-current controller. However, because of the different profiles of the time response of the α and β controller, the calculated settling time will always be different. The fact is that in any specific moment during the transient, the deviation (relative to zero) of the current control error on α and β axes are different. So it will be easy to explain the difference of the settling time calculation by (3.16). The steady-state band for settling time calculation of the current control error is defined to be 10% in the tests, since that the measured static current

control error in experiments varies in a range greater than ±5% of the nominal current.

Response of the power converter in front of a three-phase voltage sag is also tested. As shown in Fig. 3.25(a), the grid voltage experiences a sag that lasts for 1 s, and the phase-to-neutral voltage rms is reduced from 230 V to 150 V. During the sag, the converter remains connected to the grid, and the injected current keeps stable, without significant oscillations except for a minor transient. The active and reactive powers are accurately controlled as shown in Fig. 3.25(b).

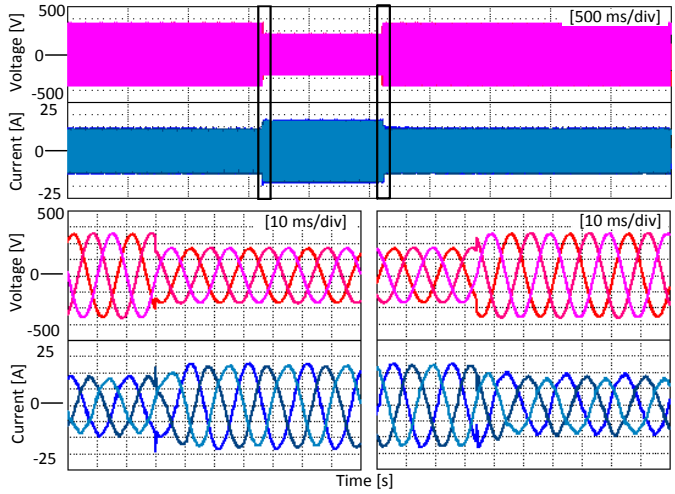

(a)

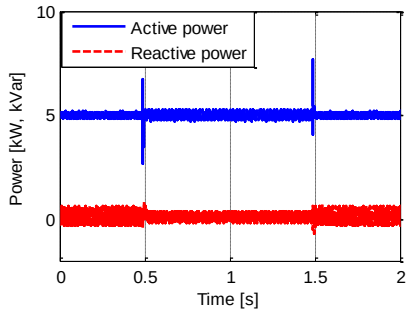

(b)

Fig. 3.25. Experimental results of the current controller under three-phase grid voltage sag: (a) grid voltage and injected current waveforms, and (b) active and reactive powers injected into the grid.

In the following, the current controller is integrated in the overall SPC control scheme shown in Fig. 2.1 in Chapter 2 to validate the performance of the current controller under grid frequency changes. A grid frequency variation is generated by configuring the regenerative ac power source, as shown in Fig. 3.26(b), where the frequency changing slope is 1 Hz/s.

Fig. 3.26(a) shows the response of the current injected by the power converter during frequency changes. It increases its magnitude when the frequency decreases, and vice versa,

thanks to the effect of the virtual inertia provided by the SPC. Particularly, the performance of the current controller when tracking a given reference current is shown in Fig. 3.26(c), where it can be observed how the regulated current perfectly tracks its reference at any time.

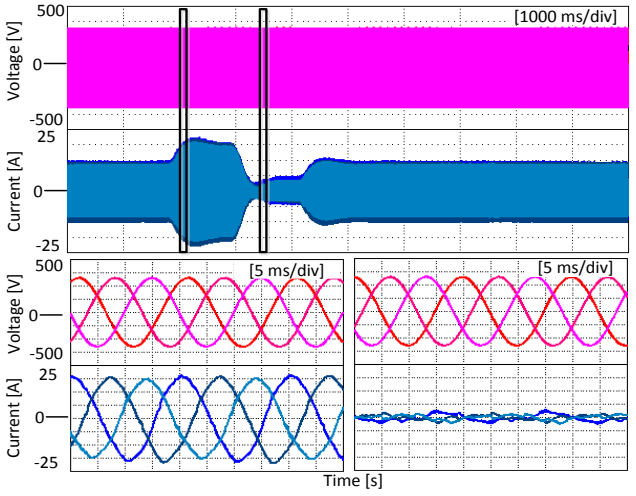

(a)

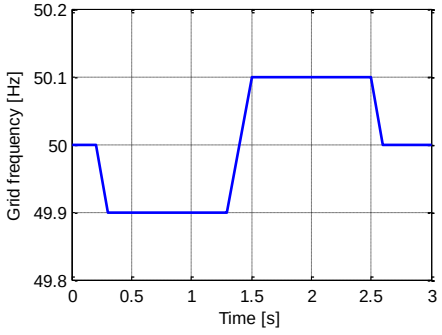

(b)

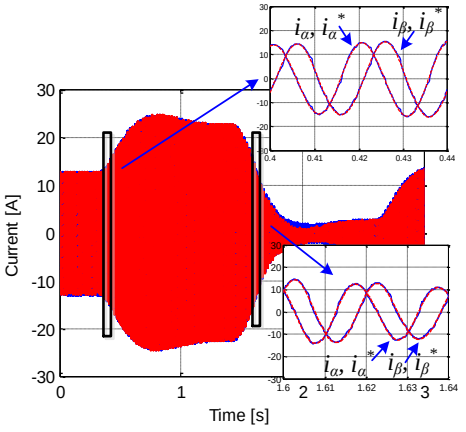

(c)

Fig. 3.26. Experimental results of the current controller (integrated in the SPC) under grid frequency variations: (a) grid voltage and injected current, (b) the variation of grid frequency imposed by the ac regenerative power source, (c) current reference and measurement on α and β axes.

3.3 Summary of the Chapter

In this chapter, a virtual admittance control structure oriented to the support of grid voltage during asymmetrical grid faults was presented. Such control structure is based on the general control framework of the SPC for grid connected power converters. By using several parallel admittance branches for positive- and negative-sequence current injection,

the unbalanced voltage at the PCC during asymmetrical faults can be considerably compensated. Simulation and experimental results based on paralleled 100 kW power converters showed the significant effect of negative-sequence current injection in compensating unbalanced grid voltage. A desired proportional gain in positive- and negative-sequence current injection for meeting the grid codes can be easily achieved by adjusting the values of the positive- and negative-sequence admittances, respectively. The time response of the power converter in presence of asymmetrical grid faults can be also adjusted to yield a fast voltage support. Moreover, the transient admittance makes the power converter contributes to improve the response speed when asymmetrical faults takes place.

A unified current loop tuning procedure was also presented in this chapter as a general approach for the control design of grid connected power converters. An analysis-based manner was used to determine the open-loop system crossover frequency and phase margin, instead of the experience-based manners that are found in most of the existing studies on this regard. A direct discrete-time domain tuning was used based on the discretized modeling of the system, which guarantees the effectiveness of the controller in digital implementation. Finally the tuning results were validated by simulation and experiments in different scenarios, where the current loop presented a fast transient response and good steady-state performance in power reference tracking, as well as in grid frequency and voltage support. With a good foundation in the current control loop, the power converter exhibited excellent grid-supporting characteristics when the outer loops of the SPC were activated.

CHAPTER
4.

The Power Loop Controller

In this chapter, a power loop controller for the Synchronous Power Controller (SPC) is presented, which provides inertia, damping and flexible droop characteristics. Different from the faithful replication of the swing equation of synchronous machines, an alternative control structure is presented, by which the inertia, the damping and the inherent P-f droop gain can be configured independently to meet the requirements in both dynamics and frequency regulations.

The good performance of the power loop controllers presented in this PhD dissertation to provide inertia and droop characteristics, as well as controllable transient response, was demonstrated by simulation and experimental tests on a regenerative power source test bed. The power loop controllers presented in this chapter enables the SPC-based grid connected power converter to provide frequency support accurately, following a specified dynamics, thus ensuring a good interaction between the power converter and the electrical grid.

4.1 Introduction

The active power exchanged between a synchronous generator and the grid can be modeled by (2.3). Then the active power control loop can be modeled as Fig. 2.3 shows in Chapter 2. For modeling and analyzing the active power control loop, V can be set at its nominal value and E can be estimated to be approximately equal to V, considering the synchronous converter operation point close to its rated values.

A VSC based on a virtual admittance can be simply modeled as an admittance gain because of two facts: (a) the power is delivered based on the load-angle and reactance as shown in (2.3), and (b) the inner current controller is significantly faster than the power loop controller, and hence its dynamics can be decoupled from the modeling of the power control loop to reduce complexity in the analysis.

The design of the power loop controller for virtual synchronous generator is discussed in this chapter based on the above modeling of the active power control loop. The mainstream technique for implementing the power loop controller is the emulation of the synchronous machine swing equation, as is presented in [25] and many other publications. This strategy is analyzed first in this chapter, and its inherent *P-f* droop characteristic is discussed. Based

on the swing equation emulation, the damping effect of the power loop controller and the *P-f* droop gain are constrained by each other. Setting a good value for the droop gain may lead to an insufficient damping in the power loop controller, and in the other way around, a proper damping value might give rise to an undesired inherent droop gain. In [33], it is proposed to use an additional PI controller, with a virtual switch, to adjust the power loop damping parameter to achieve a precise power tracking when needed. This solution however increases the order of the closed-loop transfer function, and thus the dynamic analysis and tuning of controller parameters become more complex.

This chapter presents an alternative power loop controller structure, which allows the inherent *P-f* droop characteristic gain to be configurable, and thus the active power control and *P-f* droop control can be integrated in a simple implementation. As design considerations for this power loop controller, the virtual angle stability and transient response are both analyzed, and a detailed implementation structure, which does not entail any difficulty from a practical point of view, is presented. Besides, the mathematical relationship between the power loop controller performance specifications and the control parameters is also illustrated.

The PI-based power loop controller is also introduced in this chapter, which is another alternative to the power controllers reported in the literature and shows zero steady-state error in power control in case of grid frequency changes.

4.2 Emulation of the Swing Equation

The synchronous machine swing equation for small signal variation of the rotor angular frequency, ω, around the rated rotor angular frequency, ω_s, can be expressed as (2.5). The damper winding of synchronous machines provides some damping, but it is relatively limited. Therefore, the damping provided by grid connected power converters implementing a virtual electromechanical control loop, which is not restricted by mechanical constrains, can be more effective than the one provided by conventional electromechanical generators.

Based on the swing equation, the power loop controller in Fig. 2.3, $G_{PLC}(s)$, could be implemented as shown in (4.1), considering both the inertia, J, and the damping, D, terms. This transfer function is referred as the Mechanical Power Loop (MPL) controller in this chapter.

$$G_{PLC}(s)=\frac{1}{\omega_s(Js+D)} \tag{4.1}$$

According to (4.1), the resulting second-order closed-loop transfer function would have the following form:

$$\frac{P}{P^*}(s)=\frac{\omega_n^2}{s^2+2\xi\omega_n s+\omega_n^2}, \tag{4.2}$$

where:

$$\xi = \frac{D}{2}\sqrt{\frac{\omega_s}{JP_{\max}}}, \tag{4.3a}$$

$$\omega_n = \sqrt{\frac{P_{\max}}{J\omega_s}}, \tag{4.3b}$$

being $P_{\max} = \dfrac{EV}{X}$ as defined in (2.3) in Chapter 2.

Instead of using the moment of inertia J to specify the inertial characteristics, the inertia constant H is commonly used in the literature, which is defined in (4.4). This constant represents the time a mass moment of inertia J takes to accelerate the rotational speed from zero to ω_s by spending a power S_N [104].

$$H = \frac{J\omega_s^2}{2S_N} \tag{4.4}$$

Therefore, the MPL controller gains, J and D, should be set according to:

$$J = \frac{2HS_N}{\omega_s^2}, \tag{4.5a}$$

$$D = \frac{2\xi}{\omega_s}\sqrt{\frac{2HS_N P_{\max}}{\omega_s}}\ . \tag{4.5b}$$

For analyzing the power control loop dynamics, its response to frequency disturbances should be also studied. In modeling, the grid frequency can be linked to the grid phase-angle by an integrator, as shown in Fig. 4.1.

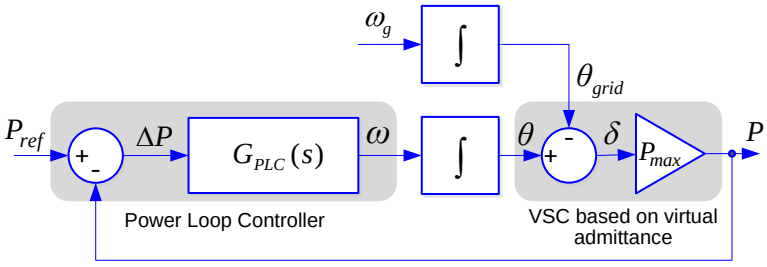

Fig. 4.1. Modeling of the SPC's active power control considering grid frequency changes.

Taking the grid frequency, ω_g, as an input variable and P as the function output, the associated transfer function (P-f response) can be shown as:

$$\frac{P}{\omega_g}(s)=\frac{-P_{\max}(s+2\xi\omega_n)}{s^2+2\xi\omega_n s+\omega_n^2}, \tag{4.6}$$

where ω_n and ξ are given by (4.3a) and (4.3b), respectively.

By observing (4.6), it can be concluded that the MPL controller incorporates an intrinsic *P-f* droop characteristic. Therefore, an inherent droop ratio D_P can be defined as:

$$D_P=(\frac{2\pi}{1000})\cdot\left|\frac{P}{\omega_g}(s)\right|_{s=0}\quad [\text{kW/Hz}], \tag{4.7}$$

which describes the steady-state power variation delivered by the power converter in response to a grid frequency change. Therefore, by combining (4.6) and (4.7), the inherent droop ratio of the MPL controller $D_{P(MPL)}$ can be expressed as:

$$D_{P(MPL)}=\frac{4\pi\xi P_{\max}}{1000\omega_n}. \tag{4.8}$$

As (4.8) shows, the droop ratio D_P is constrained by the inertia and damping parameters. If the per-unit gain of the *P-f* droop is named as R_D, which represents the grid frequency deviation that extracts the full rated power from the converter [105], the relationship between D_P and R_D would be given by:

$$R_D=\frac{2\pi S_N}{1000D_P\omega_s}, \tag{4.9}$$

where S_N is the rated power of the generation unit.

Then, the interaction among the inertia, the damping and the *P-f* droop gain defined by the MPL controller can be written as:

$$R_{D(MPL)}=\frac{1}{2\xi}\sqrt{\frac{X_{pu}}{2H\omega_s}}, \tag{4.10}$$

which is obtained by substituting the D_P in (4.9) using (4.8), and further substituting the ω_n and J using (4.3b) and (4.5a), respectively. In (4.10), X_{pu} represents the per-unit value of the reactance of the virtual admittance, whose base value, X_b, is defined as:

$$X_b=\frac{V^2}{S_N}, \tag{4.11}$$

then X_{pu} is expressed by:

$$X_{pu}=\frac{X}{X_b}=\frac{X}{V^2/S_N}=\frac{S_N}{P_{max}}. \tag{4.12}$$

Since the values of H and X_{pu} can be preset according to design requirements, the controller tuning task mainly lies in the restriction between ξ and R_D, as (4.10) shows. As inertia and damping take finite values, R_D will take a finite value as well, instead of being zero. It means, the power loop presents an intrinsic droop characteristic. Thus, the value of the active power generated by the power converter in steady-state will not be only given by the active power reference, but it will be also determined by the grid frequency. Then, an external droop controller is needed to compensate the effect of this intrinsic droop gain if precise power reference tracking is needed, or if a given droop characteristic should be provided by the power converter.

The constraint between the inherent droop and the damping is visualized in Fig. 4.2, where (4.10) is represented considering, $\omega_s = 2\pi 50$ rad/s, $X_{pu} = 0.3$, and $H = \{0.3, 0.6, 5, 20\}$.

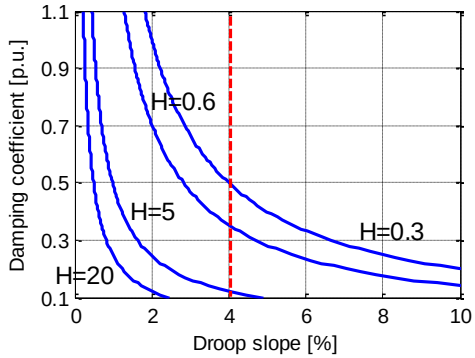

Fig. 4.2. The relationship between the inherent *P-f* droop gain, R_D, and the damping coefficient, ξ.

As shown in Fig. 4.2, once the droop gain is set, the damping coefficient will be set as well. However, the droop gain needs to be set considering the grid operator requirements and the power reserve of the generation plant. For traditional synchronous machines, 4% is a typical value for the droop gain [105]. In the scenarios shown in Fig. 4.2, if R_D is set to 4%, ξ will be smaller than 0.5 for any value of H plotted in Fig. 4.2, which may lead to an insufficient damping. Further, if R_D was required to have a high value, ξ would have to take a very low value, which undermines the damping performance of the system. For the second-order parametric transfer function of (4.2), the damping coefficient ξ has a theoretical optimal value of $1/\sqrt{2}$, which provides a good balance between the rising time and overshoot.

On the other hand, a normal value for ξ leads to a small value for R_D. This should not be an issue in case the grid was dominated by power converters controlled through the MPL, since a small value of R_D leads to strong effect in compensating frequency deviations. However, if the system is dominated by traditional synchronous generators, a variation in the grid frequency could originate some issues, such as insufficient energy storage and saturation, or even poor power quality in those converters with a small value for R_D. Therefore, an external *P-f* droop controller is necessary in order to modify the inherent droop gain of the power loop controller and set proper overall droop characteristic in the power converter.

4.3 Power Loop Controller with Flexible Frequency Droop

The power loop controller for the SPC (PLC in Fig. 2.1) allows multiple implementations as long as it results in a closed-loop transfer function that has similar dynamics as the electromechanical loop of a synchronous machine. This section proposes a synchronous power controller with inertia, damping and flexible droop characteristics for grid connected power converters. Compared with the swing equation emulation, damping and droop characteristics are particularly addressed, while the inertia feature is maintained. The damping performance is important for the local stability and dynamics of renewable power generation systems, and the droop characteristics are necessary to fulfil the required frequency support. Therefore, instead of tuning a single parameter to find a good tradeoff between both damping and inherent *P-f* droop gain, a controller structure is proposed to configure damping and droop characteristics separately. In addition, an explicit relationship among the controller gains, inertia, damping coefficient and droop gain is given.

4.3.1 Controller structure

In order to achieve a good grid interactive performance, in which the droop gain can be specified independently of the damping parameter, a power loop controller with inertia, damping and flexible droop characteristics is presented in Fig. 4.3.

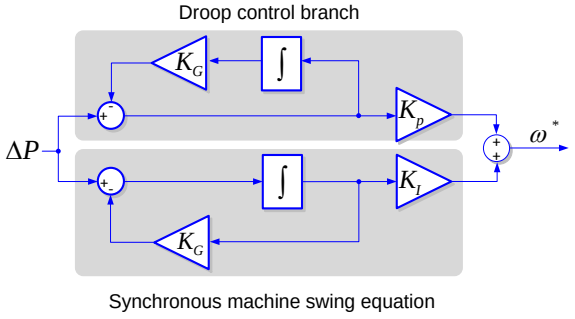

Fig. 4.3. The proposed power loop controller.

In Fig. 4.3, the direct implementation of the synchronous machine swing equation is modified by adding a droop branch in parallel for controlling the *P-f* droop gain in steady state. In this way, this branch adjusts the offset of the power transfer function by introducing a new degree of freedom. The structure of the droop branch is developed in the way that it shares the same denominator with the transfer function of the swing equation. In this manner, the order of the power regulating loop does not increase.

The transfer function of the proposed controller is generalized and written as:

$$G_{PLC}(s)=\frac{K_P s+K_I}{s+K_G}, \tag{4.13}$$

which is referred as Configurable Natural Droop (CND) controller in this PhD dissertation.

Compared with the MPL controller, the CND controller provides an additional degree of freedom without increasing the order of the power regulating transfer function. Moreover, it gives an inherent *P-f* droop feature, which can be configured independent to the inertia and damping parameters.

Substituting the power loop controller block in Fig. 4.1 by the expression (4.13), the resulting closed-loop transfer function can be written as:

$$\frac{P}{P^*}(s)=\frac{(2\xi\omega_n - K_G)s+\omega_n^{\,2}}{s^2+2\xi\omega_n s+\omega_n^{\,2}}, \tag{4.14}$$

where the damping coefficient and natural frequency are expressed as:

$$\xi = \frac{P_{\max}K_P + K_G}{2\omega_n}, \tag{4.15a}$$

$$\omega_n = \sqrt{P_{\max}K_I}\,. \tag{4.15b}$$

Therefore, the CND controller gain, K_I, should be set according to:

$$K_I = \frac{\omega_n^2}{P_{\max}}. \tag{4.16}$$

Further, the natural frequency, ω_n, can be translated to the moment of inertia, J, by equating the two ω_n in (4.3b) and (4.15b). In this manner, the CND controller with the controller gain, K_I, results in a closed-loop transfer function that presents a same value for ω_n as the one resulted from the MPL controller with the controller gain, J. Because of the same closed-loop dynamics, it is fair to say that K_I defines a moment of inertia, which has the amount of J. Therefore, (4.16) changes to:

$$K_I = \frac{1}{J\omega_s}, \tag{4.17}$$

which can be expressed in terms of H as:

$$K_I = \frac{\omega_s}{2HS_N}. \tag{4.18}$$

The *P-f* response of the CND controller is given by:

$$\frac{P}{\omega_g}(s)=\frac{-P_{\max}(s+K_G)}{s^2+2\xi\omega_n s+\omega_n^{\,2}}, \tag{4.19}$$

where (4.20) is obtained.

$$D_{P(CND)} = \frac{2\pi K_G}{1000 K_I} \tag{4.20}$$

The controller gain, K_G, should be set according to:

$$K_G = \frac{250 D_P \omega_s}{\pi H S_N}, \tag{4.21}$$

which is obtained by substituting the K_I in (4.20) using (4.18). Further, (4.21) can be changed to (4.22) expressed in terms of the per-unit droop gain, R_D.

$$K_G = \frac{1}{2HR_D} \tag{4.22}$$

Substituting the ω_n in (4.15a) using (4.15b), and further substituting the K_I using (4.18) and the K_G using (4.22), respectively, the following expression is obtained:

$$K_P = \xi \sqrt{\frac{2\omega_s}{P_{\max} H S_N}} - \frac{1}{2HR_D P_{\max}}, \tag{4.23}$$

by which the controller gain, K_P, can be set.

According to (4.18), (4.22) and (4.23), the CND controller gains, K_P, K_I and K_G, can be respectively set, according to the inputs of H, ξ and R_D. Owing to the explicit link between the controller gains and characteristic parameters, the controller can be easily made adaptive through a secondary control, and a flexible power control becomes possible. In the implementation, the algorithm for calculating the control parameters based on (4.18), (4.22) and (4.23) can be embedded in the converter controller, but will only be activated when the secondary commands are updated.

4.3.2 Local stability

As an important design consideration, the influence of the control parameters on the local stability should be analyzed. For a synchronous machine, the angle stability is mainly determined by the damping factor ξ.

Based on the proposed power loop controller, equivalence between the converter and synchronous machine is built. In traditional power systems, the small-signal rotor angle stability has to be achieved to maintain the synchronism of different machines. The instability can be the result of insufficient synchronizing torque, insufficient damping torque or unstable control actions [104]. In this chapter, the local stability of a converter is studied, which corresponds to the stability issue of insufficient damping torque of synchronous machines.

The state-space representation of the power control loop in Fig. 4.1 is:

$$\Delta\dot{\theta} = A\Delta\theta + \mathbf{B}\begin{bmatrix}\Delta P_{ref}\\ \Delta\omega_g\end{bmatrix}, \tag{4.24a}$$

$$\Delta P = C\Delta\theta + \mathbf{D}\begin{bmatrix}\Delta P_{ref}\\ \Delta\omega_g\end{bmatrix}, \tag{4.24b}$$

where $\Delta\theta$ is the state, and ΔP is the output, while ΔP_{ref} and $\Delta\omega_g$ are the inputs, and

$$A = -P_{\max} G_{PLC}(s), \tag{4.25a}$$

$$\mathbf{B} = [B_1 \quad B_2] = \left[G_{PLC}(s) \quad \frac{1}{s} P_{\max} G_{PLC}(s) \right], \tag{4.25b}$$

$$C = P_{\max}, \tag{4.25c}$$

$$\mathbf{D} = [D_1 \quad D_2] = \left[0 \quad -\frac{1}{s} P_{\max} \right]. \tag{4.25d}$$

By specifying the damping factor ξ of the characteristic equation greater than 0, the two eigenvalues of the matrix **A** will have negative real parts to make the control loop stable.

In case of a grid connected power converter controlled by the CND controller, even if the numerator of the power loop transfer function is different from the one resulting from the MPL controller, the characteristic equation remains the same. Therefore, it is reasonable to expect that the local stability is mainly influenced by the damping factor.

Fig. 4.4 validates the influence of the damping factor ξ on the power loop stability. It shows the root loci with respect to the change of ξ and H. The figure is plotted based on a 5% droop gain. The damping factor ξ has to be specified greater than 0 to yield two poles with negative real parts, and the poles move toward the left as ξ increases. It also shows that the poles move toward the right as the inertia constant H increases, because that ω_n decreases along with H and hence lead to slower poles. In any case, the poles stay in the left half plane in the common range of H.

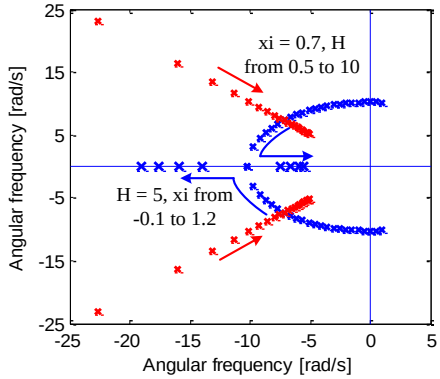

Fig. 4.4. Root loci under changes of the damping factor and inertia constant.

Fig. 4.5 shows the change of the open-loop system phase affected by the damping factor, ξ, inertia constant, H, and droop gain, R_d.

It can be observed in Fig. 4.5(a) how the damping factor has a dominant influence on the system phase margin. The system phase margin increases along with the increase of the damping factor. As Fig. 4.5(b) and (c) show, the inertia constant and droop gain have only minor influence on the phase of the open-loop system. Therefore, the inertia constant and droop gain can be specified considering the requirement of the transmission system operator (TSO) and the available power reserve without affecting significantly the system stability.

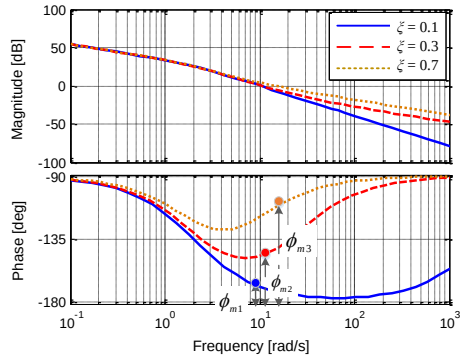

(a)

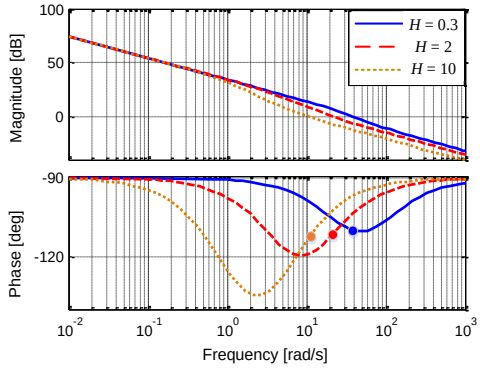

(b)

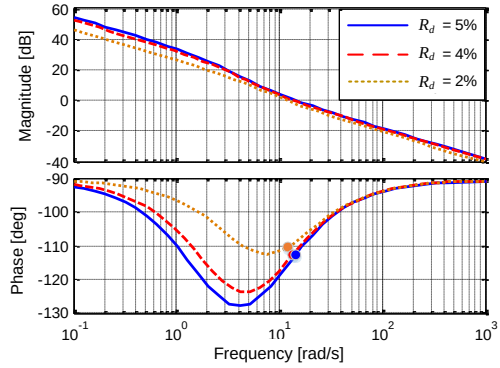

(c)

Fig. 4.5. The influence of the damping factor, inertia constant and droop gain on the system phase: (a) the influence of the damping factor, (b) the influence of the inertia constant, (c) the influence of the droop gain.

4.3.3 Transient analysis

The transient response of the active power control loop is evaluated by the closed-loop system unitary step response. The settling time and overshoot of the response are taken as the performance indicators, and they are calculated by (3.16) and (3.29) in Chapter 3, respectively. The steady-state value is obtained at t = 3 s.

H, ξ and R_D are specified with multiple values to define the system. According to (4.3b) and (4.4), it is easy to find that the natural frequency ω_n is inversely proportional to the square root of the inertia constant H, and the time response is proportional to the square root of H, which is written as:

$$t_{ss} \propto \frac{1}{\omega_n} \propto \sqrt{H} \cdot \tag{4.26}$$

Fig. 4.6(a) shows how the settling time increases as the inertia constant increases and follows the (4.26) relationship.

Fig. 4.6(b) shows that the damping factor and droop gain have minor influence on t_{ss}, except that t_{ss} increases significantly when a poor damping is set.

Fig. 4.6(c) shows how the damping factor has a considerable influence on the overshoot of the transient response. It can be concluded that t_{ss} should be not only greater than zero to guarantee the stability, but a limit of overshoot should also be set, and thereby the control parameter K_P will be tuned.

Fig. 4.6(d) shows that the overshoot also increases along with the inertia constant. However, this trend is limited in an acceptable range under a given value of ξ. The droop gain has only minor influence on the overshoot.

To summarize, it is shown how the integration of the droop control in the power loop controller does not introduce any effect on the dynamics. The transient response is still characterized by ξ and H, while R_d mainly determines the steady-state performance.

As previously mentioned, R_d is the droop gain that needs to be determined based on the utility grid requirements and the feasible power reserve. H can be designated considering the inertia constant of a traditional synchronous machine with the same power level. The damping coefficient ξ can be set considering the typical value range $0 < \xi < 1$ to create a stable and under-damped system.

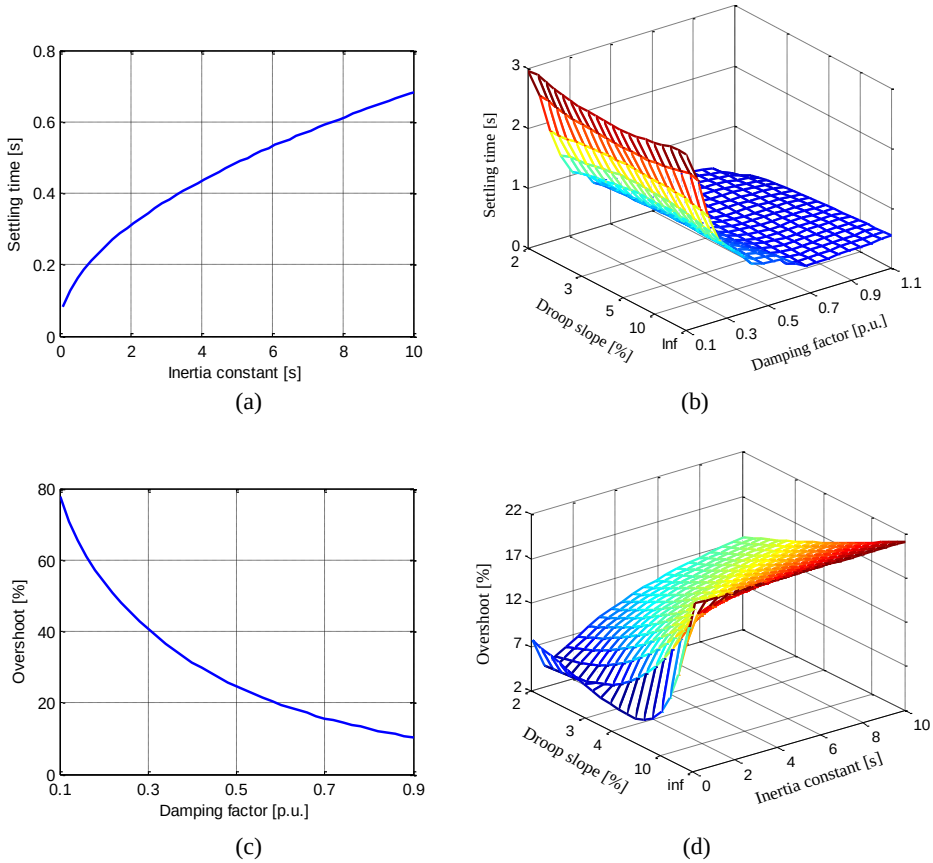

Fig. 4.6. The influence of the control parameters on the transient response settling time and overshoot: (a) the influence of the inertia constant on settling time, (b) the influence of the damping factor and droop gain on settling time, (c) the influence of the damping factor on overshoot, (d) the influence of the inertia constant and droop gain on overshoot.

4.4 PI-Based Power Loop Controller

The commonly used PI controller can also be used as an alternative to implement the power loop controller. The PI-based power loop controller achieves to make the output regulated power equal to the reference value in steady state, even if there are variations in the grid frequency. In this way, a precise power tracking control can be simply achieved, without using any additional droop loop. Moreover, setting parameters for the external droop controller is straightforward and simple, since the power loop based on a PI controller does not have intrinsic droop. In addition, given values for the inertia and the damping characteristics can be guaranteed by properly setting the PI controller gains.

The PI controller used for the power loop has the following form:

$$G_{PLC}(s) = K_X + \frac{K_H}{s}. \tag{4.27}$$

Using it as the power loop controller block in Fig. 4.1, the resulting closed-loop transfer function can be generically written as:

$$\frac{\partial P}{\partial P_{ref}}(s) = \frac{2\xi\omega_n s + \omega_n^2}{s^2 + 2\xi\omega_n s + \omega_n^2}, \tag{4.28}$$

where the damping coefficient and natural frequency are respectively given by:

$$\xi = \frac{K_X}{2}\sqrt{\frac{P_{\max}}{K_H}}, \tag{4.29a}$$

$$\omega_n = \sqrt{P_{\max} K_H}. \tag{4.29b}$$

Therefore, the PI-based power loop controller gain, K_H, should be set according to:

$$K_H = \frac{\omega_n^2}{P_{\max}}. \tag{4.30}$$

Like what was done to the CND controller, the natural frequency, ω_n, in this case, can also be translated to the moment of inertia, J, by equating the two ω_n in (4.3b) and (4.29b). Then (4.30) changes to:

$$K_H = \frac{1}{J\omega_s}, \tag{4.31}$$

which changes to (4.32), expressed in terms of H.

$$K_H = \frac{\omega_s}{2HS_N} \tag{4.32}$$

Substituting the K_H in (4.29a) using (4.32), the mechanism to set K_X is obtained, expressed as:

$$K_X = \xi\sqrt{\frac{2\omega_s}{P_{\max} HS_N}}. \tag{4.33}$$

The power response in presence of grid frequency changes will be given by:

$$\frac{\partial P}{\partial \omega_g}(s) = \frac{-P_{\max} s}{s^2 + 2\xi\omega_n s + \omega_n^2}, \tag{4.34}$$

from which, the steady-state droop gain is obtained as:

$$D_p = \left| \frac{\partial P}{\partial \omega_g}(0) \right| = 0 \cdot \tag{4.35}$$

It indicates that the power generated by the power converter will always track the power reference in steady state, regardless of whether the grid frequency changes or not.

According to (4.32) and (4.33), the control parameters K_X and K_H can be easily set from given values for ξ and H.

4.5 Analytical Comparison of Different Power Loop Controllers

Focused on virtually inertia implementation in grid connected power converters, this section compares three different types of power loop controllers to be used in the SPC structure, namely, the swing equation emulation (Section 4.2), the configurable natural droop (Section 4.3) and the PI (Section 4.4).

For each type of controller, analytical relationship between response characteristic parameters, H, ξ and R_D, and controller gains have been discussed in previous sections. Dynamics of these three controllers is compared in this section by using numerical models. In this analysis, different values of H are respectively set for each type of controller, while ξ is set to 0.7. A unitary step in active power reference is given as an input, and active power response in each case is respectively calculated through the transfer functions shown in (4.2), (4.14) and (4.28). Such active power responses are shown in Fig. 4.7.

As Fig. 4.7 shows, the time of response can be changed by adjusting the inertia constant H. In this figure, responses for H = 5 s and H = 10 s are shown. When the steady state band is defined to be equal to 2% , then the settling time for the two responses is respectively 586.6 ms and 829.7 ms in Fig. 4.7(a), while in Fig. 4.7(b), these values are respectively 544.1 ms and 732.4 ms, and in Fig. 4.7(c) they are respectively 479.0 ms and 677.5 ms. It is observed that the settling time for H=10 is always close to the settling time when H=5 multiplied by $\sqrt{2}$, which matches with the relationship given by (4.26).

The results show that all the 3 types of power loop controller can present inertial characteristic given by (4.26), and an equivalent inertia constant can be accurately given by setting the controller gains through (4.5a), (4.18) and (4.32), respectively.

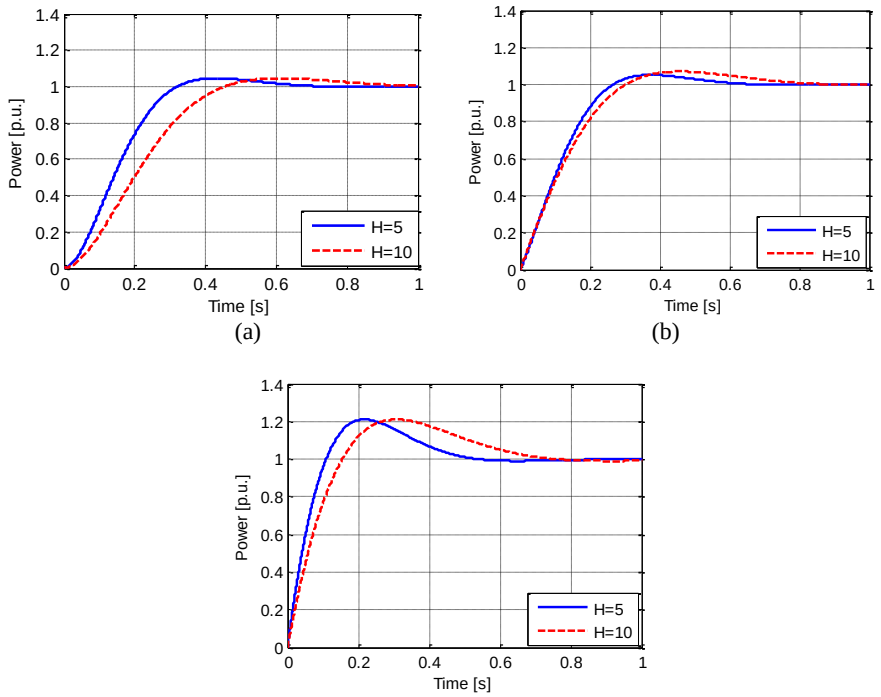

Fig. 4.7. Unitary step response of the *P*-*P** transfer function under different values of *H* when ξ=0.7: (a) swing equation emulation, (b) configurable natural droop, (c) PI.

4.6 Test Results of the Power Loop Controllers

4.6.1 Simulation results

Simulation tests are conducted to show the performance of the previously introduced CND controller in providing grid frequency support and in island operation.

A. Grid frequency support

A simulation model for a 10 kW two-level three-phase grid-connected converter was built, which is described in Appendix A.1. The key parameters of the setups and the controller are shown in Table 4.1. In this simulation, the CND controller was used as the power loop controller of the SPC to control the power converter.

In order to show the response of the active power as a function of the grid frequency changes, a simple Thevenin model was used to form the grid. For an easy evaluation and comparison of the experimental results, all the tests are done considering the same value for the damping coefficient ξ, which is set to 0.7. The virtual admittance value is set according to regular values in synchronous machines [45]. The per-unit value of virtual reactance is

set to 0.3, corresponding to 15.3 mH, while the per-unit value of virtual resistance is set to 0.1 for having sufficient damping, corresponding to 1.6 Ω.

Table 4.1 Key experimental parameters for power loop controllers' validation

Description	Symbol	Value
grid phase-to-phase voltage	V_g	400 [V]
grid nominal frequency	f_g	50 [Hz]
dc bus voltage	V_{DC}	640 [V]
power converter nominal power	P_N	10 [kW]
switching frequency	f_{sw}	10050 [Hz]
damping coefficient	ξ	0.7 [p.u.]
virtual resistance	R_{pu}	0.1 [p.u.]
virtual reactance	X_{pu}	0.3 [p.u.]

The ramp in the grid frequency shown in Fig. 4.8(a) is implemented as an input in the simulation test, and the active power response is measured. This simulation test is repeated for several times with different values for the inertia constant and the droop gain. Fig. 4.8(b) compares the power response profiles from different cases.

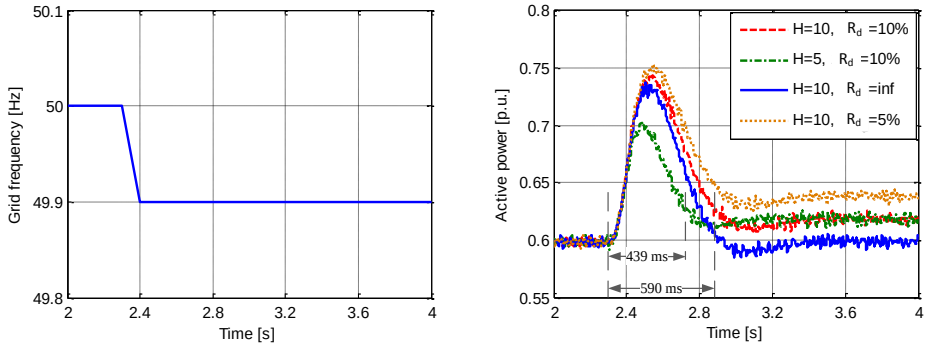

(a) (b)

Fig. 4.8. Simulated transient response under different values of inertia constant and droop gain: (a) grid frequency changes, and (b) active power response.

During the grid frequency change, the active power injection responds accordingly to minimize frequency deviation and thereby providing some frequency support. In three different simulation cases shown in Fig. 4.8(b), the droop slope R_d is set to 5%, 10% and infinite (D_P=0), while the inertia constant H is set to 10 s. As it is shown in the figure, the steady-state value of active power reaches 0.64, 0.62 and 0.6, respectively. Considering that the deviation of grid frequency is 0.1 Hz, the steady-state active power injection matches with the specified droop gain. For evaluating the inertial characteristic of the controller, R_d is set to 10%, and H is set to 5 s and 10 s in two different simulation cases. As R_d is the same for both simulation cases, the two resulting active power waveforms reaches the same steady-state value (0.62 p.u.). The settling time of the two responses is then calculated considering a steady-state band of 5%. The settling time when H=10 s is 590 ms, while the

settling time when H=5 s is 439 ms. It validates the relation given by (4.26). In summary, the specified inertial dynamics and the droop gain can both be achieved by using this power loop controller.

B. Islanding and Load Sharing

A SPC-based power converter is able to feed an island, similarly to a synchronous machine. Moreover, by using the control scheme shown in Fig. 2.1 in Chapter 2, and the power loop controllers previously presented, several power converters can run in parallel to form an island. It is worth noting that the active power reference will not dominate the active power injected by the power converters in island operation, instead, the active power injection will be determined by the value of the virtual admittance and the *P-f* droop characteristics.

Fig. 4.9 shows a study case where a 100 kW and two 10 kW converters are connected in parallel to a grid to supply 100 kW local loads. The CND controller was used as the power loop controller of the SPC to control the power converters in this simulation.

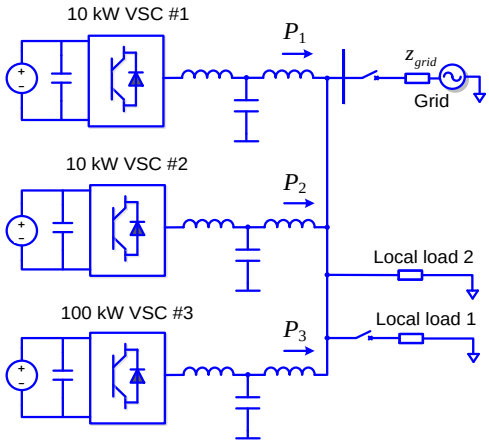

Fig. 4.9. A study case based on three paralleled grid connected power converters with different rated power for island working tests.

According to (2.3) and (4.12), the power variation of a generation unit can be expressed by:

$$\Delta P_{pu} = \frac{\Delta P}{S_N} = \frac{1}{X_{pu}} \Delta\delta \cdot \tag{4.36}$$

In this simulation case, the values of virtual reactance for all the power converters are set to the same per-unit value to achieve a proportional load sharing.

As an initial operation point, the grid connection switch is closed, and the power injection of the 3 converters are 8 kW, 7 kW, and 70 kW, corresponding to 0.8 p.u., 0.7 p.u. and 0.7 p.u., respectively, and the local load is partially fed by the main grid.

Two events are considered in the case study. At t = 1.2 s, the main grid is disconnected, while at t = 1.3 s, the step change in a local load takes place. Fig. 4.10 shows some plots describing the response of the system.

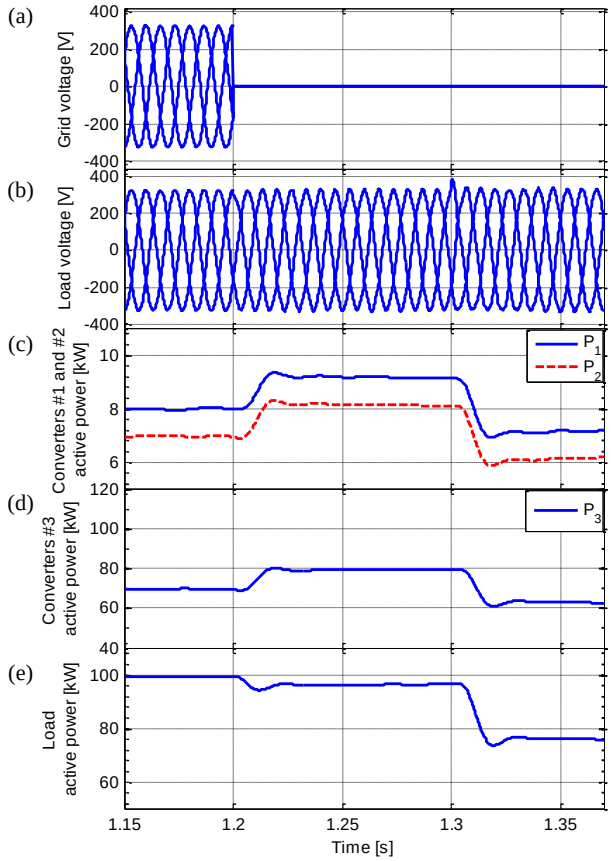

Fig. 4.10. The responses of the paralleled power converters under islanding and load changes: (a) grid voltage, (b) load voltage, (c) active powers injected by the converter #1 and #2, (d) (c) active power injected by the converter #3, (e) active power consumed by the load.

Regarding the first event, the local voltage in the island is well maintained when the main grid is disconnected as Fig. 4.10(b) shows, thanks to the grid forming capability of the power loop controller. The local voltage magnitude drop when the main grid is disconnected is calculated to be 4.22%, which is an acceptable value. As a response to this event, all the 3 power converters increase their power injection. As Fig. 4.10(c) and (d) show, the incremental power is around 0.1 p.u. for all of them (referred to the rated power of each converter). It complies with the virtual reactance setting for all the power converters. In this simulation, the minor drop in the power consumed by the passive loads, as Fig. 4.10(e) shows, is due to the drop of the voltage magnitude.

During the second event, 20% of the local load is switched out. As can be appreciated in Fig. 4.10(b), the local voltage is well maintained after a short transient, and all the power

converters decrease their power injection proportional to their rated power as Fig. 4.10(c) and (d) show.

4.6.2 Experimental results

A laboratory experimental setup was constructed in this PhD project to further validate the power loop controllers presented previously. Such experimental plant is described in Appendix B.1, and the key parameters of the setup are the same as in simulations as Table 4.1 shows.

A. Experimental results compared to transfer function analysis and simulation

Steps in power reference and grid frequency sweeps were made to validate the dynamic performance of the CND power loop controller.

Fig. 4.11 shows the active power response resulting from calculation, simulation and experiments in case of a power reference step. The control parameters are configured by setting H = 5 s and D_P = 20 kW/Hz. The calculated response is obtained from the transfer function (4.14). The simulated response is obtained from a simulated model of the power converter and the controller. The experimental response is obtained from data recorded by the dSPACE system. The responses obtained from the different methods are coherent with each other when the same input is given, i.e. a step in the active power reference, from 5 kW to 10 kW.

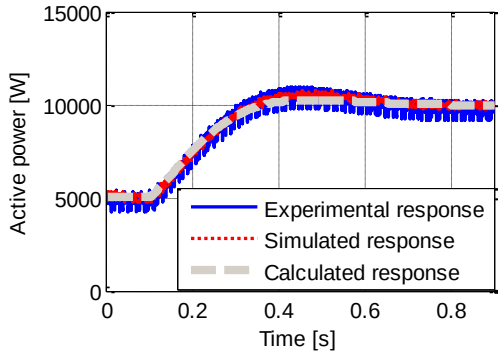

Fig. 4.11. Experimental result of the CND power loop controller comparing with simulation and calculation under a power reference step.

Fig. 4.12 shows the transient active power response in the presence of a grid frequency sweep. Fig. 4.12(a) shows the programmed frequency sweep, where the ramp slope is 1 Hz/s. Fig. 4.12(b) shows the waveforms for the grid voltage and current injected by the converter during the frequency sweep. It can be observed in this figure how the current is well controlled in steady state and exhibit a significant transient response to compensate the change of the grid frequency. It should be also noted how the converter presents a smoothed response during transients.

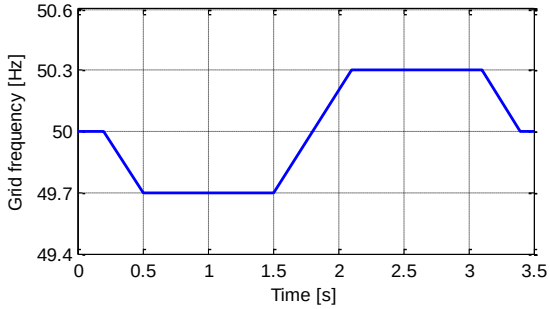

(a)

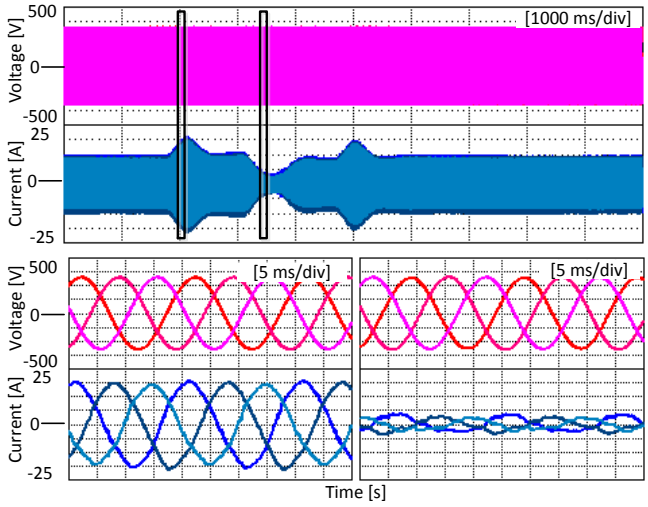

(b)

Fig. 4.12. Experimental result of the CND power loop controller under a grid frequency sweep: (a) grid frequency profile, and (b) grid voltage and injected current.

Fig. 4.13(a) compares the response of active power obtained by transfer function response plotting, simulation and experimental test. In the three cases the controller works with the same set of parameters. The transfer function shown in (4.19) is used for this comparison. Fig. 4.13(a) shows a perfect response match from the three different cases. It validates how the transient response of the grid-connected converter in practice perfectly follows the dynamics of transfer function (4.19). In this way, the damping, inertia and droop characteristics can be accurately set and the feasibility of this controller is experimentally demonstrated. In this test, the *P-f* droop gain is set to 10%. The measured active power delivered by the power converter takes a steady-state value of 0.56 p.u. when the grid frequency holds at 49.7 Hz, and 0.44 p.u. when the grid frequency holds at 50.3 Hz.

Fig. 4.13(b) shows the evolution of the virtual synchronous angular speed ω. As appreciated in this figure, a high value for inertia constant (H=10 s) results in a long settling time in the grid frequency tracking, longer than the one in a traditional loop based on a PLL.

The difference between ω and ω_g during the transient leads to a significant active power inertial response to compensate such a frequency deviation.

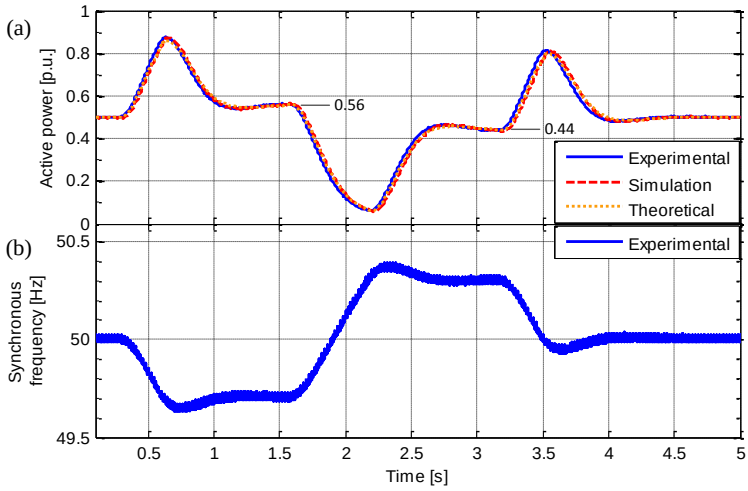

Fig. 4.13. Experimental result analysis of the CND power loop controller under a grid frequency sweep: (a) experimental active power response comparing with simulation and calculation, and (b) the inner virtual synchronous frequency of the experimental converter.

B. Inertial and droop characteristics of the CND controller

Fig. 4.14 shows the transient responses of the power converter when different values are set for the inertia constant *H*.

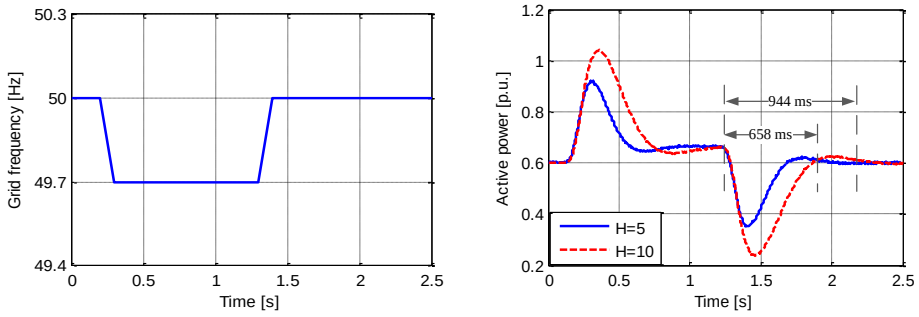

(a) (b)

Fig. 4.14. Comparison of the active power transient responses of the CND power loop controller under a grid frequency sweep under different values of inertia constant: (a) grid frequency profile, and (b) comparison of active power responses.

The frequency profile that triggers the active power responses is shown in Fig. 4.14(a). The frequency ramp slope in this figure is 3 Hz/s. The initial operating point of the power converter is 6 kW and 0 kVar. The active power responses for two different inertia constant values, H = 5 and H = 10, is measured and shown in Fig. 4.14(b). The settling times for

both values of H in response to the frequency profile are 944 ms and 658 ms. It is easy to calculate that $944/658 = 1.43 \approx \sqrt{10/5}$, which matches with (4.26).

The droop characteristic of the power converter is shown in Fig. 4.15. The grid frequency variation is plotted in Fig. 4.15(a), where it decreases to 49.9 Hz during 0.1 s, holds for 1 s and increases back to 50 Hz during 0.1 s. In three simulation cases, the droop gain R_D is set to infinite (D_P=0), 10% and 5%, corresponding to 0 kW/Hz, 2 kW/Hz and 4 kW/Hz, respectively. Fig. 4.15(b) shows the transient active power responses. It can be observed in this figure how the active power steady-state value after the first frequency ramp is 0.6 p.u., 0.62 p.u. and 0.64 p.u., respectively, according to the programmed droop gains.

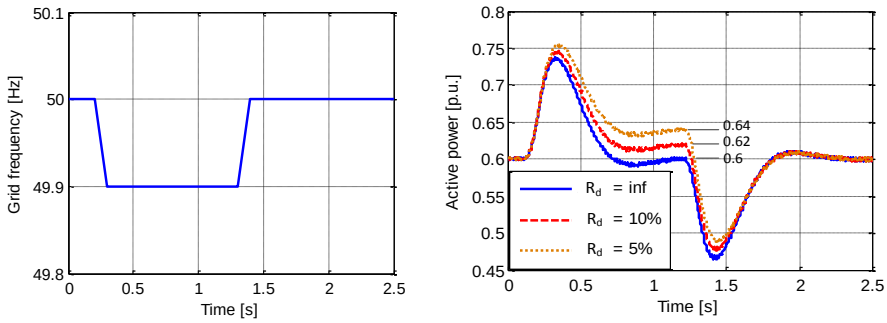

(a) (b)

Fig. 4.15. Comparison of the active power transient responses of the CND power loop controller under a grid frequency sweep under different values of droop gain: (a) grid frequency profile, and (b) comparison of active power responses.

In summary, these experimental results verify the inertial and droop response of the controller in case of grid frequency changes. The good matching in the transient active power responses obtained from the transfer function, the simulation and the experimental results validates the effectiveness and the easy implementation of the previously presented controller.

C. A comparison between the CND and the MPL controllers

A comparison between the CND controller and the typical MPL controller is presented in the following. The responses of the power converter in presence of active power reference step and grid frequency variation were considered in such comparison. In cases of grid frequency variation, it is considered that the frequency decreases from 50 Hz to 49.9 Hz during 0.1 s, and then after 1 s, increases again to 50 Hz taking 0.1 s.

The CND controller is firstly evaluated by observing experimental results from two test cases. In the first case, a 5 kW to 10 kW step in the active power reference is given as an input. The controller is configured with H = 10 s and D_P = 2 kW/Hz. The injected current waveforms, as well as the injected active and reactive powers, are shown in Fig. 4.16. As Fig. 4.16(b) and (c) show, these active and reactive power waveforms were preprocessed by a washout filter to remove any high frequency noise. As shown in Fig. 4.16, the grid injected current and power present a smooth underdamped variation thanks to the inertial characteristic of the power loop controller, instead of a sharp step. The transient response,

with no remarkable oscillations, also shows a proper damping of the system. Moreover, the injected active and reactive powers are accurately controlled in the steady state.

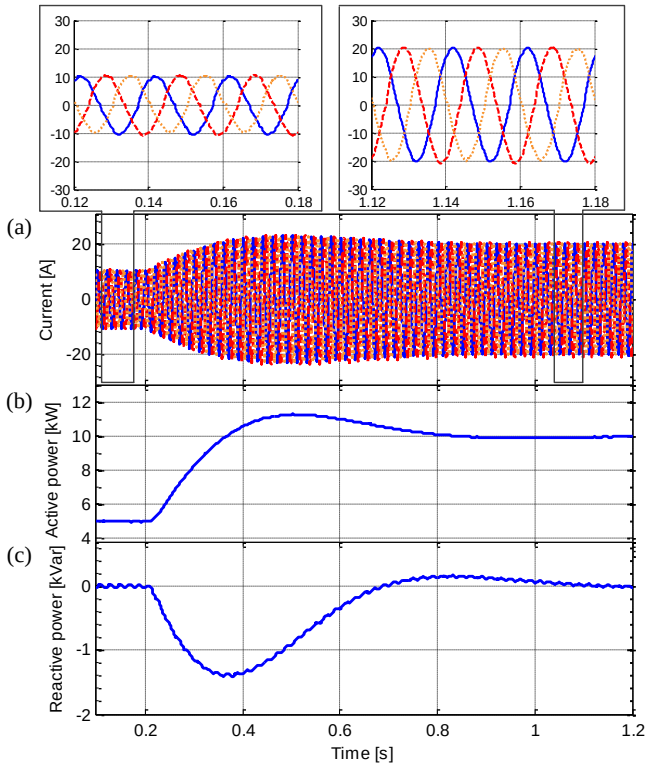

Fig. 4.16. Experimental response of the power converter based on the CND controller under an active power reference step. H=10 s and D_P=2 kW/Hz: (a) three phase current injected to the grid, (b) active power injected to the grid, (c) reactive power injected to the grid.

In the second test case, a grid frequency variation is programed in the ac power source. In this case, the power reference is set to 6 kW and 0 kVar, and the controller has the same parameters as in the previous case. The power response is shown in Fig. 4.17(b). The injected current and power respond to the grid frequency variation, which evidence the power synchronizing behavior of the power loop controller. When the grid frequency decreases by 0.1 Hz, the active power becomes equal to 6.2 kW in steady state, according to the droop gain D_P (2 kW/Hz). The virtual synchronous frequency of the power converter also shows the inertial characteristic of the power loop as well as an accurate synchronization with the grid frequency in steady state.

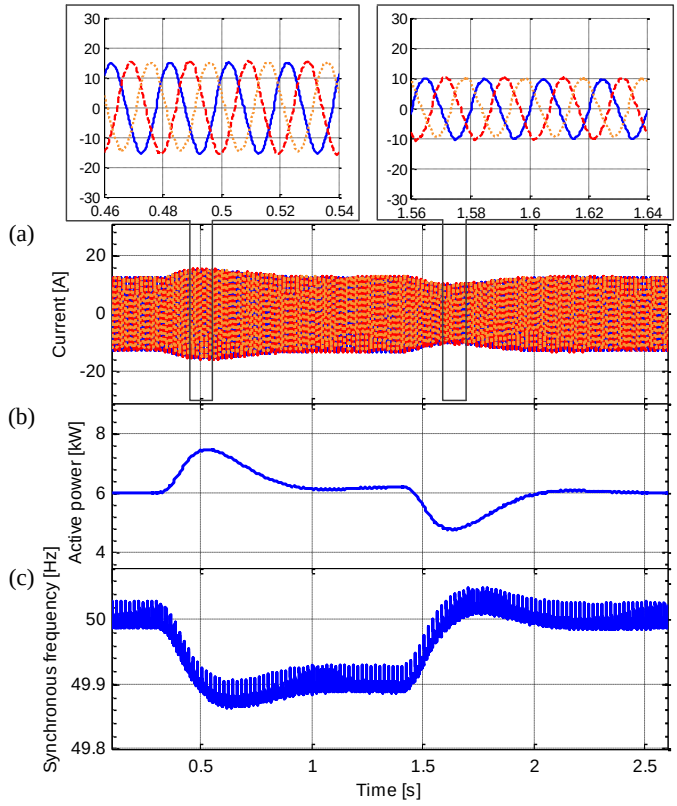

Fig. 4.17. Experimental response of the power converter based on the CND controller under grid frequency changes. H=10 s and D_P=2 kW/Hz: (a) three phase current injected to the grid, (b) active power injected to the grid, (c) inner virtual synchronous frequency of the power converter.

The MPL controller is also evaluated for the two test cases previously described and the results are shown in Fig. 4.18 and Fig. 4.19. The inertia constant is set to the same value as the previous test cases, namely, H = 10 s.

Fig. 4.18 shows the current and power responses in front of a step in the power reference. In comparison to the CND controller, the MPL controller results in a response with greater settling time and lower overshoot.

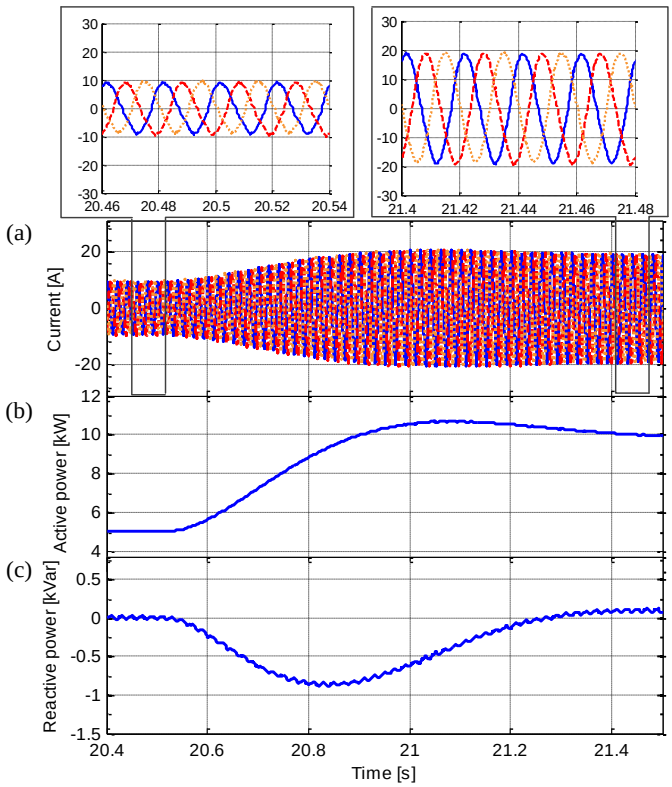

Fig. 4.18. Experimental response of the power converter based on the MPL controller under an active power reference step. *H*=10 s: (a) three phase current injected to the grid, (b) active power injected to the grid, (c) reactive power injected to the grid.

Fig. 4.19 shows the current and power responses in front of a grid frequency variation. Such frequency variation is the same as the one when the CND controller was used. The intrinsic droop characteristic of the MPL controller can be appreciated in Fig. 4.19. When the grid frequency changes from 50 to 49.9 Hz, the injected active power increases from 6 kW and reaches a 10 kW steady state value, as Fig. 4.19(b) shows. This value is coherent with the theoretical droop gain, which is equal to 40.522 kW/Hz according to (4.8). Then, as long as the grid frequency deviates by 0.1 Hz, the power injected by the power converter will change by 4 kW (0.4 p.u.), which could be much greater than the desired value. In order to adjust the power converter droop gain, an external *P-f* droop loop has to be added to compensate the inherent droop characteristic of the MPL controller.

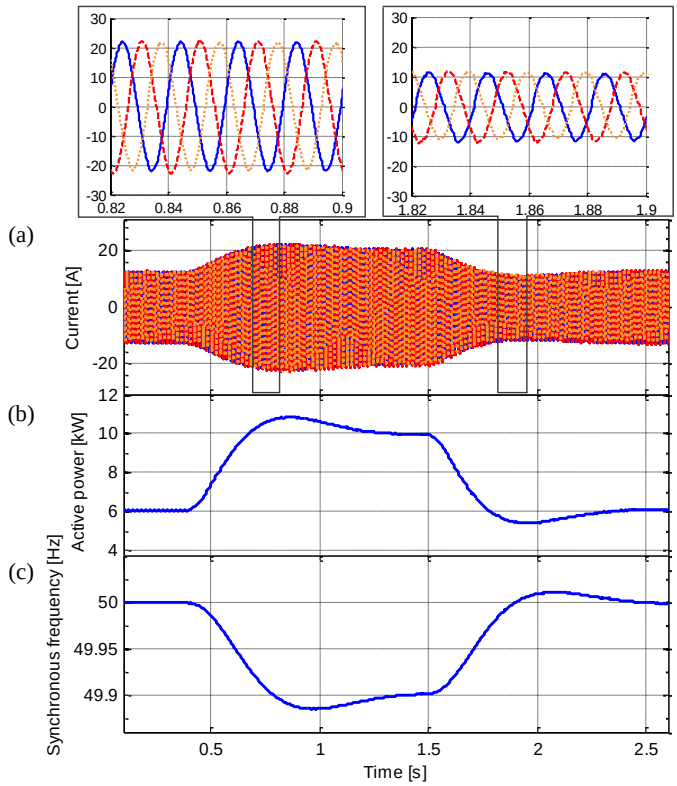

Fig. 4.19. Experimental response of the power converter based on the MPL controller under grid frequency changes. *H*=10 s: (a) three phase current injected to the grid, (b) active power injected to the grid, (c) inner virtual synchronous frequency of the power converter.

Fig. 4.20 offers a clearer comparison of the power responses associated to the CND and the MPL controllers in case of grid frequency variation.

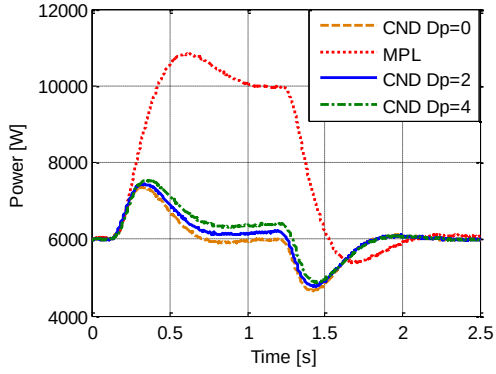

Fig. 4.20. Active power responses to grid frequency changes based on the CND and MPL controller, when *H*=10 s.

D_P is set to 0, 2 and 4 kW/Hz in three different tests conducted on the CND controller. For the MPL controller, the value of D_P depends on H and ξ. The steady-state value of the active power delivered by the power converter based on a CND controller matches in each test case with the corresponding value setting for D_P, which shows the configurability of the droop ratio in the CND controller. In contrast, the MPL controller exhibits a stronger droop effect.

The above experiments have demonstrated the different inherent *P-f* droop characteristics of the CND and MPL controllers. On the other hand, the responses of the power converter in presence of an active power reference step are similar, based on these two control strategies.

D. A comparison between the SPC and a conventional power converter control

This part presents some experiments to compare the response of a SPC-based power converter and the one from a power converter based on a conventional control. The control structure of the SPC was shown in Fig. 2.1 in Chapter 2, and the CND controller presented in this chapter is used as the power loop controller. The conventional control structure was shown in Fig. 3.21 in Chapter 3. Since this conventional control strategy consists of the vector current control (VCC), PLL and IARC, it is referred as VCC in the context.

As a first test, a step change in the reference power, from 0.5 p.u. to 1 p.u., is programmed to compare the dynamic response of the power converter. The response of the SPC-based power converter and the one of the VCC-based power converter are shown in Fig. 4.21 and Fig. 4.22, respectively. The inertia constant of the SPC is set as H = 5 s.

As Fig. 4.21(a) shows, the current injected by a SPC-based power converter has good waveform in steady state, and has smooth transient response, as well as the one that result from a VCC-based power converter as Fig. 4.22(a) shows. Both control strategies achieve accurate control of active and reactive powers in steady state. However, they result in considerably different transient responses of the power converter. The inertial effect of the SPC can be perfectly appreciated, which is observed by the significant difference in the active power settling time. For the SPC, the settling time of the active power is several hundreds of milliseconds as Fig. 4.21(b) shows, while the one for the VCC is several milliseconds as Fig. 4.22(b) shows.

Besides, the active power transient responses that result from both strategies present an overshoot, as Fig. 4.21(b) and Fig. 4.22(b) show. For the SPC, it can be explained by the active power control closed-loop transfer function, which is an under-damped second-order system thanks to the decoupling between the power loop and the current loop. For the VCC, it can be explained by the dominant poles defined by the PR controller gains, which results in a system that can be approximated to a under damped second-order system.

In both cases as Fig. 4.21(c) and Fig. 4.22(c) show, the reactive power presents an deviation during the transient, though the maximum deviation is only around 0.1 p.u.. This is because of the coupling of the active and reactive power control, for both strategies.

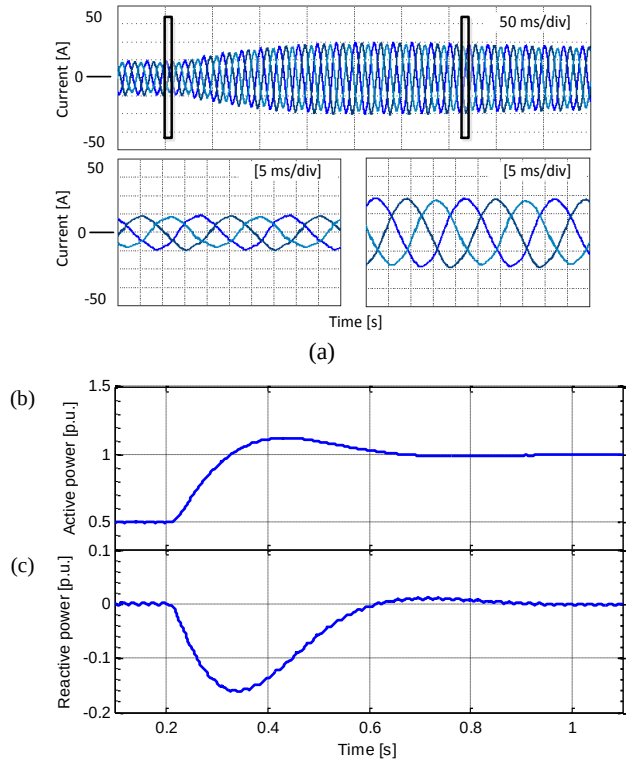

Fig. 4.21. Experimental response of a SPC-based power converter in presence of a power reference step: (a) current injected by the power converter, (b) active power injected by the power converter, (c) reactive power injected by the power converter.

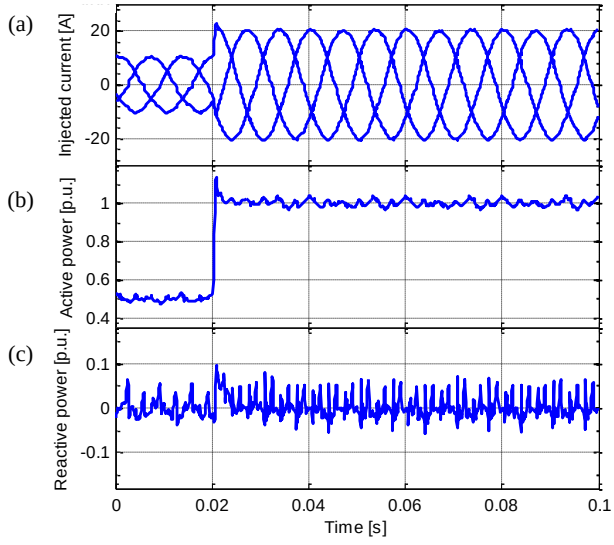

Fig. 4.22. Experimental response of a power converter based on VCC in presence of a power reference step: (a) current injected by the power converter, (b) active power injected by the power converter, (c) reactive power injected by the power converter.

As a second test, a frequency sweep was programmed, reproducing a disturbance in the ac grid-frequency. The frequency was programmed to change from 50 Hz to 49.7 Hz in a step at 0.5 s, maintaining this value for 1 s, and change back to 50 Hz in a step at 1.5 s. The steps in frequency were given only for evaluating the dynamics of the converter, even though the grid frequency does not experience such sharp changes in realistic applications.

Fig. 4.23(a) and (d) show how the injected current and power transient response of a SPC-based power converter aims to compensate the deviation of the grid frequency, emulating the inertia characteristic of synchronous machines. Besides, the experimental active power response of a SPC-based power converter matches its transfer function calculation, as Fig. 4.23(d) shows. In contrast, as Fig. 4.23(b) and (d) show, a power converter controlled by VCC does not react to the frequency change and simply remains synchronized with the electrical grid, with no changes in the active power delivered to the grid.

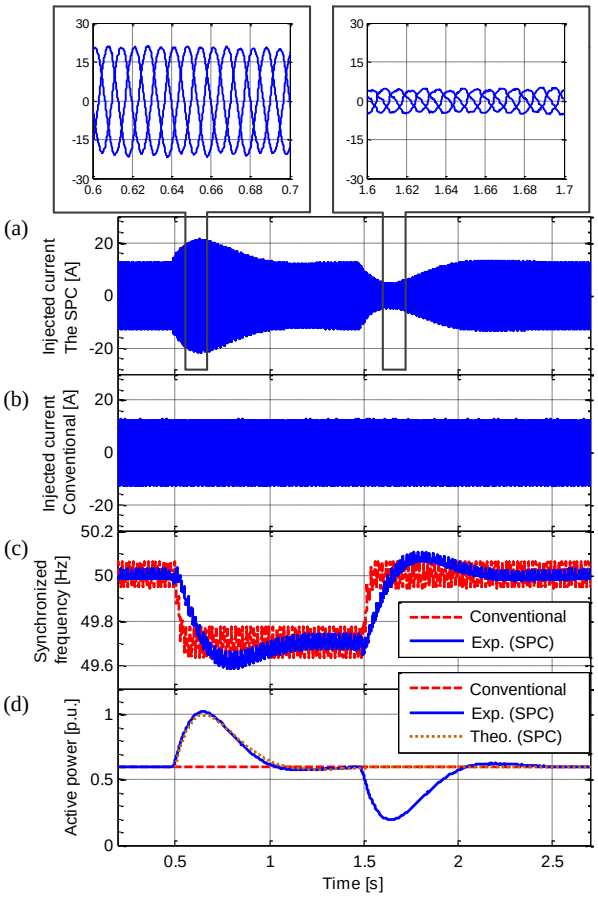

Fig. 4.23. Comparison of the experimental responses of the power converter controlled by different strategies under grid frequency steps: (a) current injected by the power converter based on the SPC, (b) current injected by the power converter based on the VCC, (c) comparison of the inner synchronized frequency of the two strategies, (d) comparison of the active power responses of the converter based on the two strategies.

Fig. 4.23(c) shows both the synchronized frequency generated by the SPC power loop controller and the grid frequency detected by the PLL [86]. Both signals show an accurate lock of the grid frequency in steady state, however, the SPC presents a damped frequency detection, which can be a remarkable feature regarding power converter operation stability when connected to weak ac grids connection under adverse grid conditions.

As a third test, a voltage dip is programmed in the ac power source and the responses for the VCC and the SPC based power converter are compared. In this test, the phase-to-neutral rms voltage of the three phases decreased from 230 V to 190 V for 1 s.

The response of the power converter based on the VCC are shown in Fig. 4.24, while the results based on the SPC are shown in Fig. 4.25. During the dip, both power converters remain connected to the grid and the injected current was stable in each case, as Fig. 4.24(b) and Fig. 4.25(b) show.

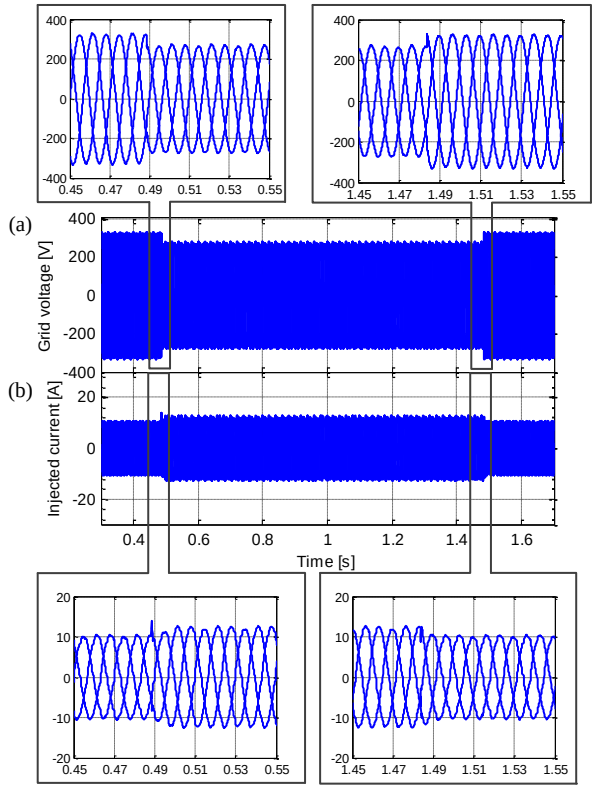

Fig. 4.24. Experimental response of the power converter controlled by VCC under a balanced grid voltage dip: (a) grid voltage, and (b) current injected by the power converter.

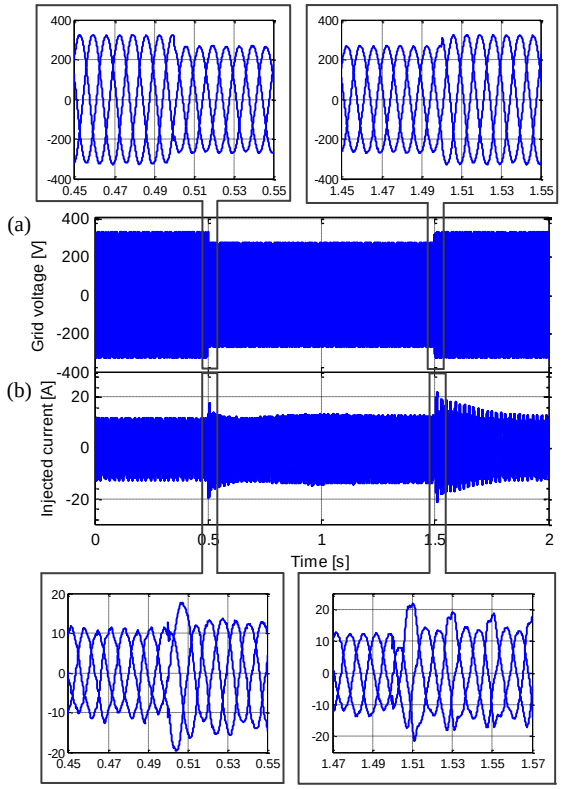

Fig. 4.25. Experimental response of the power converter controlled by the SPC under a balanced grid voltage dip: (a) grid voltage, and (b) current injected by the power converter.

Fig. 4.26 compares both strategies, and shows how the SPC-based power converter provides a significant voltage support during the voltage dip by injecting reactive current, thanks to the effect of the virtual admittance.

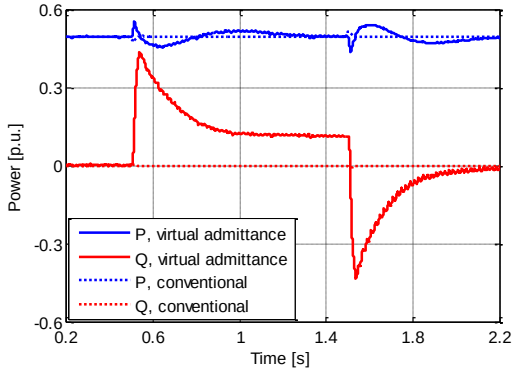

Fig. 4.26. Comparison of the reactive power injection of the power converter controlled by the two strategies during a balanced grid voltage dip.

Finally, the performance of the SPC is compared with the VCC when *P-f* droop control is enabled for both strategies. The same droop gain is set for the two strategies, namely 2%, as well as the same dead-band, namely 0.05 Hz. The responses of both controllers under grid frequency changes are shown in Fig. 4.27.

In order to highlight the difference between these two control strategies in grid-interaction dynamics, the frequency of the ac power supply is programmed to change in steps as Fig. 4.27(a) shows. The responses of the injected current for both the VCC and the SPC are respectively shown in Fig. 4.27(b) and (c), and the responses of active power for both strategies are compared in Fig. 4.27(d).

The main difference between both controllers appears in their transient response. The SPC-based power converter shows a remarkable transient response in front of grid frequency changes. When the grid frequency drops, the grid angle decreases, so the SPC-controlled converter delivers more active power aiming to compensate such a frequency drop. The power imbalance modifies the SPC virtual frequency and the load-angle until a new equilibrium is reached. During the transient, the SPC-based power converter delivers part of its virtual kinetic energy, naturally compensating the frequency drop.

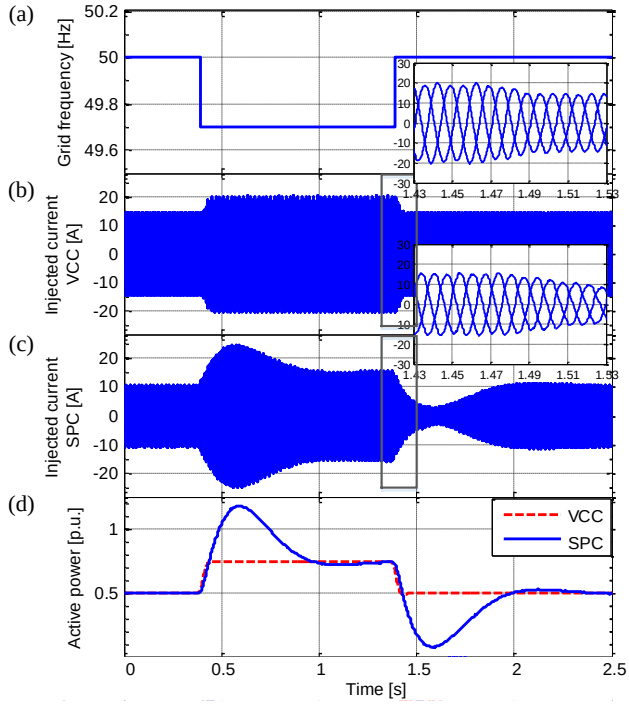

Fig. 4.27. Comparison of the experimental responses of the power converter controlled by different strategies under grid frequency steps. Droop control enabled for both strategies: (a) grid frequency, (b) current injected by the power converter based on the VCC, (b) current injected by the power converter based on the SPC, (c) comparison of the active power responses of the converter based on two strategies.

E. Performance of the power loop controller with a PI

The SPC based on a power loop controller with a PI is also evaluated in this section. Results from four different tests are shown in the following.

As a first test, a step in the power reference, from 0.5 p.u. to 1 p.u., is programmed to validate the dynamic performance of the controller. To clearly show the inertial characteristic of the controller, H is set to 10 s, which is a quite high value. The grid voltage and injected current waveforms are shown in Fig. 4.28, and the active power, the reactive power, the virtual synchronous frequency, ω, and the phase-angle of the virtual electromotive force, θ, are plotted in Fig. 4.29.

As shown in Fig. 4.28 and Fig. 4.29(a), the injected current and the delivered power change smoothly, showing the typical response of a second-order system. Both transient and steady-state responses present a good damping and an accurate active and reactive power control.

Fig. 4.29(a) shows the experimental active power step response and the response of the transfer function (4.28), where it can be appreciated the good realization of the inertial characteristic. The virtual synchronous frequency ω is shown in the Fig. 4.29(c), demonstrating how the good performance of the power-based grid synchronization is well achieved. The phase-angle signal θ, as Fig. 4.29(d) shows, is used to generate the virtual electromotive force.

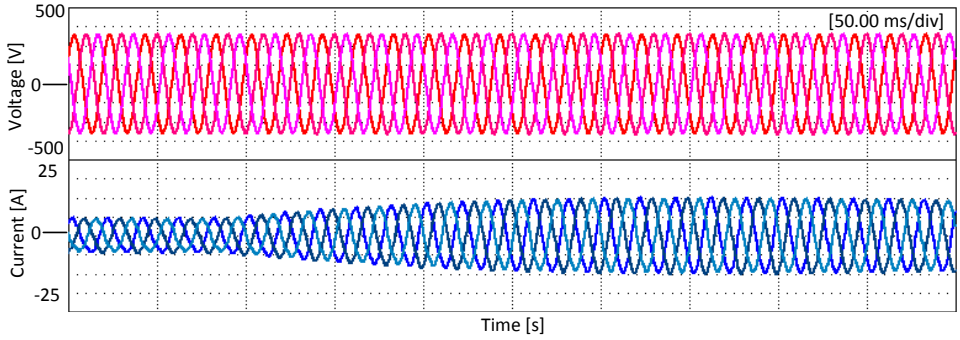

Fig. 4.28. Experimental result of the PI-based power loop controller under an active power reference step. Grid voltage and injected current.

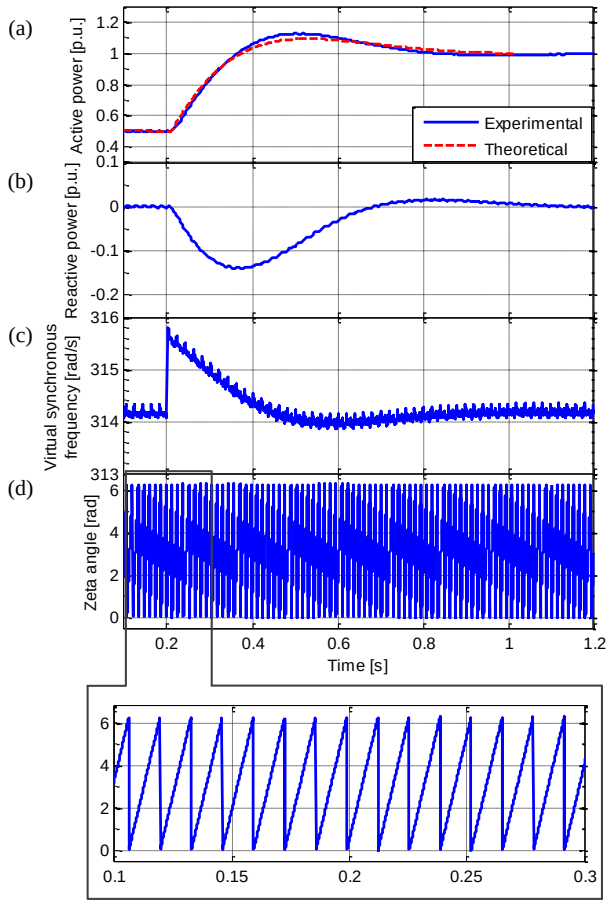

Fig. 4.29. Experimental response of the power converter based on the PI-based power loop controller under an active power reference step. H = 10 s: (a) active power injected by the converter, (b) reactive power injected by the converter, (c) inner virtual synchronous frequency of the power converter, (d) phase-angle of the virtual electromotive force.

As a second experimental test, grid frequency variations are programmed in the ac regenerative power source as Fig. 4.30(a) shows, with a frequency changing slope of 1Hz/s. The response of the injected current, active and reactive power and virtual synchronous frequency are shown in Fig. 4.30(b), (c), (d) and (e), respectively.

In this test, the active power reference is set to 0.5 p.u., the reactive power reference to 0, and the inertia constant H is set to 10 s. Moreover, the gain of the external droop controller K_{DP} is set to 0. The experimental results confirm that the injected current and power aim to compensate the grid frequency deviation. The controlled active power goes back to its reference in steady state, as Fig. 4.30(c) shows, which confirms that the no inherent droop gain exists when the PI controller is used.

The programmed frequency profile is used as an input for the transfer function (4.34), and its output is plotted in Fig. 4.30(c), together with the experimental active power profile

measured in the test. It validates the accurate implementation of the designed inertial characteristic. The perfect match between the experimental power response and the one from the transfer function (4.34) also demonstrates that the inner current control loop does not affect the inertial characteristic of the power control loop, thus confirming that both loops are not coupled. Besides, the virtual synchronous frequency ω shows an accurate locking of the grid frequency in steady state.

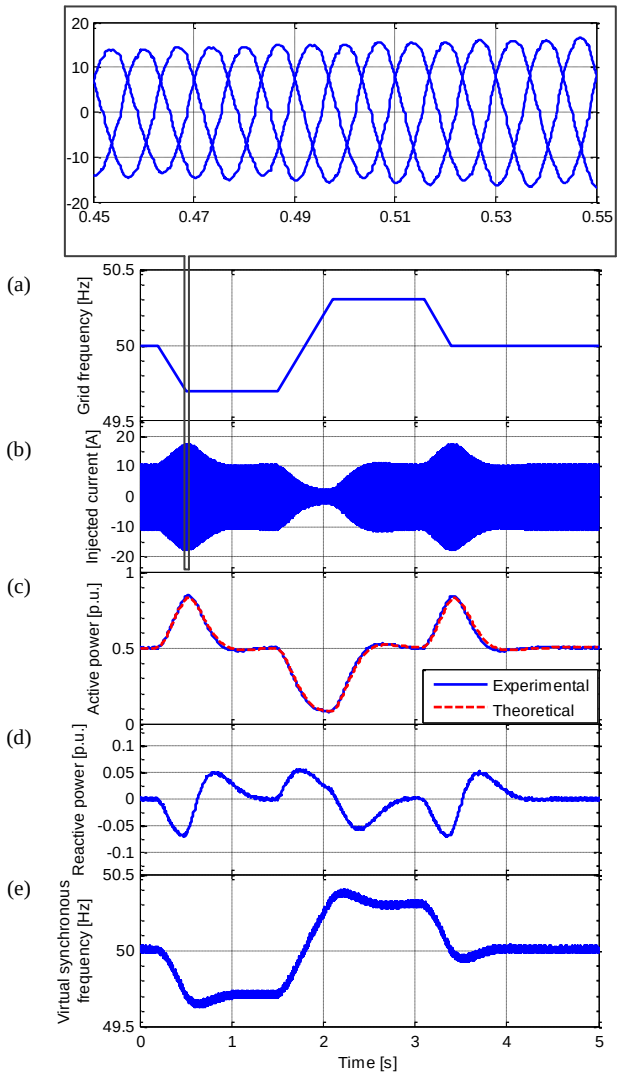

Fig. 4.30. Experimental response of the power converter based on the PI-based power loop controller under a grid frequency sweep. H = 10 s: (a) grid frequency, (b) current injected by the converter, (c) active power injected by the converter, (d) reactive power injected by the converter, (e) inner virtual synchronous frequency of the power converter.

As a third test, the performance of the external droop controller is evaluated. Since the PI-based power loop controller does not contain any inherent *P-f* droop characteristic, the

droop gain should be set by the controller structure shown in Fig. 2.2 in Chapter 2, as an outer loop. The droop gain was set to 2% by making K_{DP} = 1591.5 W/(rad/s). For the sake of simplifying, the dead band ω_{db} is set to 0. In the test, the active power reference of the converter is set to 0, and the grid frequency is decreased step by step from its nominal value, recording the value of the delivered active power at each value of frequency. The relation between the power and frequency is plotted in Fig. 4.31, where the slope of the recorded operation points matches the droop loop gain.

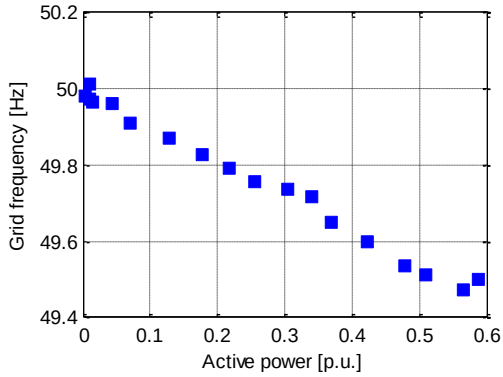

Fig. 4.31. Power-frequency droop characteristic of the external droop controller under 2% droop gain when the PI-based power loop controller is used.

Finally, a fourth test is conducted to show the effect of the virtual admittance in grid voltage support during an unbalanced voltage sag. In this test, the rms grid voltage of one of the phases is set down to 30 V for 1 s. Fig. 4.32 and Fig. 4.33 show the response of the power converter in front of such event.

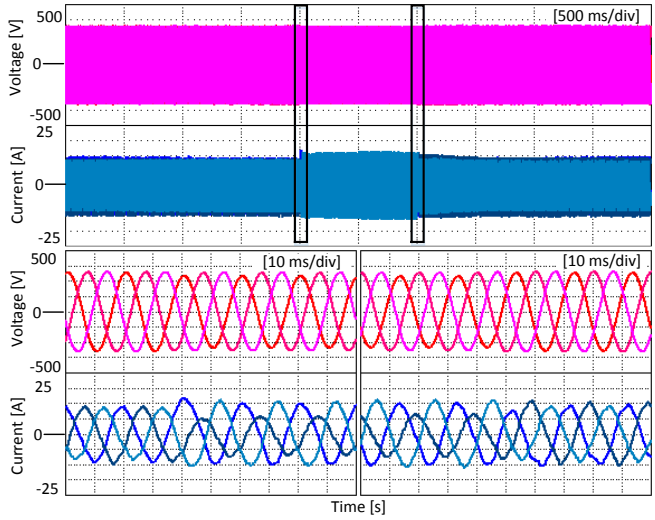

Fig. 4.32. Experimental voltage and current waveforms of the PI-based power loop controller under an unbalanced voltage dip.

The injected unbalanced current during the fault, as Fig. 4.32 shows, can be explained by

the unequal reactive power injection in each phase, which is shown in Fig. 4.33(b). For the phase A, where the voltage magnitude drops, the reactive power injection is significantly greater than for the other two phases. It exhibits that the implemented virtual admittance can regulate the reactive power injection for each phase according to its voltage magnitude. Therefore, the unbalance in grid voltage can be naturally compensated. It is worth noting that this feature of unbalanced voltage support cannot be achieved by a conventional outer *Q-V* droop controller. Moreover, if a selective admittance for negative sequence is implemented, as presented in the Chapter 3, the level of unbalance can be further diminished.

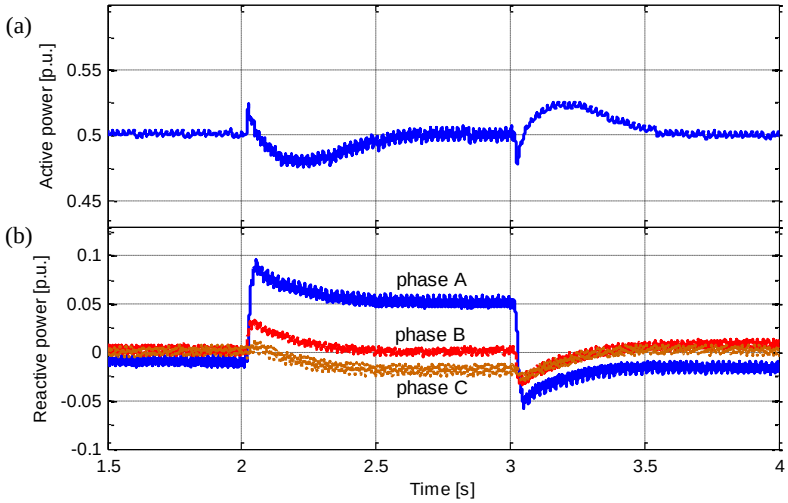

Fig. 4.33. Experimental result analysis of the PI-based power loop controller under an unbalanced voltage dip: (a) active power injected by the converter, and (b) reactive power in each phase injected by the converter.

4.7 Summary of the Chapter

This chapter has presented a power loop controller, namely, the CND controller, for the SPC with adjustable inertia, damping and flexible droop characteristics for grid-connected power converters. The inherent *P-f* droop characteristic shown by typical swing-equation-emulation controllers, referred as the MPL controllers, has been analyzed. Based on this analysis, a constraint between the damping and the inherent *P-f* droop characteristics was identified. For a MPL controller, it is necessary to compensate the droop characteristic to meet the TSO requirements, when a damping parameter is set. In comparison, the CND controller shows more flexibility, since it avoids this constraint between the damping and the inherent *P-f* droop characteristic in the power regulation loop. Therefore, the CND controller does not need any outer *P-f* droop loop. Besides, accurate reference power tracking can also be easily achieved in presence of grid frequency variations.

Simulation and experimental results have verified the CND controller, which let the power converter present a good transient response, same as the one expected from a transfer

function analysis. The performance of the power converter in frequency sweep tests, when the converter is tuned by different sets of parameters, has validated the inertial and droop characteristics of the CND controller. Accurate inertia constant, damping factor and droop gain can be implemented to ensure proper grid-interaction dynamics and also compliance with the TSO requirements. The power converter based on the CND controller was also able to supply an islanded grid and achieved proportional load sharing according to the power converter rating. A comparison between the CND and the MPL controller, showed the significant difference in droop characteristic, and the capability of the CND controller for setting the inherent *P-f* droop gain.

As an alternative, the PI-based power loop controller was also presented in this chapter. It has two control parameters, like the MPL controller, but does not contain any inherent *P-f* droop gain. Therefore, a zero steady-state error in reference power tracking can be achieved regardless of the grid frequency changes. The PI-based power loop controller was also validated in experiments, in terms of reference power tracking, grid frequency changes, droop control and voltage dips response.

Three types of power loop controller for the SPC, namely, the MPL, CND, and PI, were analytically compared with each other. All the three types of controllers are able to provide synthetic inertia, damping and droop characteristics, which are interesting features for the future renewable power generation plants.

Some experimental results to compare the CND-based SPC and a conventional power converter controller were shown in this chapter. Compared with a power converter based on a conventional control, which consists of the VCC, PLL, and IARC, the SPC-based power converter presented an inertial response under power reference changes and grid frequency changes. This inertial response demonstrated that the SPC managed to reshape the interaction dynamics between a generation unit and the grid, contributing to the grid stability by adding inertia to the whole system. In steady state, the active and reactive power control of both strategies were accurate. The synchronized frequency generated by the SPC was more damped compared to the one generated by a PLL, which guarantees a more stable operation of the generation units. Regarding transient performance in presence of grid frequency variations, a SPC-based power converter showed a stronger effect aiming to compensate grid frequency disturbances than a conventional power converter. The amount of the active power transient change processed by the power converter, under grid frequency variations, can be increased simply by increasing the inertia constant. Therefore, in case of large-scale integration of the SPC-based power converters, this active power transient response will resist the grid frequency deviation. On the other hand, in case of small-scale integration, the transient active power response of the SPC-based power converters will not do any harm. Even though a conventionally controlled power converter can also compensate grid frequency disturbances based on droop control, the lacking of inertia renders the grid frequency more prone to disturbances. In presence of grid voltage sags, the SPC-based power converter naturally supported the voltage by injecting reactive current to the grid, thanks to the effect of its virtual admittance.

CHAPTER 5.

Unified Reference Controller

The Unified Reference Controller (URC) for VSCs in multi terminal direct current (MTDC) systems is presented in this chapter. MTDC grids are expected to experience rapid expansion in the near future as they have emerged as a competitive solution for transmitting offshore wind power and overlaying ac areas. The goal for developing the URC is to endow the VSCs in MTDC grids with ac grid support characteristic, especially providing frequency droop control for the connected ac areas. The control objectives of the VSCs are no longer limited to the stabilization of MTDC grid, instead, the requirements of ac side are also met. This chapter also introduces the concept of inertia sharing for the control and operation of MTDC grids, which can be achieved by the proposed URC.

5.1 Introduction

In recent years, HVDC transmission systems based on VSCs have emerged as a promising technology due to their technical and economic advantages [106]–[110]. Particularly, VSC appears as a suitable technology for Multi-Terminal dc (MTDC) systems [111]. The developments of VSC-based MTDC can be found in [112]–[114].

Master/Slave control is one of the control paradigms for MTDC systems, where one of the grid-side VSC stations performs dc voltage control, and other stations perform power flow control [115]. As a step towards the autonomous operation and let multiple VSC stations participate in dc voltage control of the grid, voltage-squared control is proposed in [116]. Another simple implementation to let each VSC contribute to the total energy balance of the MTDC grid is the voltage-current (voltage-power) droop control [115], [117].

The abovementioned methods can keep the balance between the harvested and the delivered energy by regulating the dc voltage in MTDC grid. However, the VSC stations have not response to the change of the ac grid frequency. In one sense, it can be seen as an advantage since the dynamics of different ac areas are decoupled from each other and the propagation of perturbations from one ac area to another can hence be avoided. In another sense, the lack of frequency support to ac areas becomes a drawback. Actually, for VSC stations connected to low-inertia ac grids, frequency support is an essential feature to improve system stability [38], [118], [119]. A secondary control architecture for MTDC

grids incorporating load frequency control is proposed in [120], thus the power reference of VSCs can be set taking into account the ac grid frequency. The frequency support can also be achieved by specifying the primary control as shown in [121]. In this section, frequency support is considered in designing the primary control. By configuring the VSCs in MTDC grids in proper control modes, a large ac grid can share its inertia with other ac areas, especially supporting the frequency of a low-inertia grid.

Different control modes such as voltage control, power control and droop control can be employed for each VSC station according to the status of the MTDC grid that it interfaces with. For example, the stations interfacing with wind farms normally perform power and frequency control for harvesting the maximum energy, and the station that is connected to a stiff bus of the ac grid can perform voltage control [115]. The transition among different control modes can facilitate a more flexible operation of MTDC grids. For instance, when an onshore VSC station has a fault and is blocked, another onshore VSC station needs to take more share in dc voltage control following the dispatch of the secondary control, then the control mode of this VSC station may need to change from voltage droop control to voltage control. After this transition, the MTDC grid can hold on for longer time before the fault station is restored, thanks to a more optimized power flow configuration. A Generalized Voltage Droop (GVD) control structure is proposed in [122] for multiple control modes of VSC and the mode transition. Based on the secondary control commands, the parameters of the GVD controller can be scheduled for smooth mode transition. Nevertheless, the method proposed in [122] has not options for the support of ac grid frequency.

This section presents a Unified Reference Controller (URC) for primary control of MTDC grids as a step towards more flexible operation. Oriented to the requirements of ac systems, the frequency droop mode and frequency-voltage double droop mode are integrated in the generalized primary controller that is capable of operation mode transition. It is worth to remark here that not only dc voltage stabilization, but also ac frequency support stands as the main feature of the controller presented in this chapter. In this way, MTDC grid starts to interact with the ac system and contributes to the stabilization of an ac area by sharing the inertia among different ac areas. Besides, the dynamics interaction among different ac areas and the dc grid are analyzed to avoid negative impacts.

5.2 Different Operation Modes for VSCs in an MTDC Grid

Fig. 5.1 shows the hierarchical control structure of a VSC station, which mainly includes the droop based primary and power flow based secondary control. The droop based primary control is achieved by using the URC. The secondary control determines the appropriate operation mode and set points for the VSC stations periodically based on an optimal power flow program, and the URC executes the orders of the secondary control.

The most adopted operation modes for VSCs in HVDC systems are dc voltage control, frequency control, and voltage droop control. Offshore VSC stations can deliver power to the dc system following the wind status, by performing frequency or maximum power point

control, while onshore stations commonly work in voltage control mode or voltage droop mode for balancing power in the dc systems. In this manner the wind generation and dc transmission systems act as feeder of the ac systems, while has not response to ac grid frequency changes. This feature has been seen as an advantage so far, since it allows isolating any fault or perturbation coming from the ac system, thus avoiding complication or instability in the whole ac-dc network.

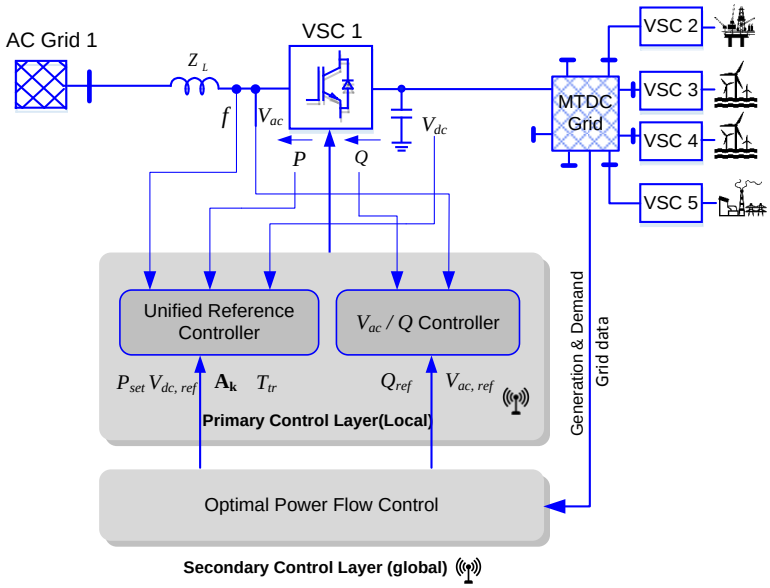

Fig. 5.1. VSC station hierarchical control structure.

However, ancillary services for both ac and dc grids are expected nowadays for improving the grid performance [123], and support to ac grid frequency is becoming necessary, especially in cases when MTDC systems are integrated into ac power systems in a large scale or when the connected ac grid has low inertia. Therefore, control modes considering ac frequency support are required, and in the meantime the interaction dynamics among multiple nodes needs to be analyzed to avoid the negative impacts of the frequency droop and voltage droop. In general, the operational modes of VSC stations considering not only dc requirements, but also the ones set by the ac grid, are listed below.

A. Frequency / Power Control

Because of the grid forming ability of the VSC, islands such as wind farms and oil or gas platforms can be connected to VSC-based MTDC networks without auxiliary equipment [124]. For doing this the associated VSCs (like VSC 3 and 4 in Fig. 5.1) will perform frequency and power control and set the load frequency. In addition, if the VSC bears a dominant share of the generation for the connected island ac grid, it also needs to perform frequency control.

B. P-V_{dc} Droop Control

In this operation mode, the VSC exerts active power control, while the power order is determined by the power flow program and adjusted by the droop control algorithm. This mode is applicable to onshore VSC stations like VSC 1 and 5 in Fig. 5.1.

Compared to the fixed active power control, the operation with droop characteristics is critical for the stabilization of the MTDC grid by adjusting the power delivery as a function of the actual dc link voltage. The droop slope can be specified considering the steady-state voltage range of the dc grid and the power processing constraints applied to each VSC [115].

C. DC Voltage Control

The VSC operating in this mode performs fixed dc voltage control. Commonly a VSC connected to a large ac grid works in this control mode to take as much share as possible in holding the power balance within the MTDC grid. The dc link voltage is regulated to a given value under the assumption that the VSC can always balance the imported/exported power in the dc grid by adjusting its power exchange with the ac grid. However, this assumption cannot always be fulfilled considering the limited capacity of the VSC stations. In practice, a power or dc current limitation has to be implemented in the VSC station controller to saturate power delivery under severe faults [125]–[127].

D. P-f Droop Control

This mode is as an alternative to the P-V_{dc} droop operation. This is oriented to a scenario in which the ac grid where the VSC is connected to has insufficient inertia, whereas the VSC is also connected to a strong node in the MTDC grid. In this mode, the main attention is payed to ac side, being the VSC deemed to be a generation unit with not only grid feeding capabilities, but also grid supporting features. The VSC 2 in Fig. 5.1 can preferably work in this control mode, considering the insufficient inertia of the oil and gas platform.

E. V_{dc}-f Interaction Control

In the grid of the future, when MTDC systems are largely penetrated into the ac mains, the regulation of both dc voltage and ac frequency shall be considered in the design of primary or secondary control layers. In order to head towards automation, the primary control of VSC with automatic responses to both dc voltage and ac frequency variations could be of interests. A voltage-frequency double droop control mode is considered in the controller presented in this chapter. The future onshore VSC stations (like VSC 1 and 5 in Fig. 5.1) can work in this mode for supporting the ac system, as well as stabilizing the dc system. Besides, the sharing between dc support and ac support can be adjusted simply by scheduling the control parameters.

5.3 Unified Reference Controller

With the capability of selecting the operation mode of VSCs, the grid of future will manage to automatically adapt itself to the perturbations in primary sources and loads, and even get through the fault contingencies. For instance, when a VSC station needs to contribute more in the voltage control after the fault of another VSC station, it can change

from the voltage droop control to voltage control operation mode. Fig. 5.2 shows the primary control architecture of such VSC, which is mainly characterized by the URC.

This control architecture is proposed as a unified approach for controlling VSCs in MTDC grids. The control layers shown in Fig. 5.2(a) are similar to the typical control scheme of VSC-HVDC, which consists of an inner current controller and several outer controllers. The reference of the current in d axis (i_d^{ref}) is determined by the URC, which is dependent on the local measurements and the secondary commands. The reference of the current in q axis (i_q^{ref}) is determined by either the reactive power controller or the ac voltage controller.

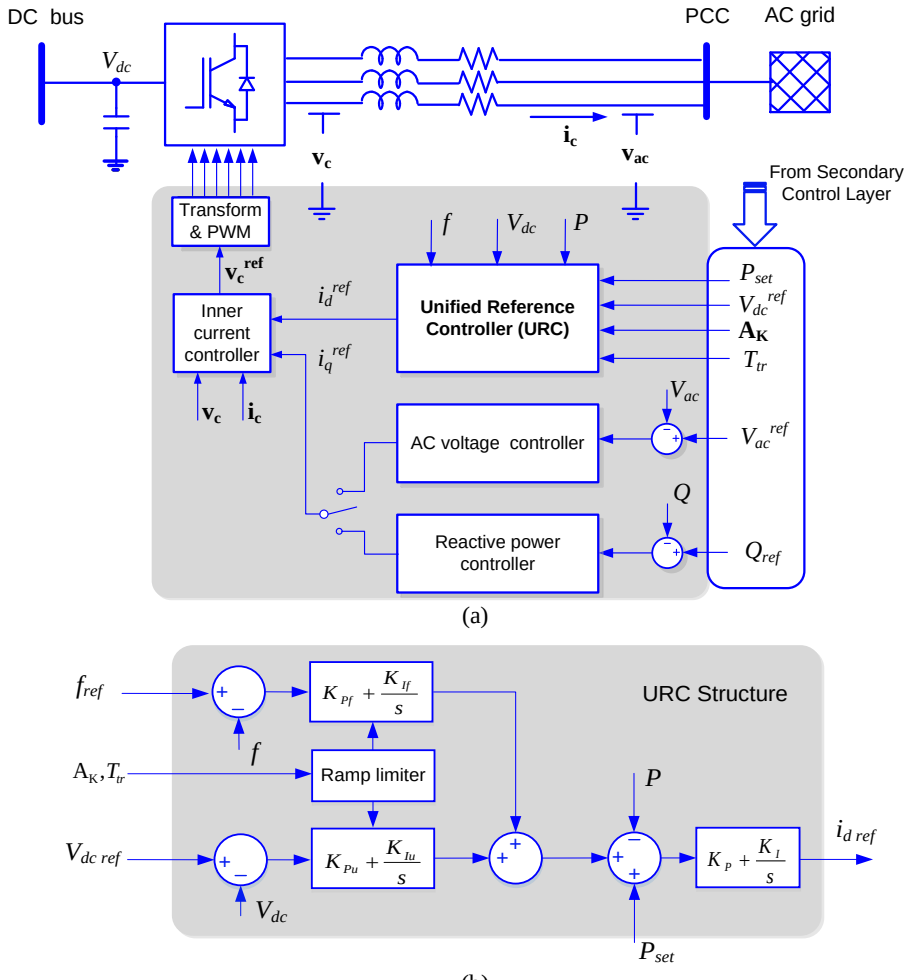

Fig. 5.2. VSC stations control: (a) general control structure, and (b) the proposed Unified Reference Controller.

The structure of the URC is shown in detail in Fig. 5.2(b). P_{set} is the active power reference resulting from a power flow analysis, and $\mathbf{A_K}$ is the parameter matrix shown in (5.1). Each element of $\mathbf{A_K}$ is defined in Fig. 5.2(b).

$$\mathbf{A_K} = \begin{bmatrix} K_{Pf} & K_{If} \\ K_{Pu} & K_{Iu} \end{bmatrix} \tag{5.1}$$

The matrix $\mathbf{A_K}$ will always contain some zero element to avoid control fighting, and it will be set by the secondary control layer commands. With different configuration in $\mathbf{A_K}$, the URC performs different functions, thus assigns the required operation mode to the controlled VSC. For operation modes like V_{dc} control or f control, P_{set} needs to be set to zero. The secondary control also specifies the transition time, T_{tr}, and the gain scheduling block will ramp $\mathbf{A_K}$ to the control objective during the transition time.

Except for the reference power control, other operation modes can be selected and are generalized as follow:

Mode A: f control: $K_{Pf} \neq 0$, $K_{If} \neq 0$, $K_{Pu} = 0$, $K_{Iu} = 0$.

$$P_{ref} = (K_{Pf} + \frac{K_{If}}{s})(f_{ref} - f)\cdot \tag{5.2}$$

Mode B: P-V_{dc} droop control: $K_{Pf} = 0$, $K_{If} = 0$, $K_{Pu} \neq 0$, $K_{Iu} = 0$.

$$P_{ref} = P_{set} + K_{Pu}(V_{dc} - V_{dc}^{ref})\,. \tag{5.3}$$

Mode C: V_{dc} control: $K_{Pf} = 0$, $K_{If} = 0$, $K_{Pu} \neq 0$, $K_{Iu} \neq 0$.

$$P_{ref} = (K_{Pu} + \frac{K_{Iu}}{s})(V_{dc} - V_{dc}^{ref})\,. \tag{5.4}$$

Mode D: P-f droop control: $K_{Pf} \neq 0$, $K_{If} = 0$, $K_{Pu} = 0$, $K_{Iu} = 0$.

$$P_{ref} = P_{set} + K_{Pf}(f_{ref} - f)\,. \tag{5.5}$$

Mode E: V_{dc}-f control: $K_{Pf} \neq 0$, $K_{If} = 0$, $K_{Pu} \neq 0$, $K_{Iu} = 0$.

$$P_{ref} = P_{set} + K_{Pf}(f_{ref} - f) + K_{Pu}(V_{dc} - V_{dc}^{ref})\,. \tag{5.6}$$

As a traditional discipline, the HVDC system simply plays a role as a feeder for the ac grids, and only stabilization of the dc side is considered. Based on the URC, when modes A, D or E are activated, perturbations at the ac side will be compensated as well. However, the ac perturbations will affect the dc link voltage, and in turn the frequencies of other ac areas. Because of this coupling dynamics, the strength of different areas can be shared to damp the disturbances in the whole network, while on the other hand the perturbations

might also be propagated and even amplified and cause instability. The latter situation has to be avoided through a proper control design.

Based on the URC strategy, the interaction between the dc and ac grid is modeled in Fig. 5.3, where two ac systems are interconnected through a dc grid, with two VSCs acting as interfaces.

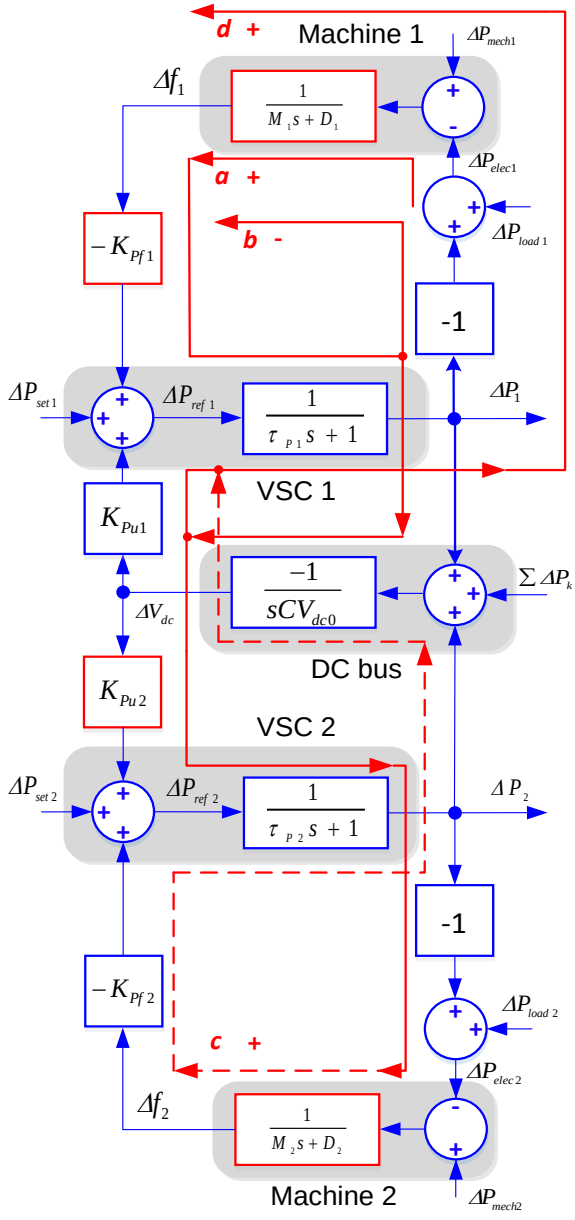

Fig. 5.3. The interaction between dc voltage and ac frequency.

The ac system is represented by the swing equation of synchronous machine, where the electrical power equals to the load power subtracting the power injected by the converter. The dynamics of the power converter is represented by a first-order time delay, and the dynamics of the dc grid is determined by the equivalent capacitance of the dc capacitors.

The following analysis is an example to show how the highlighted droop parameters K_{pf1} and K_{pu2} should be determined considering the dynamics of the relevant ac systems, which are expressed in the highlighted blocks for the Machine 1 and 2. Arrows in the Fig. 5.3 denote the disturbance flow directions considered in the following analysis. The symbols ¨a¨, ¨b¨, ¨c¨ and ¨d¨ represent different effects in presence of disturbances, which are explained in detail in the following analysis.

In Fig. 5.3, τ_{Pi} is the time constant of the power control loop of the i^{th} VSC, ΔP_i the incremental power that is injected to the i^{th} ac grid, ΔP_{loadi} the incremental load changes in the i^{th} ac grid, M_i and D_i respectively are the torque and damping parameters of the synchronous machine that forms the i^{th} ac grid, $\sum \Delta P_k$ the sum of the power that is injected to other ac grids except for grids 1 and 2, and C the equivalent dc link capacitance.

As shown in Fig. 5.3, the system is a multi-input multi-output system. The power delivered by the VSCs is influenced by different inputs. During the operation of MTDC grid, the variation in dc voltage can happen due to the events such as the variation in the harvested wind power and the variation in the power delivered to the ac grids. In order to study the VSC power delivery response under variations in the dc voltage, the transfer function considering the partial derivation $\partial P_i/\partial V_{dc}$ needs to be obtained. By defining the dc voltage as an independent variable and the power delivered to grid i (1, 2, …) as a dependent magnitude, a transfer function can be written as:

$$\Delta P_i = \frac{K_{Pui}(M_i s + D_i)}{M_i \tau_{Pi} s^2 + (M_i + \tau_{Pi})s + D_i + K_{Pfi}} \Delta V_{dc} \cdot \tag{5.7}$$

As shown in (5.7), the power processed by the VSCs is able to compensate the deviation of dc voltage. Such compensation effect is strengthened when K_{Pu} takes high values and K_{Pf} low values.

On the other hand, a variation in the ac grid frequency can happen because of ac load changes and generation variation. In such a case, the response of ΔP_i in the presence of frequency changes can be written as:

$$\Delta P_i = \frac{-K_{Pfi} C V_{dc0} s}{\tau_{Pi} C V_{dc0} s^2 + C V_{dc0} s + K_{Pui}} \Delta f_i \cdot \tag{5.8}$$

As shown in (5.8), the power processed by the i^{th} VSC aims to compensate the deviation of the ac frequency during transient states. Moreover, this compensation effect will not only respond to transient in the VSC local area, but it will also respond to transients in other areas, which are coupled through ΔP_2 and $\sum \Delta P_k$.

As shown in Fig. 5.3, frequency variations from an ac grid can be propagated to other ac grids by affecting the dc voltage. The frequency response of an ac grid in presence of dc voltage changes can be written as:

$$\Delta f_i = \frac{K_{Pui}}{M_i \tau_{Pi} s^2 + (M_i + \tau_{Pi}) s + D_i + K_{Pfi}} \Delta V_{dc} \cdot \tag{5.9}$$

Then, the interaction between two ac areas can be analyzed. In a conventional control paradigm, a VSC station does not respond to frequency variations, and the frequency hence swings freely following the load changes and is characterized by the inertia constant of the generation plant. This effect is denoted by "*a*" in Fig. 5.3. So if the demand P_{load1} decreases in the area 1, the frequency in such area, f_1, increases according to this effect. However, in cases of activating modes A, D or E, K_{pf1} is enabled, and the effect "*a*" will be superposed by a feedback effect, which is denoted by "*b*" in Fig. 5.3, which counteracts and damps the frequency variation. Due to the decrease in the delivered power P_1, the dc voltage increases, and the frequency of another ac area, f_2, can be disturbed if K_{Pu2} is enabled and if the inertia in such second area, M_2, is insufficient. This effect is denoted by "*c*" in Fig. 5.3. Moreover, if K_{Pf2} and K_{Pu1} are enabled, the effect "*d*" will take place to counteract the effect "*b*". Therefore, the frequency response in the first area, f_1, will results from the aggregated effects of "*a*", "*b*" and "*d*".

As a healthy interaction among multi terminals, the effects "*c*" and "*d*" need to be avoided, which can be achieved under either of two conditions: sufficient inertia of area 2, or enough small value of K_{Pu2}. In the former condition, the disturbances in grid 1 will sink in grid 2 due to the inertia of grid 2, showing the effect of inertia sharing. In the latter condition, the disturbances in grid 1 will not propagate to grid 2, despite the fact that grid 2 could have insufficient inertia.

In general, the conceptual operation paradigm for MTDC grids is shown in Fig. 5.4, where five different ac areas are interconnected through a MTDC grid.

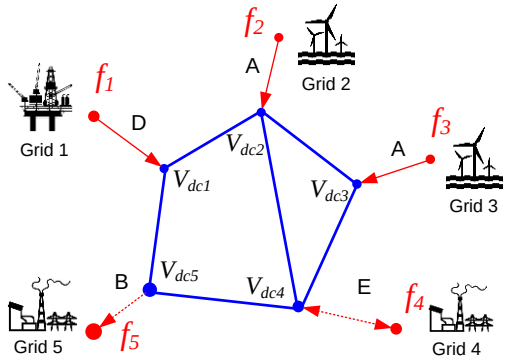

Fig. 5.4. The conceptual operation paradigm for MTDC grid based on ac-dc interaction.

Grid 1 is an oil and gas platform as a low-inertia ac grid, Grid 2 and 3 are offshore wind farms, Grid 4 is an onshore grid with clusters of synchronous machines, and Grid 5 is similar to Grid 4 but with larger rotating mass. According to the different characteristics of each ac

grid, different operation modes for the VSC controllers interconnected through the MTCD networks should be selected. In detail, the offshore farms will work with frequency control (Mode A), the Grid 5 performs voltage droop control (Mode B), the oil and gas platform performs frequency droop control (Mode D), and the Grid 4 performs V_{dc}-f interaction (Mode E).

The arrows in Fig. 5.4 denote the direction of the disturbance flow (which not necessarily matches the direction of the power flow). In this way the frequency disturbances in grids 1, 2 and 3 can sink in grids 4 and 5, and the disturbances in grid 4 can also be damped by grid 5. It can be seen that by operating in a proper mode, the nodes connected to low-inertia ac grids will not be involved in dc voltage control, but only in supporting the ac frequency. On the other hand, a VSC station connected to a large ac grid can perform dc voltage control. Moreover, other stations can perform frequency support as well as voltage support following both needs at the dc and ac sides.

The advantages of the inertia sharing can be summarized as:

1- Frequency support for an ac area by exchanging power with another ac area that has larger amount of inertia.
2- Isolation of the perturbations at the dc side because of frequency deviation in a low-inertia ac grid.
3- Adjustable interaction between the dc voltage and ac frequency at each terminal.

5.4 Simulation Results

A simulated MTDC grid based on CIGRE B4 grid [128] is built as shown in Fig. 5.5, where two offshore grids and two onshore grids are interconnected by five VSC stations. The proposed URC is implemented for each VSC.

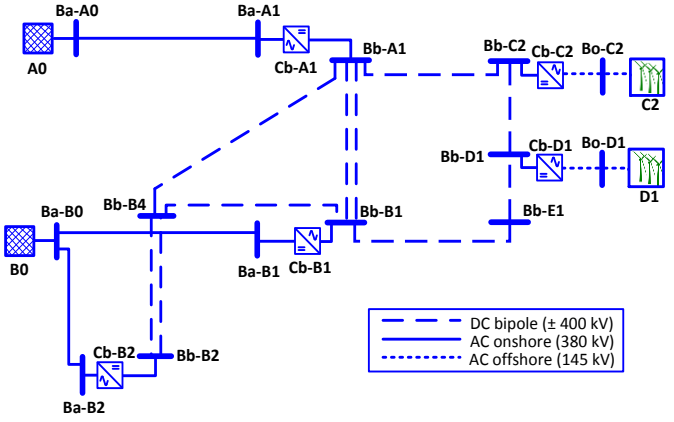

Fig. 5.5. CIGRE MTDC grid test system.

The grid B0 is configured to be a strong ac grid with high amount of inertia, which leads to a stiff frequency. For the sake of simplifying the grid model, a Thevenin equivalent model

(voltage source with impedance) is used to form the grid B0. The VSC Cb-B1 and Cb-B2 are hence assigned with voltage droop control. The offshore VSC stations, Cb-C2 and Cb-D1, perform frequency control. The VSC Cb-A1 works in different control modes with different control parameters in the following tests. The control parameters of VSC station Cb-A1 are shown in Table 5.1.

In this test, the base power for VSCs and the base voltage for dc buses are 1200 MW and 800 kV, respectively. Two synchronous generators supply the grid A0 with a base power of 400 and 200 MW. They both have an inertia constant of 3.6 s and initially work at 0.72 pu. The events considered in the tests are listed in Table 5.2, and some simulation results are presented in the following to show the interaction between the dc and ac grid.

Table 5.1 Control parameters for the VSC Cb-A1

Symbol	K_{PU}	K_{Pf}	K_{Iu}	K_{If}
$\mathbf{A_{K1}}$	20	0	0	0
$\mathbf{A_{K2}}$	20	0.4	0	0
$\mathbf{A_{K3}}$	20	0.8	0	0
$\mathbf{A_{K4}}$	0	0.4	0	0

Table 5.2 Events in the Tests

Event	Description
E1	Total loss of mechanical power in the 200 MW synchronous generator of grid A0
E2	Load step of 100 MW in the bus Bb-B1
E3	Break of one of the two transmission lines between Ba-A0 and Ba-A1
E4	Transition from the Mode B (voltage droop control) to Mode C (voltage control)
E5	Transition from the Mode E (V_{dc}-f control) to Mode D (frequency control)

Firstly, the event E1 from Table 5.2 is triggered, where a sudden loss of the mechanical power in the 200 MW synchronous generator of grid A0 takes place, and results based on different control parameters are shown in Figs. 5.6 and Fig. 5.7.

Fig. 5.6(a) shows how the other generator of area A0 (400 MW) increases its output power to keep the power equilibrium. Due to the drop of the frequency as Fig. 5.6(d) shows, the VSC also increases its injected power to contribute to the frequency stabilization as Fig. 5.6(c) shows, which is companied by the drop of the dc voltage as Fig. 5.6(b) shows. Comparing the plots in Fig. 5.6(d), it is found that the ac grid supporting effect can be enhanced by increasing the value of K_{Pf}, with the compromise of the dc voltage drop as Fig. 5.6(b) shows.

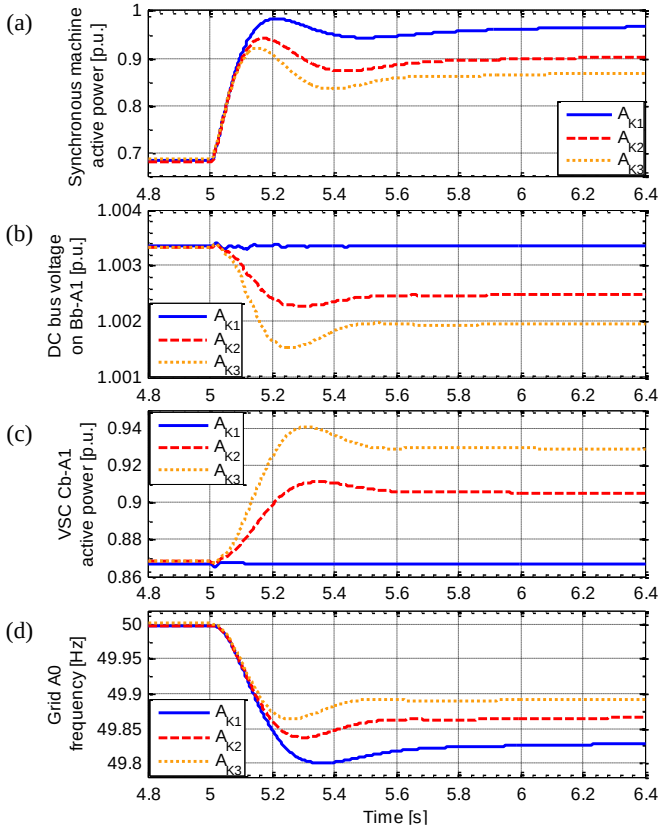

Fig. 5.6. Responses of grid A0 and VSC Cb-A1 when a 200 MW generator in grid A0 is lost: (a) active power output of the remained 400 MW generator in grid A0, (b) dc bus voltage of the VSC Cb-A1, (c) active power injected by VSC Cb-A1 to grid A0, (d) grid A0 frequency.

As shown in Fig. 5.7, the support of grid frequency is actually an aggregated effect of multiple nodes. The dc bus voltage drop results in a change of the power injected by VSC Cb-B1 and Cb-B2, as Fig. 5.7(a) and (b) show, while the VSC Cb-C2 and Cb-D1 maintain their power import following the frequency control, as Fig. 5.7(c) and (d) show.

As a summary of this test, Fig. 5.6(d) shows how the frequency deviation of the ac grid can be alleviated by properly dispatching the control mode and parameters to relevant VSCs, and Fig. 5.7(c) and (d) show how the VSCs that are connected to wind farms are not affected. In this way, the frequency of the grid A0 becomes stiffer, i.e., the grid A0 apparently presents a larger amount of inertia, which actually relies on the dc voltage support of the VSC that is connected to the grid B0. Since the grid B0 has sufficient amount of inertia, its frequency is not much affected by the voltage disturbances. In this case, the grid B0 shares its inertia to the grid A0.

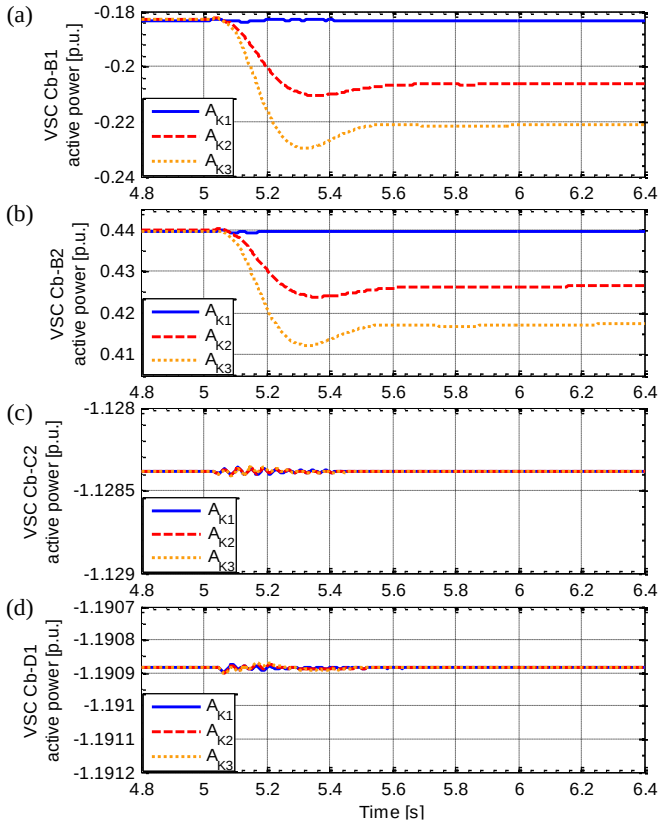

Fig. 5.7. Responses of different terminals when a 200 MW generator in grid A0 is lost: (a) active power absorbed by VSC Cb-B1 from the MTDC grid, (b) active power absorbed by VSC Cb-B2 from the MTDC grid, (c) active power absorbed by VSC Cb-C2 from the MTDC grid, (d) active power absorbed by VSC Cb-D1 from the MTDC grid.

A second test, the event E2 from Table 5.2 is triggered to the system, i.e., a load step of 100 MW in the dc bus Bb-B1 takes place. This event might represent a dc grid perturbations caused by a large change in the power imported from the offshore wind farms or in power injected in one of the onshore terminals. Fig. 5.8 shows the responses of the ac grid A0 and the VSC Cb-A1. By comparing the plots in Fig. 5.8, the effect of K_{Pu} and K_{Pf} can be clearly identified, corresponding to the dc voltage and ac frequency droop support loops. As a consequence of the load increment, the voltage at the dc bus Bb-A1 drops and reaches a new steady state value, as shown in Fig. 5.8(b). As a result, the power injected to the ac grid by the VSC Cb-A1 decreases to compensate the the dc bus voltage drop, as shown in Fig. 5.8(c). Comparing the traces for A_{k2} and A_{k4} in Fig. 5.8(c), it can be appreciated how the trace corresponding to A_{k2} presents a stronger response. Then comparing the traces for A_{k2} and A_{k4} in Fig. 5.8(b), it can be appreciated how the trace for A_{k2} experiences a lower drop. Therefore, it is demonstrated that a greater value for K_{pu} enhances the voltage support effect of the VSC. By following a similar reasoning in comparing the traces for A_{k1} and A_{k2} in Fig. 5.8, it can be concluded that a lower value for K_{pf} enhances the voltage support effect.

Therefore, by specifying different ratios for K_{Pu} over K_{Pf}, the dc voltage droop support and ac frequency droop support can be achieved at different levels.

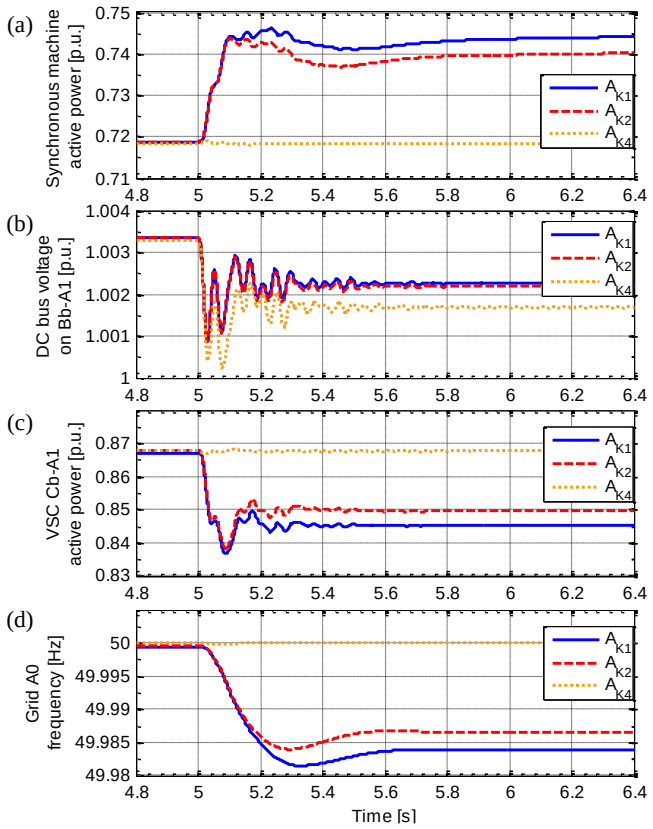

Fig. 5.8. Responses of grid A0 and VSC Cb-A1 when dc load on Bb-B1s steps: (a) active power output of the 400 MW generator in grid A0, (b) dc bus voltage of the VSC Cb-A1, (c) active power injected by VSC Cb-A1 to grid A0, (d) grid A0 frequency.

In summary, load changes in the dc grid or in the ac grid A0 can lead to a change in the dc voltage or the ac frequency. By configuring the associated VSC stations to the appropriate operation modes, with a proper ratio K_{Pu} / K_{Pf}, the perturbations either at ac grid A0 or at dc side can be considerably damped by exchanging power with the VSC stations connected to the ac grid B0. The frequency of the offshore ac grids are not affected, since the wind power import only follows the maximum power point of the offshore plants and do not react to the dc grid voltage changes. The large ac grid B0 acts as the sink of perturbations, thanks to its relatively large amount of inertia.

Fig. 5.9 shows some simulation results when the event E3 from Table 5.2 is considered, i.e., when one of the two paralleled transmission lines between Ba-A0 and Ba-A1 is broken and totally lost. Since the line impedance is instantaneously triggered to a very high value, both the power supplied by the synchronous generator of the grid A0 and the power delivered by the VSC Cb-A1 instantaneously decrease, as Fig. 5.9(a) and (c) show, resulting in a transient in dc voltage and frequency of the grid A0, as Fig. 5.9(b) and (d) show. The

tradeoff between the dc voltage support and ac frequency support is shown in Fig. 5.9 by traces based on different values for K_{Pf}. After comparing such traces, it can be conclude that the larger value for K_{Pf}, the shorter settling time of grid frequency, while the larger deviation of the dc voltage.

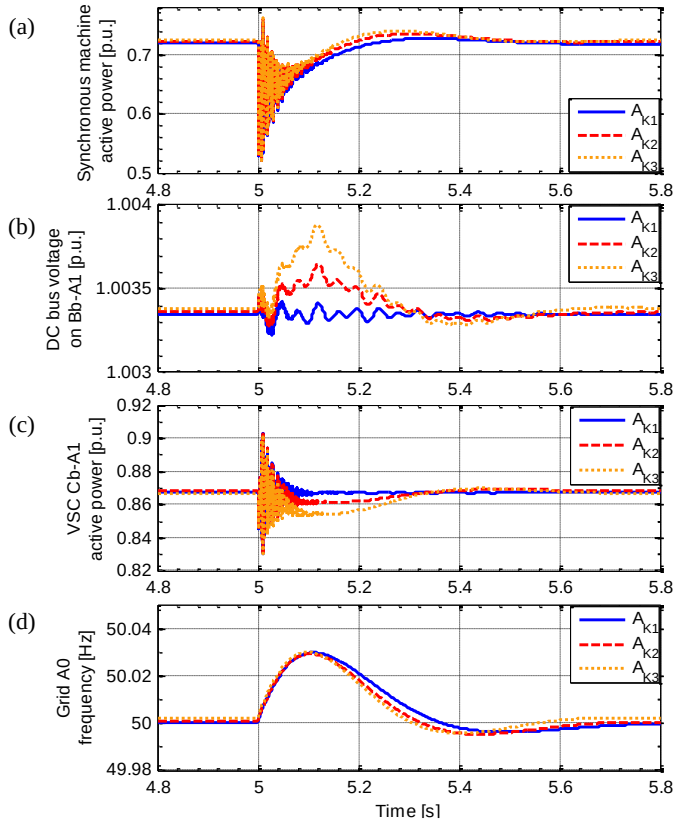

Fig. 5.9. Responses of grid A0 and VSC Cb-A1 when one of the two transmission lines between Ba-A0 and Ba-A1 breaks: (a) active power output of the 400 MW generator in grid A0, (b) dc bus voltage of the VSC Cb-A1, (c) active power injected by VSC Cb-A1 to grid A0, (d) grid A0 frequency.

To show the capability of the URC to have smooth transitions among different operation modes some tests are conducted in the following.

In a first case, the event E4 from Table 5.2 is considered, i.e., the operation mode of VSC Cb-A1 transits from the Mode B (voltage droop control) to Mode C (voltage control). This action might be needed when the VSC station in charge of the dc voltage control is blocked after a fault, and another station hence needs to take more share in dc voltage control.

The transition starts at t = 5 s, and the parameters matrix is linearly ramped to the objective values during 10 s. The dc voltage is driven and attached to its reference value after the transition, as shown in Fig. 5.10(a). A step change in the dc voltage reference is given at t = 25 s, and an effective voltage control is achieved. As it is shown in Fig. 5.10(b), the dc voltage on other nodes (Cb-B1 and Cb-B2) accordingly moves to new operation

points after the change in the operation mode and the change in the voltage reference. When the dc bus voltage of VSC Cb-A1 changes, the power it delivers changes as well. Following the voltage droop control, the active power injected by VSC Cb-B1 and Cb-B2 change to achieve a new power equilibrium, as shown in Fig. 5.10(c).

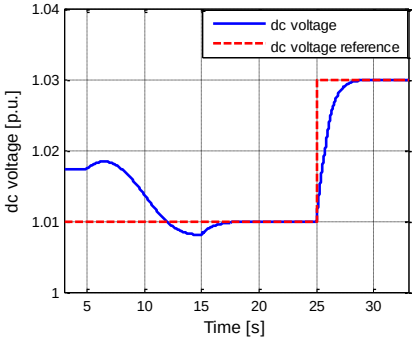

(a)

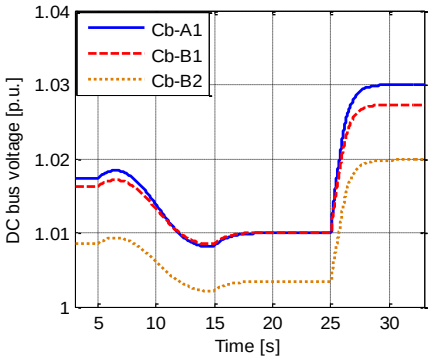

(b)

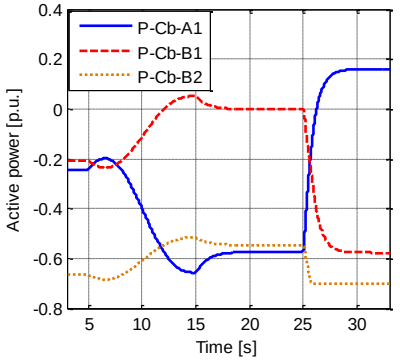

(c)

Fig. 5.10. Control mode for VSC Cb-A1 transition from Mode B to Mode C: (a) dc bus voltage on Bb-A1, (b) dc bus voltage of VSC Cb-A1, Cb-B1 and Cb-B2, (c) active power injected by VSC Cb-A1, Cb-B1 and Cb-B2.

In the second test case, the event E5 from Table 5.2 is executed, i.e., the operation mode of VSC Cb-A1 transits from the Mode E (V_{dc}-f control) to Mode D (frequency control). The transition starts at t = 25 s and reaches the new operation mode in 5 s. By changing the injected active power, the frequency is regulated to its reference value after the transition, as shown in Fig. 5.11(a). The change of the injected power of the VSC Cb-A1 results in the change of the dc voltage, as shown in Fig. 5.11(b). The power injected by the VSC Cb-B1 and Cb-B2 change as well, by following a voltage droop control, as shown in Fig. 5.11(c). At t = 35 s, the load in the grid A0 decreases in a step, and Fig. 5.11(a) shows the transient of the frequency in the grid A0. Thanks to the effective control in mode D, the VSC Cb-A1 compensates the power imbalance by reducing the power injection from 0.5 p.u. to 0.25 p.u., as shown in Fig. 5.11(a), and the frequency is drawn back to its reference after a short transient. From Fig. 5.11(b) and Fig. 5.11(c) it can be observed how the other VSCs automatically move their operation points for restoring the power equilibrium.

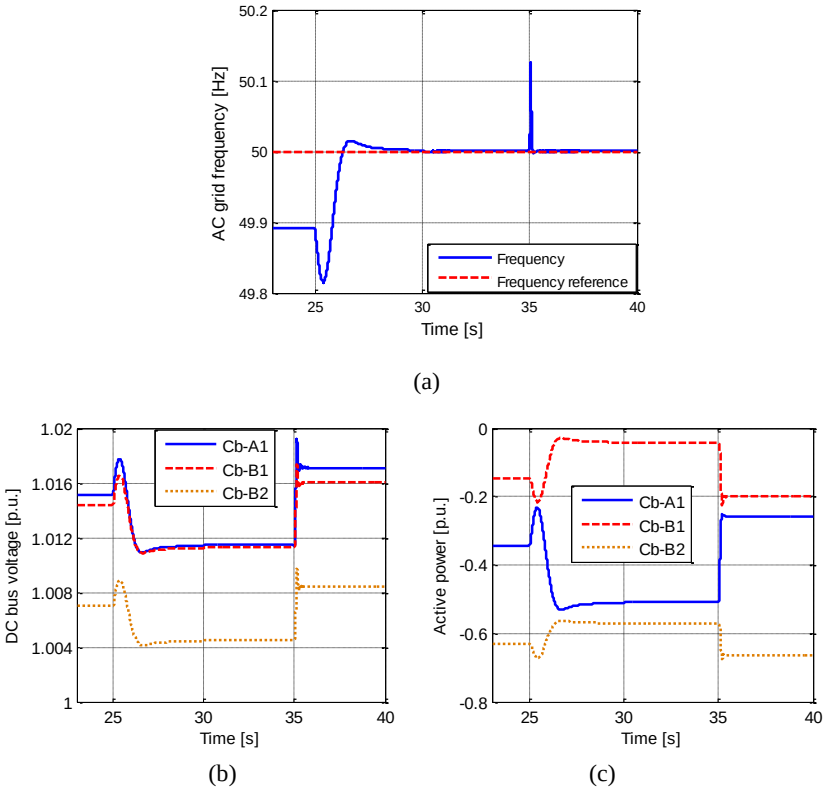

Fig. 5.11. Control mode for VSC Cb-A1 transition from Mode E to Mode D: (a) frequency of the Grid A0, (b) dc bus voltage of VSC Cb-A1, Cb-B1 and Cb-B2, (c) active power injected by VSC Cb-A1, Cb-B1 and Cb-B2.

The results shown in Fig. 5.10 and 5.11 exhibit the effectiveness of the URC structure in re-dispatching the role of the VSC stations interconnected in a MTDC system. Combined with secondary control, each VSC is able to work properly to meet requirements in the associated nodes, and the MTDC grid can also be reorganized after the block of a VSC station.

5.5 Summary of the Chapter

The operation of MTDC grids with inertia sharing was discussed in this chapter, supported by the previously presented URC structure. The perturbations in the ac-dc grids were properly damped by sharing the inertia from several large ac grids, without interfering the low-inertia ac grids. In this way, the requirements of the connected ac grids can also be met, as well as the balance of energy in the MTDC grid. Moreover, the large-scale integration of offshore wind energy based on MTDC grid becomes more possible thanks to its support to the connected ac grids. Simulation results based on the CIGRE B4 grid [128] model showed the good performance and merits of the URC solution. Each VSC station in

the MTDC grid have presented a satisfactory response to events such as load changes in ac grid, load changes in dc grid and transmission line fault.

CHAPTER
6.

Conclusions and Future Work

6.1 Conclusions

The work presented in this PhD dissertation has introduced and analyzed new features in the control of grid connected power converters with grid support functionalities. In this regard, the main work performed in this PhD project has focused on the application of the Synchronous Power Controller (SPC) concept and its fundamental control structure. The results obtained, and the conclusions that can be extracted after the analysis, have evidenced that introducing an emulated and improved synchronous generator characteristics enabled the SPC-controlled power converters to provide an enhanced transient response, which is more aligned with the needs of an electrical system with high integration of non-synchronous based generation devices.

One of the conclusions achieved in this work is that SPC-based power converters can be integrated in already existing power conversion stages, which count on accurate and fast dynamic inner controllers. As these inner controllers are the foundation that should follow the input provided by the SPC, a methodology for achieving an appropriate inner current controller tuning was proposed and tested, giving rise to a methodology that permits to conduct the tuning considering a generic power range of the converter, where the SPC will be hosted.

Different from many other current controller tuning methods, the presented unified tuning approach does not entail a pole-placement process based on a trial-and-error manner, neither the setting of open-loop crossover frequency or phase margin based on a canonical convention. The multiple-candidates-optimal-solution based method has reported satisfactory results, which were collected in the Chapter 3 of this PhD dissertation.

The work conducted in this PhD has contributed also to demonstrate the advantages of the virtual admittance and inertia emulation that the SPC introduces. The SPC structure introduced in Chapter 2 was integrated in the outer loop of a current controlled device, and its performance was tested in different scenarios. The results achieved were satisfactory, especially under transient conditions.

However, a significant active power drift was observed in steady state in some cases. The analysis of this phenomenon permitted to concluded that the inherent *P-f* droop gain can be

high, depending on the SPC implementations. For this reason, a method alternative to the synchronous generator swing equation emulation was introduced. In this case, a PI-based power loop controller came into the plan, which permitted to eliminate the inherent droop as well as to specify the droop characteristic only by means of an external droop loop.

After the analysis conducted, together with the experimental results collected, it has been concluded that the power loop controller that has the lead-lag structure shows more interesting features, such as the capability of specifying the inherent droop slope without interfering the damping and inertia characteristics, and the elimination of the external droop loop. This controller has been referred in this work as the Configurable Natural Droop (CND) controller, and it is integrated in the generic structure of the SPC. All the three power loop control strategies for emulating the inertia and damping of synchronous generators, which are the swing equation emulation, the PI, and the CND, were tested in simulations and experiments, showing good performance. The setup used in the experiments was a 10 kW two-level three-phase grid connected power converter, which showed good performance in presence of power reference changes, grid frequency sweeps and voltage sags, based on different power loop controllers. The CND controller also showed an expected inherent droop feature in the experiments, different from the one resulting from the swing equation emulation. The results of the above tests have been reported in Chapter 4.

The comparison between the SPC and the conventional control was also addressed at this stage, and the results were shown in Chapter 4. It has been demonstrated how the SPC-based power converter can reshape the interaction dynamics between a generation unit and the grid and contribute to frequency stabilization. The active power transient response of the SPC-based power converter showed an inertial response compared to the conventional control based converter, and showed a good steady-state performance like the one from the conventional control. Under frequency changes, the SPC-based power converter showed a stronger transient response aiming to compensate the frequency changes, thanks to the inertial characteristic. Under a voltage sag, the SPC-based power converter naturally injected more reactive power thanks to the virtual admittance. It can be concluded that an SPC-based power converter can contribute more to the grid stability compared to a conventional power converter, which is important in case of large-scale integration of renewable generation, especially power-converter-based generation.

The work conducted in this PhD has been also useful in order to show the importance of negative sequence control. Moreover, it has been shown that this feature can be achieved using the SPC by means of using a simple implementation based on setting different admittances for components in different sequences. This application is of special interest, as it was shown, in case of dealing with asymmetrical grid faults.

The experimental validation of the tri-branch virtual admittance was carried out in this stage, demonstrating the advantages of this structure when dealing with the injection of negative sequence current for unbalanced voltage support. The main principles and the associated results have been reported in Chapter 3.

In the last chapter of the PhD dissertation, a unified outer loop controller for the VSCs in MTDC grids was presented, which integrates both dc voltage and ac frequency droop control. In this way, the support to the ac areas that are connected to the MTDC grid is possible. The simulation results based on a CIGRE B4 test model showed the effectiveness

of the power converter for compensating the frequency changes of the ac area (caused by load changes) that it interfaces, considering the presented control strategy. Besides, the transition from one operation mode to another, such as from voltage droop to voltage-frequency double droop, was also demonstrated to be possible. The work performed in this field was reported in Chapter 5.

6.2 Future Work

As widely admitted, grid connected power converters in the future should provide more services to the grid, support it, and contribute to its stability. Therefore, the SPC will be developed continuously in the future as well as other synchronous generation emulation control (SGEC) strategies.

As indicated in Chapter 1, the SPC is different from other SGEC strategies. Even though this PhD research was more centered on the electromechanical part of the SPC, the use of the virtual admittance is one of the most remarkable features of the SPC. Therefore, future work could be oriented to analyze in deep the advantages brought by the virtual admittance, as well as to propose possible improvements that could be introduced in this part.

Thanks to its virtual implementation, the SPC integrated in highly controllable devices such as power converters are expected to do many things that the synchronous machines cannot, such as having selective admittances or power loop controllers for different frequencies. Even though the tri-branch virtual admittance was introduced in Chapter 3, a systematic and analytical tuning of the negative-sequence admittance, considering both grid requirements and physical current limits is considered as a future work.

In addition to those fields linked to the virtual admittance or power loop controller applications, other issues that have not been totally addressed in this PhD research include the pre-synchronization, re-synchronization and black start for the SGEC-based power converters.

REFERENCES

[1] F. Blaabjerg, R. Teodorescu, M. Liserre, and A. V. Timbus, "Overview of control and grid synchronization for distributed power generation systems," *IEEE Trans. Ind. Electron.*, vol. 53, no. 5, pp. 1398–1409, 2006.

[2] D. G. Holmes, T. A. Lipo, B. P. McGrath, and W. Y. Kong, "Optimized design of stationary frame three phase AC Current regulators," *IEEE Trans. Power Electron.*, vol. 24, no. 11, pp. 2417–2426, 2009.

[3] B. Wen, D. Dong, D. Boroyevich, R. Burogs, P. Mattavelli, and Z. Shen, "Impedance-Based Analysis of Grid-Synchronization Stability for Three-Phase Paralleled Converters," *IEEE Trans. Power Electron.*, vol. 31, no. 1, pp. 26–38, 2015.

[4] S. Buso and P. Mattavelli, *Digital Control in Power Electronics*. Morgan & Claypool, 2006.

[5] H. Akagi, E. Hirokazu, and M. Aredes, *Instantaneous power theory and applications to power conditioning*. John Wiley & Sons, Ltd, 2007.

[6] R. Teodorescu, M. Liserre, and P. Rodriguez, *Grid Converters for Photovoltaic and Wind Power Systems*. John Wiley & Sons, Ltd, 2011.

[7] H. Bevrani, A. Ghosh, and G. Ledwich, "Renewable energy sources and frequency regulation: survey and new perspectives," *IET Renew. Power Gener.*, vol. 4, no. 5, p. 438, 2010.

[8] J. Driesen and K. Visscher, "Virtual synchronous generators," in *IEEE PES General Meeting*, 2008, pp. 1–3.

[9] A. Engler and N. Soultanis, "Droop Control in L^{V}-Grids," in *International Conference on Future Power Systems*, 2005, pp. 1–6.

[10] J. M. Guerrero, J. C. Vasquez, J. Matas, L. G. De Vicuña, and M. Castilla, "Hierarchical control of droop-controlled AC and DC microgrids - A general approach toward standardization," *IEEE Trans. Ind. Electron.*, vol. 58, no. 1, pp. 158–172, 2011.

[11] T. Loix, K. De Brabandere, J. Driesen, and R. Belmans, "A Three-Phase Voltage and Frequency Droop Control Scheme for Parallel Inverters," in *Proc. IECON*, 2007, pp. 1662–1667.

[12] J. Rocabert, A. Luna, F. Blaabjerg, and P. Rodríguez, "Control of Power Converters in AC Microgrids," *IEEE Trans. Power Electron.*, vol. 27, no. 11, pp. 4734–4749, 2012.

[13] K. De Brabandere, B. Bolsens, J. Van Den Keybus, A. Woyte, J. Driesen, and R. Belmans, "A Voltage and Frequency Droop Control Method for Parallel Inverters," *IEEE Trans. Power Electron.*, vol. 22, no. 4, pp. 1107–1115, 2007.

[14] L. Zhang, L. Harnefors, and H. P. Nee, "Power-synchronization control of grid-connected voltage-source converters," *IEEE Trans. Power Syst.*, vol. 25, no. 2, pp. 809–820, 2010.

[15] L. Zhang, L. Harnefors, and H. P. Nee, "Interconnection of two very weak AC systems by VSC-HVDC links using power-synchronization control," *IEEE Trans. Power Syst.*, vol. 26, no. 1, pp. 344–355, 2011.

[16] Entso-E, "ENTSO-E Network Code for Requirements for Grid Connection Applicable to all Generators," 2013.

[17] L. Hadjidemetriou, E. Kyriakides, and F. Blaabjerg, "A new hybrid PLL for interconnecting renewable energy systems to the grid," *IEEE Trans. Ind. Appl.*, vol. 49, no. 6, pp. 2709–2719, 2013.

[18] W. Yao, M. Chen, J. Matas, J. M. Guerrero, and Z. M. Qian, "Design and analysis of the droop control method for parallel inverters considering the impact of the complex impedance on the power sharing," *IEEE Trans. Ind. Electron.*, vol. 58, no. 2, pp. 576–588, 2011.

[19] H. P. Beck and R. Hesse, "Virtual synchronous machine," in *Proc. EPQU*, 2007, pp. 1–6.

[20] T. K. Vrana and C. Hille, "A novel control method for dispersed converters providing dynamic frequency response," *Electr. Eng.*, vol. 93, no. 4, pp. 217–226, 2011.

[21] M. A. Torres, L. A. Lopes, L. A. Moran, and J. R. Espinoza, "Self-Tuning Virtual Synchronous Machine : A Control Strategy for Energy Storage Systems to Support Dynamic Frequency Control," *IEEE Trans. Energy Convers.*, vol. 29, no. 4, pp. 833–840, 2014.

[22] S. I. Nanou, A. G. Papakonstantinou, and S. A. Papathanassiou, "A generic model of two-stage grid-connected PV systems with primary frequency response and inertia emulation," *Electr. Power Syst. Res.*, vol. 127, pp. 186–196, 2015.

[23] J. Zhu, C. D. Booth, G. P. Adam, A. J. Roscoe, and C. G. Bright, "Inertia emulation control strategy for VSC-HVDC transmission systems," *IEEE Trans. Power Syst.*, vol. 28, no. 2, pp. 1277–1287, 2013.

[24] M. P. N. Van Wesenbeeck, S. W. H. De Haan, P. Varela, and K. Visscher, "Grid tied converter with virtual kinetic storage," in *IEEE Bucharest PowerTech*, 2009, pp. 1–7.

[25] F. Gao and M. R. Iravani, "A control strategy for a distributed generation unit in grid-connected and autonomous modes of operation," *IEEE Trans. Power Deliv.*, vol. 23, no. 2, pp. 850–859, 2008.

[26] Q. C. Zhong and G. Weiss, "Static synchronous generators for distributed generation and renewable energy," in *Proc. PSCE*, 2009, pp. 1–6.

[27] Q. C. Zhong and G. Weiss, "Synchronverters: Inverters that mimic synchronous generators," *IEEE Trans. Ind. Electron.*, vol. 58, no. 4, pp. 1259–1267, 2011.

[28] Q. C. Zhong and G. Weiss, "United States Patent Application Publication: Static synchronous generators," 2011.

[29] K. Sakimoto, Y. Miura, and T. Ise, "Stabilization of a power system with a distributed generator by a Virtual Synchronous Generator function," in *ICPE 2011-ECCE Asia*, 2011, pp. 1498–1505.

[30] S. M. Ashabani and Y. A. R. I. Mohamed, "A flexible control strategy for grid-connected and islanded microgrids with enhanced stability using nonlinear microgrid stabilizer," *IEEE Trans. Smart Grid*, vol. 3, no. 3, pp. 1291–1301, 2012.

[31] Y. Du, J. M. Guerrero, L. Chang, J. Su, and M. Mao, "Modeling, analysis, and design of a frequency-droop-based virtual synchronous generator for microgrid applications," in *2013 IEEE ECCE Asia Downunder*, 2013, pp. 643–649.

[32] S. D. Arco and J. A. Suul, "Equivalence of Virtual Synchronous Machines and Frequency-Droops for Converter-Based MicroGrids," *IEEE Trans. Smart Grid*, vol. 5, no. 1, pp. 394–395, 2014.

[33] Q. C. Zhong, P. Nguyen, Z. Ma, and W. Sheng, "Self-Synchronized Synchronverters : Inverters Without a Dedicated Synchronization Unit," *IEEE Trans. Power Electron.*, vol. 29, no. 2, pp. 617–630, 2014.

[34] J. Alipoor, Y. Miura, and T. Ise, "Power System Stabilization Using Virtual Synchronous Generator with Alternating Moment of Inertia," *IEEE J. Emerg. Sel. Top. Power Electron.*, vol. 03, no. 2, pp. 451–458, 2015.

[35] S. Wang, J. Hu, and X. Yuan, "Virtual synchronous control for grid-connected DFIG-based wind turbines," *IEEE J. Emerg. Sel. Top. Power Electron.*, vol. 3, no. 4, pp. 932–944, 2015.

[36] M. Ashabani, F. D. Freijedo, S. Golestan, and J. M. Guerrero, "Inducverters: PLL-less converters with auto-synchronization and emulated inertia capability," *IEEE Trans. Smart Grid*, vol. 7, no. 3, pp. 1660 – 1674, 2016.

[37] S. D'Arco, J. A. Suul, and O. B. Fosso, "Control system tuning and stability analysis of Virtual Synchronous Machines," in *2013 IEEE Energy Conversion Congress and Exposition, ECCE 2013*, 2013, pp. 2664–2671.

[38] M. Guan, W. Pan, J. Zhang, Q. Hao, J. Cheng, and X. Zheng, "Synchronous Generator Emulation Control Strategy for Voltage Source Converter (VSC) Stations," *IEEE Trans. Power Syst.*, vol. 30, no. 6, pp. 3093–3101, 2015.

[39] Y. Chen, R. Hesse, D. Turschner, and H. Beck, "Dynamic Properties of the Virtual Synchronous Machine (VISMA)," *Proc. ICREPQ*, 2011.

[40] Y. Chen, R. Hesse, D. Turschner, and H. Beck, "Comparison of methods for implementing virtual synchronous machine on inverters," in *Proc. ICREPQ*, 2012, pp. 1–6.

[41] P. Rodriguez, J. I. Candela, J. Rocabert, and R. Teodorescu, "Synchronous power controller for a generating system based on static power converters," International Patent WO 2012/117 131 A1, Sept 7, 2012, Priority date: Feb 18, 2011, Licensed by: Abengoa, S.A.

[42] H. Alatrash, A. Mensah, E. Mark, G. Haddad, and J. Enslin, "Generator emulation controls for photovoltaic inverters," *IEEE Trans. Smart Grid*, vol. 3, no. 2, pp. 996–1011, 2012.

[43] P. Rodriguez, I. Candela, and A. Luna, "Control of PV generation systems using the synchronous power controller," in *Proc. ECCE*, 2013, pp. 993–998.

[44] Y. Hirase, K. Abe, K. Sugimoto, and Y. Shindo, "A grid-connected inverter with virtual synchronous generator model of algebraic type," *Electr. Eng. Japan (English Transl. Denki Gakkai Ronbunshi)*, vol. 184, no. 4, pp. 10–21, 2013.

[45] P. M. Anderson and A. A. Fouad, *Power System Control and Stability*. 2002.

[46] D. Remon, A. M. Cantarellas, E. Rakhshani, I. Candela, and P. Rodriguez, "An Active Power Synchronization Control Loop for Grid-Connected Converters," in *IEEE PES General Meeting*, 2014, pp. 1–5.

[47] D. Remon, A. M. Cantarellas, E. Rakhshani, I. Candela, and P. Rodriguez, "An Active Power Self-Synchronizing Controller for Grid-Connected Converters Emulating Inertia," in *ICRERA*, 2014, pp. 424–429.

[48] S. D'Arco, J. A. Suul, and O. B. Fosso, "A Virtual Synchronous Machine implementation for distributed control of power converters in SmartGrids," *Electr. Power Syst. Res.*, vol. 122, pp. 180–197, 2015.

[49] D. Remon, A. M. Cantarellas, M. A. A. Elsaharty, C. Koch-ciobotaru, and P. Rodriguez, “Synchronous PV Support to an Isolated Power System,” in *ECCE*, 2015, pp. 1982–1987.

[50] D. Remon, A. M. Cantarellas, M. A. A. Elsaharty, C. Koch-ciobotaru, and P. Rodriguez, “Equivalent Model of a Synchronous PV Power Plant,” in *ECCE*, 2015, pp. 47–53.

[51] P. Rodriguez, C. Citro, I. Candela, J. Rocabert, and A. Luna, “Flexible Grid Connection and Islanding of SPC- based PV Power Converters,” in *ECCE*, 2015, pp. 450–459.

[52] P. Mitra, L. Zhang, and L. Harnefors, “Offshore Wind Integration to a Weak Grid by VSC-HVDC Links Using Power-Synchronization Control : A Case Study,” *IEEE Trans. Power Deliv.*, vol. 29, no. 1, pp. 453–461, 2014.

[53] H. Mahmood, D. Michaelson, and J. Jiang, “Accurate reactive power sharing in an islanded microgrid using adaptive virtual impedances,” *IEEE Trans. Power Electron.*, vol. 30, no. 3, pp. 1605–1617, 2014.

[54] A. D. Paquette and D. M. Divan, “Virtual Impedance Current Limiting for Inverters in Microgrids With Synchronous Generators,” *IEEE Trans. Ind. Appl.*, vol. 51, no. 2, pp. 1630–1638, 2015.

[55] J. He, Y. W. Li, and M. S. Munir, “A flexible harmonic control approach through voltage-controlled DG-grid interfacing converters,” *IEEE Trans. Ind. Electron.*, vol. 59, no. 1, pp. 444–455, 2012.

[56] X. Wang, F. Blaabjerg, and Z. Chen, “Synthesis of variable harmonic impedance in inverter-interfaced distributed generation unit for harmonic damping throughout a distribution network,” *IEEE Trans. Ind. Appl.*, vol. 48, no. 4, pp. 1407–1417, 2012.

[57] X. Zhang, Q. Zhong, and W. Ming, “Stabilization of a Cascaded DC Converter System via Adding a Virtual Adaptive Parallel Impedance to the Input of the Load Converter,” *IEEE Trans. Power Electron.*, vol. 31, no. 3, pp. 1826–1832, 2016.

[58] M. Albu, K. Visscher, D. Creangă, A. Nechifor, and N. Golovanov, “Storage selection for DG applications containing virtual synchronous generators,” in *2009 IEEE Bucharest PowerTech*, 2009, pp. 1–6.

[59] S. D. Arco and J. A. Suul, “Virtual synchronous machines - Classification of implementations and analysis of equivalence to droop controllers for microgrids,” in *Proc. PowerTech*, 2013, pp. 1–7.

[60] H. Bevrani, T. Ise, and Y. Miura, “Virtual synchronous generators: A survey and new perspectives,” *Int. J. Electr. Power Energy Syst.*, vol. 54, pp. 244–254, 2014.

[61] T. Loix, S. De Breucker, P. Vanassche, J. Van Den Keybus, J. Driesen, and K. Visscher, “Layout and performance of the power electronic converter platform for the VSYNC project,” in *IEEE Bucharest PowerTech*, 2009, pp. 1–8.

[62] K. Visscher and S. W. H. de Haan, “Virtual synchronous machines (VSG’s) for frequency stabilisation in future grids with a significant share of decentralized generation,” in *IET-CIRED*, 2008, no. 0118, pp. 1–4.

[63] R. Hesse, H. Beck, and D. Turschner, “Conditioning Device for Energy Supply Networks,” US8510090B2, 2007.

[64] M. H. J. Bollen, “Characterisation of voltage sags experienced by three-phase adjustable-speed drives,” *IEEE Trans. Power Deliv.*, vol. 12, no. 4, pp. 1666–1671, 1997.

[65] S. Engelhardt, J. Kretschmann, J. Fortmann, F. Shewarega, I. Erlich, and C. Feltes, “Negative sequence control of DFG based wind turbines,” in *IEEE PES General Meeting*, 2011, pp. 1–8.

[66] W. Wang and X. Ma, “Transient analysis of low-voltage ride-through in three-phase grid-connected converter with LCL filter using the nonlinear modal series method,” *Electr. Power Syst. Res.*, vol. 105, pp. 39–50, 2013.

[67] C. Tang, Y. Chen, and Y. Chen, “PV Power System With Multi-Mode Operation and Low-voltage Ride-through Capability,” *IEEE Trans. Ind. Electron.*, vol. 62, no. 12, pp. 7524–7533, 2015.

[68] T. Wijnhoven and G. Deconinck, “Flexible fault current contribution with inverter interfaced distributed generation,” in *IEEE PES General Meeting*, 2013.

[69] P. Rodriguez, A. Luna, M. Ciobotaru, R. Teodorescu, and F. Blaabjerg, “Advanced grid synchronization system for power converters under unbalanced and distorted operating conditions,” in *Proc. IECON*, 2006, no. 2, pp. 5173–5178.

[70] E.ON, “Requirements for Offshore Grid Connections in the E.ON Netz Network,” 2008.

[71] J. A. Fuentes, M. Cañas, A. Molina, E. Gómez, and F. Jiménez, “International Review of Grid Connection Requirements related with Voltage Dips for Wind Farms,” in *International Conference on Renewable Energy and Power Quality (ICREPQ)*, 2007, pp. 1–6.

[72] T. Wijnhoven, T. Neumann, G. Deconinck, and I. Erlich, “Control aspects of the dynamic negative sequence current injection of type 4 wind turbines,” in *IEEE PES General Meeting*, 2014.

[73] J. C. Vasquez, J. M. Guerrero, M. Savaghebi, J. Eloy-garcia, and R. Teodorescu, “Modeling , Analysis , and Design of Parallel Three-Phase Voltage Source Inverters,” *IEEE Trans. Ind. Electron.*, vol. 60, no. 4, pp. 1271–1280, 2013.

[74] M. Ochoa-Gimenez, J. Roldan-Perez, A. Garcia-Cerrada, and J. L. Zamora-Macho, “Space-vector-based controller for current-harmonic suppression with a shunt active power filter,” in *Proc. EPE*, 2013, pp. 1–10.

[75] A. Egea-Alvarez, A. Junyent-Ferre, O. Gomis-Bellmunt, J. L. J. Ekanayake, and N. Jenkins, "Operation and control of VSC-HVDC multiterminal grids for offshore wind," *EPE J.*, vol. 23, no. 2, pp. 34–39, 2013.

[76] S. Fukuda and T. Yoda, "A novel current-tracking method for active filters based on a sinusoidal internal model," *IEEE Trans. Ind. Appl.*, vol. 37, no. 3, pp. 888–895, 2001.

[77] I. J. Gabe, V. F. Montagner, and H. Pinheiro, "Design and implementation of a robust current controller for VSI connected to the grid through an LCL filter," *IEEE Trans. Power Electron.*, vol. 24, no. 6, pp. 1444–1452, 2009.

[78] S. Y. Park, C. L. Chen, J. S. Lai, and S. R. Moon, "Admittance compensation in current loop control for a grid-tie LCL fuel cell inverter," *IEEE Trans. Power Electron.*, vol. 23, no. 4, pp. 1716–1723, 2008.

[79] D. N. Zmood and D. G. Holmes, "Stationary frame current regulation of PWM inverters with zero steady-state error," *IEEE Trans. Power Electron.*, vol. 18, no. 3, pp. 814–822, 2003.

[80] K. Rouzbehi, A. Miranian, A. Luna, and P. Rodriguez, "Optimized control of multi-terminal DC Grids Using particle swarm optimization," *EPE J.*, vol. 24, no. 2, pp. 38–49, 2014.

[81] J. Rocabert, G. M. S. Azevedo, I. Candela, F. Blaabjerg, and P. Rodriguez, "Connection and disconnection transients for micro-grids under unbalance load condition," in *Proc. EPE*, 2011, pp. 1–9.

[82] F. Martinez-Rodrigo, S. de Pablo, and L. C. Herrero-de Lucas, "Current control of a modular multilevel converter for HVDC applications," *Renew. Energy*, vol. 83, pp. 318–331, 2015.

[83] M. Mehrasa, E. Pouresmaeil, B. N. Jørgensen, and J. P. S. Catalão, "A control plan for the stable operation of microgrids during grid-connected and islanded modes," *Electr. Power Syst. Res.*, vol. 129, pp. 10–22, 2015.

[84] R. Teodorescu, F. Blaabjerg, M. Liserre, and P. C. Loh, "Proportional-resonant controllers and filters for grid-connected voltage-source converters," in *Electric Power Applications, IEE Proceedings*, 2006, vol. 153, no. 5, pp. 750–762.

[85] X. Yuan, W. Merk, H. Stemmler, and J. Allmeling, "Stationary-frame generalized integrators for current control of active power filters with zero steady-state error for current harmonics of concern under unbalanced and distorted operating conditions," *IEEE Trans. Ind. Appl.*, vol. 38, no. 2, pp. 523–532, 2002.

[86] P. Rodríguez, A. Luna, I. Candela, R. Mujal, R. Teodorescu, and F. Blaabjerg, "Multiresonant frequency-locked loop for grid synchronization of power converters under distorted grid conditions," *IEEE Trans. Ind. Electron.*, vol. 58, no. 1, pp. 127–138, 2011.

[87] E. Twining and D. G. Holmes, “Grid Current Regulation of a Three-Phase Voltage Source Inverter With an LCL Input Filter,” *IEEE Trans. Power Electron.*, vol. 18, no. 3, pp. 888–895, 2003.

[88] B. Li, W. Yao, L. Hang, and L. M. Tolbert, “Robust proportional resonant regulator for grid-connected voltage source inverter (VSI) using direct pole placement design method,” *IET Power Electron.*, vol. 5, no. 8, p. 1367, 2012.

[89] G. Zeng and T. W. Rasmussen, “Design of current-controller with PR-regulator for LCL-filter based grid-connected converter,” in *PEDG 2010*, 2010, pp. 490–494.

[90] P. Lezana, C. A. Silva, J. Rodríguez, and M. A. Pérez, “Zero-steady-state-error input-current controller for regenerative multilevel converters based on single-phase cells,” *IEEE Trans. Ind. Electron.*, vol. 54, no. 2, pp. 733–740, 2007.

[91] S. Buso and P. Mattavelli, *Digital Control in Power Electronics*, First Edit., vol. 1, no. 1. USA: Morgan & Claypool, 2006.

[92] A. Vidal, F. D. Freijedo, A. G. Yepes, P. Fernández-comesaña, J. Malvar, O. ; Lopez, and J. Doval-Gandoy, “Assessment and Optimization of the Transient Response of Proportional-Resonant Current Controllers for Distributed Power Generation Systems,” *IEEE Trans. Ind. Electron.*, vol. 60, no. 4, pp. 1367–1383, 2013.

[93] S. Lee, K. J. Lee, and D. S. Hyun, “Modeling and control of a grid connected VSI using a delta connected LCL filter,” in *Proc. IECON*, 2008, pp. 833–838.

[94] R. Turner, S. Walton, and R. Duke, “Robust high-performance inverter control using discrete direct-design pole placement,” *IEEE Trans. Ind. Electron.*, vol. 58, no. 1, pp. 348–357, 2011.

[95] A. M. Cantarellas, E. Rakhshani, D. Remon, and P. Rodriguez, “Design of the LCL+trap filter for the two-level VSC installed in a large-scale wave power plant,” in *ECCE*, 2013, pp. 707–712.

[96] J. Xu, J. Yang, J. Ye, Z. Zhang, and A. Shen, “An LTCL Filter for Three-Phase Grid-connected Converters,” *IEEE Trans. Power Electron.*, vol. 29, no. 8, pp. 4322–4338, 2014.

[97] J. M. Espi, J. Castello, R. García-Gil, G. Garcera, and E. Figueres, “An Adaptive Robust Predictive Current Control for Three-Phase Grid-Connected Inverters,” *IEEE Trans. Ind. Electron.*, vol. 58, no. 8, pp. 3537–3546, 2011.

[98] A. G. Yepes, F. D. Freijedo, Ó. López, and J. Doval-Gandoy, “Analysis and design of resonant current controllers for voltage-source converters by means of nyquist diagrams and sensitivity function,” *IEEE Trans. Ind. Electron.*, vol. 58, no. 11, pp. 5231–5250, 2011.

[99] A. G. Yepes, F. D. Freijedo, J. Doval-Gandoy, Ó. López, J. Malvar, and P. Fernandez-Comesaña, “Effects of discretization methods on the performance of

resonant controllers," *IEEE Trans. Power Electron.*, vol. 25, no. 7, pp. 1692–1712, 2010.

[100] S. A. Richter and R. W. De Doncker, "Digital Proportional-Resonant (PR) Control with Anti-Windup Applied to a Voltage-Source Inverter," in *EPE*, 2011.

[101] F. J. Rodríguez, E. Bueno, M. Aredes, L. G. B. Rolim, F. a S. Neves, and M. C. Cavalcanti, "Discrete-time implementation of second order generalized integrators for grid converters," in *Proceedings - 34th Annual Conference of the IEEE Industrial Electronics Society, IECON 2008*, 2008, no. 1, pp. 176–181.

[102] P. Rodríguez, A. Luna, R. S. Muñoz-Aguilar, I. Etxeberria-Otadui, R. Teodorescu, and F. Blaabjerg, "A stationary reference frame grid synchronization system for three-phase grid-connected power converters under adverse grid conditions," *IEEE Trans. Power Electron.*, vol. 27, no. 1, pp. 99–112, 2012.

[103] P. Rodriguez, A. V. Timbus, R. . Teodorescu, M. Liserre, and F. Blaabjerg, "Flexible Active Power Control of Distributed Power Generation Systems During Grid Faults," *IEEE Trans. Ind. Electron.*, vol. 54, no. 5, pp. 2583–2592, 2007.

[104] P. Kundur, *Power system stability and control*. New York, USA: McGraw-Hill, 1994.

[105] J. Duncan Glover, M. S. Sarma, and T. J. Overbye, *Power system analysis and design*, Fourth edi. USA: Cengage Learning, 2010.

[106] F. Schettler, H. Huang, and N. Christl, "HVDC transmission systems using voltage sourced converters design and applications," in *Power Engineering Society Summer Meeting*, 2000, vol. 2, pp. 715–720.

[107] G. P. Adam and B. W. Williams, "Multi-pole voltage source converter HVDC transmission systems," *IET Gener. Transm. Distrib.*, vol. 10, no. 2, pp. 496–507, 2016.

[108] R. Feldman, M. Tomasini, E. Amankwah, J. C. Clare, P. W. Wheeler, D. R. Trainer, and R. S. Whitehouse, "A hybrid modular multilevel voltage source converter for HVDC power transmission," *IEEE Trans. Ind. Appl.*, vol. 49, no. 4, pp. 1577–1588, 2013.

[109] Y. Li, Z. W. Zhang, C. Rehtanz, L. F. Luo, S. Rüberg, and D. C. Yang, "A new voltage source converter-HVDC transmission system based on an inductive filtering method," *IET Gener. Transm. Distrib.*, vol. 5, no. 5, p. 569, 2011.

[110] S. Shariat Torbaghan, M. Gibescu, B. G. Rawn, H. Müller, M. Roggenkamp, and M. van der Meijden, "Investigating the impact of unanticipated market and construction delays on the development of a meshed HVDC grid using dynamic transmission planning," *IET Gener. Transm. Distrib.*, vol. 9, no. 15, pp. 2224–2233, 2015.

[111] D. Van Hertem and M. Ghandhari, “Multi-terminal VSC HVDC for the European supergrid: Obstacles,” *Renew. Sustain. Energy Rev.*, vol. 14, no. 9, pp. 3156–3163, 2010.

[112] U. Axelsson, H. Vatten, C. Liljegren, M. Aberg, K. Eriksson, and O. Tollerz, “The Gotland HVDC Light Project - Experiences from Trial and Commercial Operation,” in *16th International Conference and Exhibition on Electricity Distribution*, 2001, vol. 1, pp. 18–21.

[113] B. S. Gordon, “Supegrid to the rescue,” *Power Eng.*, vol. 20, no. 5, pp. 30–33, 2006.

[114] H. Rao, “Architecture of Nan ’ ao Multi-terminal VSC-HVDC Systems and Its Multi-functional Control,” *CSEE J. Power Energy Syst.*, vol. 1, no. 1, pp. 9–18, 2015.

[115] C. D. Barker and R. Whitehouse, “Autonomous Converter Control in a Multi-terminal HVDC System,” in *9th IET International Conference on ACDC*, 2010, pp. 1–5.

[116] B. Berggren, R. Majumder, C. Sao, and K. Linden, “European Patent Specification: Method and Control Device for Controlling Power Flow Within a Dc Power Transmission Network,” 2010.

[117] J. Liang, T. Jing, O. Gomis-Bellmunt, J. Ekanayake, and N. Jenkins, “Operation and Control of Multiterminal HVDC Transmission for Offshore Wind Farms,” *IEEE Trans. Power Deliv.*, vol. 26, no. 4, pp. 2596–2604, 2011.

[118] J. Zhu, J. M. Guerrero, W. Hung, C. D. Booth, and G. P. Adam, “Generic inertia emulation controller for multi-terminal voltage-source-converter high voltage direct current systems,” *IET Renew. Power Gener.*, vol. 8, no. 7, pp. 740–748, 2014.

[119] B. Silva, C. L. Moreira, L. Seca, Y. Phulpin, and J. a P. Lopes, “Provision of inertial and primary frequency control services using offshore multiterminal HVDC networks,” *IEEE Trans. Sustain. Energy*, vol. 3, no. 4, pp. 800–808, 2012.

[120] A. Marten and D. Westermann, “Load Frequency Control in an interconnected power system with an embedded HVDC Grid,” in *IEEE Power and Energy Society General Meeting*, 2012, pp. 1–7.

[121] T. M. Haileselassie, R. E. Torres-Olguin, T. K. Vrana, K. Uhlen, and T. Undeland, “Main grid frequency support strategy for VSC-HVDC connected wind farms with variable speed wind turbines,” in *IEEE PES PowerTech*, 2011, pp. 1–6.

[122] K. Rouzbehi, A. Miranian, A. Luna, and P. Rodriguez, “A generalized voltage droop strategy for control of multi-terminal DC grids,” *IEEE Trans. Ind. Appl.*, vol. 51, no. 1, pp. 59–64, 2013.

[123] D. Van Hertem and R. H. Renner, “Ancillary services in electric power systems with HVDC grids,” *IET Gener. Transm. Distrib.*, vol. 9, no. 11, pp. 1179–1185, 2015.

[124] T. K. Vrana, R. E. Torres-Olguin, B. Liu, and T. M. Haileselassie, "The North Sea super grid - a technical perspective," in *9th IET International Conference on AC and DC Power Transmission*, 2010, pp. 1–5.

[125] C. Dierckxsens, K. Srivastava, M. Reza, S. Cole, J. Beerten, and R. Belmans, "A Distributed DC Voltage Control Method for VSC MTDC Systems," *Electr. Power Syst. Res.*, vol. 82, no. 1, pp. 54–58, 2012.

[126] L. Xu and L. Yao, "DC voltage control and power dispatch of a multi-terminal HVDC system for integrating large offshore wind farms," *IET Renew. Power Gener.*, vol. 5, no. 3, p. 223, 2011.

[127] T. M. Haileselassie, M. Molinas, and T. Undeland, "Multi-Terminal VSC-HVDC System for Integration of Offshore Wind Farms and Green Electrification of Platforms in the North Sea," in *Proc. NORPIE*, 2008, pp. 1–8.

[128] T. K. Vrana, S. Dennetiere, Y. Yang, J. Jardini, D. Jovcic, and H. Saad, "The CIGRE B4 DC Grid Test System," *Electra*, 2013.

[129] A. M. Cantarellas, E. Rakhshani, D. Remon, A. Luna, and P. Rodriguez, "Grid Connection Design and Control of LCL + Trap Filter Based Two-Level VSC for Wave Power Plant Applications," in *ECCE Asia Downunder*, 2013, pp. 481–486.

APPENDIX

A.

Simulation Test System

The test system used for collecting the simulation results in this PhD dissertation are described in this appendix. The modeling of the LCL-trap filter is also given.

A.1 Simulation Test System

Fig. A.1 shows the block diagram of the simulation test system, which was built in PSIM.

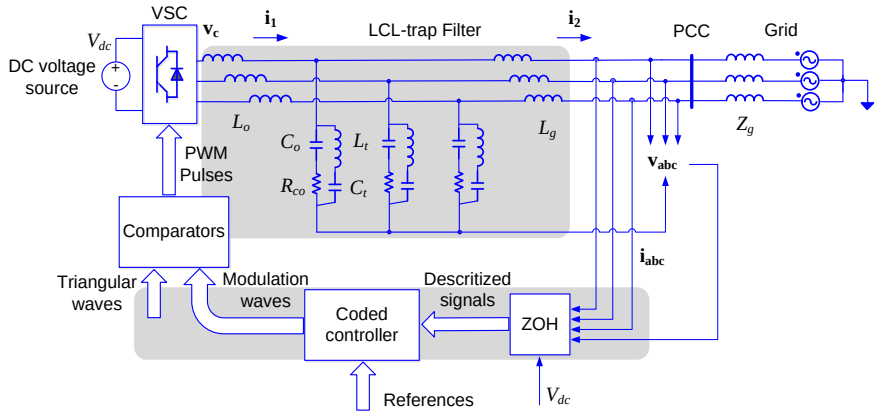

Fig. A.1. Block diagram of the simulation test system used for this PhD dissertation.

This block diagram can represent all the simulation scenarios in this PhD dissertation, except that in the case presented in Section 4.6.1.B, where the converter, filter and controller blocks were reproduced for paralleled working of power converters.

For the scenario of 10 kW grid connected power converter, the parameters are shown in

Table A.1.

Table A.1 Parameters of the 10 kW power converter simulation system

Description	Symbol	Value
nominal grid phase-phase voltage	V_{line}	400 [V]
nominal grid frequency	f_g	50 [Hz]
dc bus voltage	V_{dc}	640 [V]
converter nominal power	P_N	10 [kW]
switching frequency	f_{sw}	10050 [Hz]
samping frequency	f_s	10050 [Hz]
filter converter side inductance	L_o	2.6 [mH]
filter grid side inductance	L_g	662 [μH]
filter capacitance	C_o	5.5 [μF]
filter trap branch capacitance	C_t	1 [μF]
filter trap branch inductance	L_t	244 [μH]
filter converter side resistance	R_o	0.025 [Ω]
filter grid side resistance	R_g	0.094 [Ω]
filter damping resistance	R_{co}	1 [Ω]

For the scenario of 100 kW grid connected power converter, the parameters are shown in Table A.2.

Table A.2 Parameters of the 100 kW power converter simulation system

Description	Symbol	Value
grid phase-phase voltage	V_{line}	400 [V]
grid frequency	f_g	50 [Hz]
dc bus voltage	V_{dc}	750 [V]
converter nominal power	P_N	100 [kW]
switching frequency	f_{sw}	3150 [Hz]
samping frequency	f_s	6300 [Hz]
filter converter side inductance	L_o	778 [μH]
filter grid side inductance	L_g	402 [μH]
filter capacitance	C_o	66 [μF]
filter trap branch capacitance	C_t	30 [μF]
filter trap branch inductance	L_t	85 [μH]
filter converter side resistance	R_o	0.0073 [Ω]
filter grid side resistance	R_g	0.0021 [Ω]
filter damping resistance	R_{co}	0.5 [Ω]

In this simulation system as Fig. A.1 shows, the two-level three-phase VSC is supplied by a dc voltage source, and it is connected to the grid through an LCL-trap filter. This filter was chosen to keep the simulation setup consistent with the experimental one.

The three-phase grid voltage is expressed on the *dq* reference frame, where the *d*-axis voltage is the desired voltage magnitude and the phase-angle is calculated as an integration of the programmed frequency. In this way, the magnitude and frequency of the grid voltages can be changed for balanced voltage sag and frequency sweep tests. For creating an unbalanced voltage sag event, a step voltage source can be placed to multiply the output voltage of the sag phase.

In order to minimize the gap between the simulation and the experimental implementation, the controller is discretized and coded in C language in Microsoft Visual Studio, which generates a DLL file after the code is compiled. A DLL block in PSIM can call the generated DLL file in simulation.

A.2 LCL-Trap Filter Transfer Function

Fig. A.1 has shown the topology of an LCL-trap filter, and in this section its transfer function is presented, which can be used for modeling and analysis. (A.1) [129] shows the single-phase expression of the transfer function between the converter output voltage, $\mathbf{v_c}$, and grid side current, $\mathbf{i_2}$, when an LCL-trap filter is used.

$$G_2(s)=\frac{i_2}{v_c}(s)=\frac{C_oC_tL_tR_{co}s^3+C_tL_ts^2+C_oR_{co}s+1}{\alpha_1 s^5+\alpha_2 s^4+\alpha_3 s^3+\alpha_4 s^2+\alpha_5 s^1+\alpha_6}, \tag{A.1}$$

where L_o and L_g are respectively the converter side inductance and grid side inductance, R_o and R_g respectively the equivalent parasite resistance of the inductors, C_o the main capacitance, R_{co} the passive damping resistance, C_t and L_t the capacitance and inductance of the trap branch, and the different coefficients in the denominator can be written as a function of the filter parameters shown as:

$$\alpha_1 = C_o \cdot C_t \cdot L_o \cdot L_g \cdot L_t, \tag{A.2a}$$

$$\begin{aligned}\alpha_2 = {} & C_o \cdot C_t \cdot L_o \cdot L_g \cdot R_{co} + C_o \cdot C_t \cdot L_o \cdot L_t \cdot R_{co} + \\ & C_o \cdot C_t \cdot L_g \cdot L_t \cdot R_{co} + C_o \cdot C_t \cdot L_o \cdot L_t \cdot R_g + C_o \cdot C_t \cdot L_g \cdot L_t \cdot R_{co}\end{aligned}, \tag{A.2b}$$

$$\begin{aligned}\alpha_3 = {} & C_o \cdot L_o \cdot L_g + C_t \cdot L_o \cdot L_g + C_t \cdot L_o \cdot L_t + C_t \cdot L_g \cdot L_t \\ & + C_o \cdot C_t \cdot L_o \cdot R_g \cdot R_{co} + C_o \cdot C_t \cdot L_g \cdot R_o \cdot R_{co} + C_o \cdot C_t \cdot L_t \cdot R_o \cdot R_{co} \\ & + C_o \cdot C_t \cdot L_t \cdot R_{co} \cdot R_g + C_o \cdot C_t \cdot L_t \cdot R_o \cdot R_g\end{aligned}, \tag{A.2c}$$

$$\alpha_4 = C_o \cdot L_o \cdot R_{co} + C_o \cdot L_g \cdot R_{co} + C_o \cdot L_o \cdot R_g + C_o \cdot L_g \cdot R_o + C_t \cdot L_o \cdot R_g + C_t \cdot L_g \cdot R_o + C_t \cdot L_t \cdot R_o + C_t \cdot L_t \cdot R_g + C_o \cdot C_t \cdot R_g \cdot R_o \cdot R_{co}, \quad \text{(A.2d)}$$

$$\alpha_5 = L_o + L_g + C_o \cdot R_{co} \cdot R_o + C_o \cdot R_{co} \cdot R_g + C_o \cdot R_o \cdot R_g + R_o \cdot C_t \cdot R_g, \quad \text{(A.2e)}$$

$$\alpha_6 = R_o + R_g. \quad \text{(A.2f)}$$

As an alternative, if the converter side current $\mathbf{i_1}$ is controlled, (A.3) becomes useful in modeling and analysis.

$$G_1(s) = \frac{i_1}{v_c}(s) = \frac{1 - G_2(s)(L_g s + R_g)}{L_o s + R_o}. \quad \text{(A.3)}$$

APPENDIX

B.

Laboratory Experimental Setups

This appendix describes the experimental setup of the 10 kW grid connected power converter, and describes the asymmetrical grid fault experimental setup, which consists of two paralleled 100 kW grid connected power converters.

B.1 10 kW Grid Connected Power Converter Setup

Fig. B.1 shows the block diagram of the 10 kW grid connected power converter experimental setup, which was pictured in Fig. B.2 and Fig. B.3.

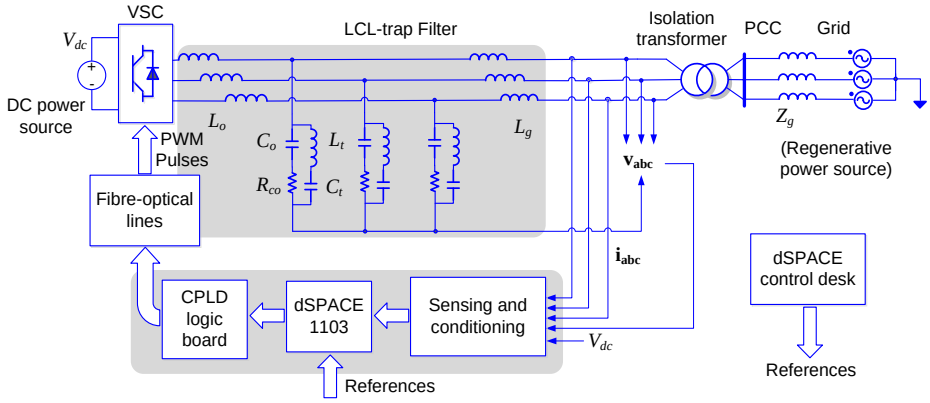

Fig. B.1. Block diagram of the 10 kW grid connected power converter experimental setup.

Fig. B.2. Laboratory view of the 10 kW grid connected power converter test setup.

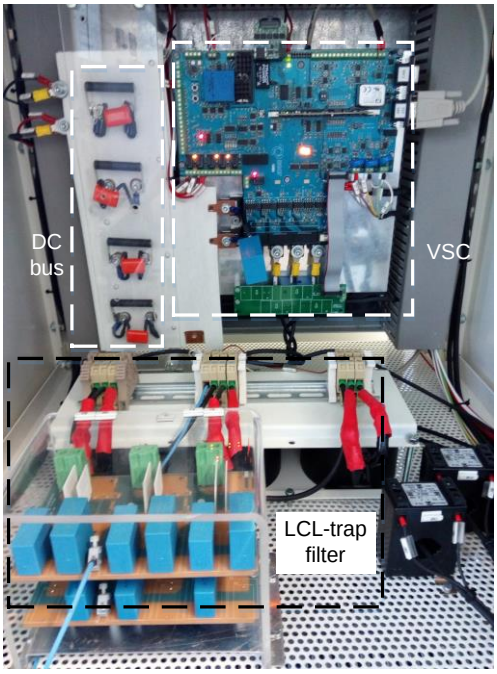

Fig. B.3. 10 kW grid connected power converter.

The setup parameters are listed in Table B.1.

Table B.1 Parameters of the 10 kW grid connected power converter experimental setup

Description	Symbol	Value
nominal grid phase-phase voltage	V_{line}	400 [V]
nominal grid frequency	f_g	50 [Hz]
dc bus voltage	V_{dc}	640 [V]
converter nominal power	P_N	10 [kW]
switching frequency	f_{sw}	10050 [Hz]
samping frequency	f_s	10050 [Hz]
filter converter side inductance	L_o	2.6 [mH]
filter grid side inductance	L_g	662 [µH]
filter capacitance	C_o	5.5 [µF]
filter trap branch capacitance	C_t	1 [µF]
filter trap branch inductance	L_t	244 [µH]
filter damping resistance	R_{co}	1 [Ω]

The dc bus was supplied by a 40 kW dc power source, supplied by Magna-Power. During the frequency variation and voltage dip tests, the power converter was connected to the grid through a California Instrument regenerative power source, model MX45, by which the grid voltage amplitude and frequency profiles were programmable. In this manner, a grid frequency sweep could be generated. The output impedance of the ac regenerative source was set to a very low value, 0.002+ j0.002 Ω, thus the voltage profile at the PCC became almost independent to the power injected by the power converter. In this way, the power response of the power converter could be compared with the theoretical response given by the transfer functions such as (4.6), (4.19) and (4.34) to validate the designed inertial characteristic. The control algorithm was implemented in a dSPACE 1103 real-time control system by using the same code used in simulation tests.

B.2 Asymmetrical Grid Fault Test Setup

Fig. B.4 shows the block diagram of the asymmetrical grid fault experimental setup, which was pictured in Fig. B.5.

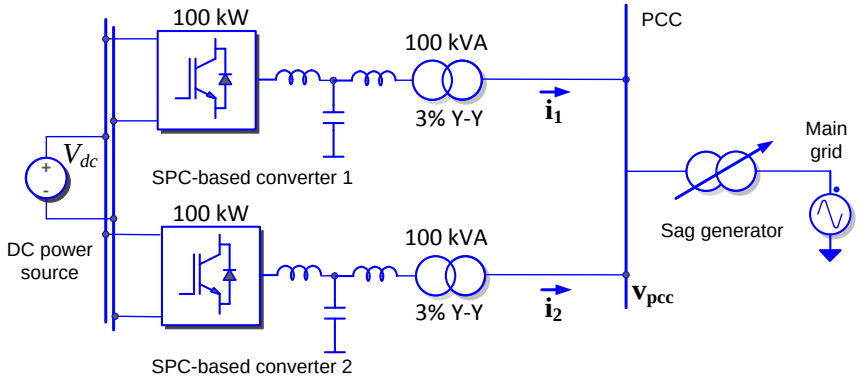

Fig. B.4. Block diagram of the asymmetrical grid fault experimental setup.

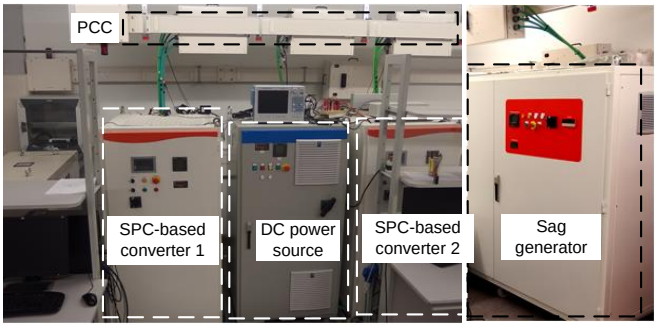

Fig. B.5. Laboratory view of the asymmetrical grid fault experimental setup.

These two 100 kW SPC-based grid connected power converters have the same specs as table B.2 shows. Table B.2 also lists other setup parameters for asymmetrical grid fault experimental tests.

The power rating of the dc power source is 250 kW, which is sufficient to supply both power converters. The grid link filter for each converter is LCL-trap filter with the parameters shown in Table B.2. The sag is triggered manually in the tests.

Table B.2 Parameters of the asymmetrical grid fault experimental setup

Description	Symbol	Value
nominal grid voltage	V	400 [V]
grid frequency	f_g	50 [Hz]
sag generator equivalent inductance	L_s	800 [μH]
dc bus voltage	V_{dc}	750 [V]
converter rated power	P_n	100 [kW]
converter rated current rms	I_n	160 [A]
switching frequency	f_{sw}	3150 [Hz]
samping frequency	f_s	6300 [Hz]
filter converter side inductance	L_o	778 [μH]
filter grid side inductance	L_g	402 [μH]
filter capacitance	C_o	66 [μF]
filter trap branch capacitance	C_t	30 [μF]
filter trap branch inductance	L_t	85 [μH]
filter damping resistance	R_{co}	0.5 [Ω]
virtual reactance	X_{pu}	0.3 [p.u.]
filtering stage bandwidth	k_{bw}	0.3
virtual inertia constant	H	5 [s]
virtual damping factor	ξ	0.7
reactive power control	K_{pq}	1e-5
reactive power control	K_i	1e-7
current controller	K_p	4.5
current controller	K_r	100